Stony Brook University

Mechanisms Underlying Angiotensin II Type 1 Receptor Mediated Electrical Remodeling in Left Ventricular Myocytes

A Dissertation Presented

by

Jeremy Hyonjoon Kim

to

The Graduate School

in Partial Fulfillment of the

Requirements

for the Degree of

Doctor of Philosophy

in

Biomedical Engineering

Stony Brook University

August 2011

Stony Brook University

The Graduate School

Jeremy Hyonjoon Kim

We, the dissertation committee for the above candidate for the

Doctor of Philosophy degree,

hereby recommend acceptance of this dissertation.

Richard T. Mathias, Ph.D. Dissertation Advisor
Professor of Physiology & Biophysics

Emilia Entcheva, Ph.D. Chairperson of Defense
Associate Professor of Biomedical Engineering

Ira S. Cohen, M.D., Ph.D.
Leading Professor of Physiology & Biophysics

Richard Z. Lin, M.D.
Professor of Medicine

Roman Shirokov, Ph.D.
Associate Professor of Pharmacology & Physiology
UMDNJ – New Jersey Medical School

This dissertation is accepted by the Graduate School

Lawrence Martin
Dean of the Graduate School

Abstract of the Dissertation

Mechanisms Underlying Angiotensin II Type 1 Receptor Mediated Electrical Remodeling in Left Ventricular Myocytes

by

Jeremy Hyonjoon Kim

Doctor of Philosophy

in

Biomedical Engineering

Stony Brook University

2011

The angiotensin II type 1 (AT_1) receptor is a G protein coupled receptor that is highly active in various cardiac disease states. Both the AT_1 receptor and its primary effector, angiotensin II (A2), are known to be expressed in cardiac tissue. AT_1 receptor activation leads to the transactivation of various intracellular signaling pathways that are known to be responsible for physiological and pathological changes in both cardiac structure and function. In particular, AT_1 receptors are involved in physiological adaptation to increased hemodynamic load, but they are also involved in the development of pathological cardiac hypertrophy, which is characterized by structural and electrical remodeling during the progression into heart failure. However, the AT_1 receptor-mediated mechanisms underlying these changes are unclear. Therefore, the overall aim of this study was to highlight the importance of AT_1 receptors in mechanical stress-induced electrical remodeling and to understand the mechanisms underlying AT_1 receptor-mediated regulation.

The following is a summary of our findings. Using the whole-cell patch clamp technique on isolated left ventricular myocytes from a pressure overload-induced mouse model of cardiac hypertrophy, we measured the time dependence of reductions in two predominant repolarizing currents, the fast and slow components of the transient outward K+-current ($I_{to,fast}$ and $I_{K,slow}$). These reductions preceded structural remodeling of the heart. We also present evidence supporting our hypothesis that AT_1 receptors mediate these reductions. Moreover, we present evidence supporting a novel hypothesis that AT_1 receptor-mediated downregulation of $I_{to,fast}$ and $I_{K,slow}$ does not involve G protein stimulation; rather, it appears to depend on receptor internalization, which leads to reductions in functional $I_{to,fast}$ and $I_{K,slow}$ channel densities. Finally, with the aid of a computational action potential model and multivariable linear regression, we quantified the relative significance of various electrophysiological parameters, including $I_{to,fast}$ and $I_{K,slow}$ properties, on the determination of the action potential morphology.

The results presented in this work provide new insights into AT_1 receptor-mediated changes that are typically associated with heart failure.

TABLE OF CONTENTS

LIST OF FIGURES

LIST OF TABLES

LIST OF ABBREVIATIONS

A2	Angiotensin II
AP	Action Potential
APD	Action Potential Duration
AT_1	Angiotensin Type 1
ATP	Adenosine Triphosphate
C_m	Cell Capacitance
DAG	Diacylglycerol
DCM	Dilated Cardiomyopathy
GPCR	G Protein Coupled Receptor
GRK	G Protein Coupled Receptor Kinase
HT/BW	Heart to body weight ratio
IP_3	Inositol 1,4,5-Triphosphate
KChAP	Kv Channel-Associating Protein
KChIP	Kv Channel-Interacting Protein
LV	Left Ventricle (or Ventricular)
MLR	Multivariable Linear Regression
NCX	Sodium Calcium Exchanger
PLS	Partial Least-Squares
PMCA	Plasma Membrane Ca^{2+}-ATPase
Sar	Saralasin
SERCA	Sarco-endoplasmic Reticulum Calcium ATPase

SII	[Sar^{1}-Ile^{4}-Ile^{8}]AngII
SR	Sarcoplasmic Reticulum
TAC	Transverse Aortic Constriction
TTX	Tetrodotoxin

ACKNOWLEDGEMENTS

While this manuscript was being put together, I had the privilege of working alongside professors, who contributed valuable insights and expertise on this subject matter. I am grateful for my advisor Dr. Rick Mathias, who possesses an unbridled passion for science that is transparently displayed in his work and in his speech. Moreover, he has repeatedly demonstrated his dedication and commitment to my research and guided me from the incipience of my project to the completion of this document. These valuable qualities are highly desired in a dissertation advisor and I am truly blessed to have Rick take me under his wings for the past few years as I journeyed towards becoming an independent researcher. I am also thankful for my dissertation committee members Dr. Emilia Entcheva, Dr. Ira Cohen, Dr. Richard Lin and Dr. Roman Shirokov for their constructive criticisms that challenged me to grow as a scientist and also for their helpful discussions which guided my research aims.

The technical skills and resources required for this work were acquired from various people here at Stony Brook University who are highly skilled in their respective areas of expertise. I am especially grateful for Dr. Junyuan Gao, who introduced me to the whole-cell patch clamp technique, which was used to obtain the majority of the data presented in this work. I also thank Joan Zuckerman for isolating and providing canine cardiac myocytes on a weekly basis and Dr. Zhongju Lu for offering sound advice on various patch-clamp techniques. Dr. Yaping Jiang performed the aortic constriction (and sham) surgeries on mice, which were crucial for our research aims. I also acknowledge Dr. Wei Wang, who, as a former lab member, trained me in the cardiac cell isolation procedure and Dr. Claire Wu was instrumental in further refining and improving the isolation procedure. Finally, I would like to thank other members of our lab Dr. K. Varadaraj, Dr. Xiurong Sun, Dr. Huan Wang, Stalin Mafla, Melissa Farrell and Abha

Kochhar for making each day all the more enjoyable and for their warm presence here at the university.

I cannot overstate the importance of family and friends, who have unconditionally loved and supported me throughout my academic career. I am grateful for my parents, who did their best to raise me up, and also for my two sisters, Stephanie and Borin, who encouraged me to do my best. I cannot imagine this academic journey without the presence of my fellow classmates and friends, who shared in similar struggles and understood the toils as well as the joys of Ph.D. student life.

My wife, Sue, has been my pillar of support especially this past year as I neared completion of my dissertation work. While I was focused on my work, Sue worked tirelessly to keep everything else going in our lives, including upkeep of our home and taking care of my physical needs, which I oftentimes tended to neglect. She was also my source of encouragement and strength, an uplifting presence in my life. She is truly a blessing and I love her dearly.

Finally, I would like to thank God for His guiding hand in my life and for leading me to this university, where I have been tremendously blessed.

Chapter 1

General Introduction

1.1 Clinical Relevance

Heart failure remains as one of the most costly diseases, which in 2007 was mentioned in nearly 300,000 death certificates in the United States and it was the underlying cause in 57,000 of those deaths (Roger, et al. 2011). Despite the fact that heart failure diagnosis has improved, the death rate remains high and based on statistical data, approximately half of those diagnosed with heart failure will die within 5 years (Roger, et al. 2011). These statistics demonstrate an urgent need for improved treatment and diagnostic procedures for heart failure.

Heart failure is diagnosed clinically when a patient displays physical symptoms and when subsequent tests (i.e. echocardiography) reveal structural remodeling, which usually indicates a pathological deviation from healthy and normal heart function (Lips, et al. 2003). Structural remodeling can manifest in the form of a dilated heart (dilated cardiomyopathy, or DCM) that leads to reduced contractile function or alternatively it can be in the form of cardiac hypertrophy, which is characterized by a thickening of the myocardial wall, that may or may not preserve normal function (Mudd and Kass, 2008). In many instances, an increase in left ventricular mass is a known risk factor for cardiac disease such as ischemic heart disease, arrhythmias and sudden cardiac death (Levy, et al. 1990). Medical intervention at early stages of heart failure may prevent the heart from progressing into tissue damage and irreversible heart failure, at which point treatment options are less viable. Additionally, since there are different classifications of heart failure, a need for more focused strategies to combat various manifestations of heart failure is needed. Characterizing the patterns of changing cellular and molecular activity from early to end stage heart failure in various pathological phenotypes will likely help answer some of these needs.

1.2 Cellular Components and Mechanisms Underlying Heart Function

The heart is the primary means by which every cell in the natural body receives oxygen and nutrients via vascular transport. It is a muscular pump that is capable of generating the level of force that is necessary to maintain continuous blood flow throughout the body. Besides maintaining its life-sustaining beat, it is crucial for the heart to be capable of responding and adjusting according to the body's changing demands. The heart possesses an ability to make adjustments by increasing both the beating frequency and force production to meet increasing demands. These adaptations are only temporary and are reversible should the demand be reduced. The heart also has the ability to adapt structurally via addition of myofibrils—contractile units in the myocardium—that provide increased contractile force and the ability to overcome greater hemodynamic resistance. This structural adaptation is a long-term response to sustained increases in hemodynamic load and has also been shown to be reversible once the hemodynamic burden is mitigated (Levin, et al. 1995). The mechanisms underlying these adaptations comprise complex cellular feedback systems that sense physiological stimuli and respond with the appropriate changes to optimize cardiac performance. Any failure in these mechanisms can cause the heart to fall out of its delicate balance, initiating a series of molecular changes that are pathological in many instances.

The heart comprises excitable cells interconnected via gap junctions that enable rapid propagation of excitation, which is crucial for synchronous activation and contraction. Excitable cells rely on potential differences and electrochemical gradients between the intracellular milieu and interstitial spaces to supply the driving force for ion channel activity. In a beating heart cell, this activity is represented in the morphology of the action potential. In left ventricular myocardium, variations in the morphology of the action potential exist regionally (Litovsky and

Antzelevitch, 1988; Fedida and Giles, 1991) and among species (Varro, et al. 1993), but they all retain a characteristic depolarizing spike which represents Na^+ entry from the opening of voltage-gated fast Na^+ channels (I_{Na}). In most mammalian species, the dome-shaped plateau and repolarization phases are produced by the influx of Ca^{2+} through voltage-gated calcium channels (I_{CaL}) and the opening of voltage-gated K^+ channels which, over time, cause the membrane potential to approach the Nernst potential for K^+. For the continuous elicitation of action potentials, $[Na^+]_i$ must be maintained relatively low while $[K^+]_i$ is maintained relatively high. This requires activity of the sodium-potassium (Na/K) ATPase (reviewed in Glitsch, 2001), which, in each cycle, uses the energy of 1 ATP to translocate 3 Na^+ and 2 K^+ across the membrane in opposite directions. This produces a net outward current (I_P) that is measureable using electrophysiological methods. Under physiological conditions, the Na/K-ATPase extrudes Na^+ from and transports K^+ into the cell interior, a process that balances the influx of Na^+ and efflux of K^+ that occurs through ion channels during each action potential. During each action potential, depolarization induced influx of Ca^{2+} through the L-type channels (I_{CaL}) triggers the rapid release of Ca^{2+} stored in the sarcoplasmic reticulum (SR) ($[Ca^{2+}]_{SR}$) which induces a transient rise in $[Ca^{2+}]_i$ and activates myosin-actin interactions that result in contraction—a phenomenon altogether known as excitation-contraction coupling (reviewed in Bers, 2002). Following this, Ca^{2+} pumps powered by ATP (Ca^{2+}-ATPases) in the sarcolemma (PMCA) and the SR membrane (SERCA2a) extrude Ca^{2+} from the cytosol via active transport either out of the cell or back into the SR, thereby reducing $[Ca^{2+}]_i$ and allowing myocyte relaxation. The sodium-calcium exchanger (NCX) is also responsible for maintaining a constant cycle of $[Ca^{2+}]_i$ during systole and diastole. This secondary active transporter is driven by the Na^+ electrochemical gradient (Main, et al. 1997). Increasing I_P under physiological conditions increases the Na^+

gradient, which in turn increases the driving force for NCX activity and increased Ca^{2+} extrusion, which results in lowered $[Ca^{2+}]_i$. Furthermore, a small, TTX-sensitive persistent Na^+ current (I_{pNa}) has been described in ventricular myocytes (Saint, et al. 1992) and studies have suggested that increased I_{pNa} can dramatically extend the action potential duration (Noble, et al. 1998, Sakmann, et al. 2000) and may be involved in the development of early after depolarizations (Ju, et al. 1996). The activity of these ion channels, pumps and exchangers are highly interdependent and their coordinated regulation maintains the appropriate duration, frequency and strength of the heartbeat.

1.3 Transient Outward K^+ Currents in Mammalian Species

Electrophysiological studies have demonstrated species differences in action potential waveforms (Varro, et al. 1993). Mouse and rat left ventricular (LV) action potentials are characterized by rapid repolarization that lacks a phase 2 plateau and are short (APD_{50} : ~3 to 10 ms) in comparison to those of humans, dog, guinea pig and rabbit, which display longer action potential duration (APD_{50}: ~150 to 400 ms) due to a prominent plateau phase (Fig 1.1). Action potential morphological differences among these species reflect differences in ion channel expression and regulation in the heart. In particular, species differences in repolarizing K^+ current expression have been well characterized (reviewed in Nerbonne and Kass, 2005). Action potential repolarizing currents are primarily composed of outward K^+ currents mediated by membrane channels having high K^+ selectivity. These K^+ currents are known to include fast- and slow-activating delayed rectifiers (I_{Kr} and I_{Ks}), transient outward K^+ currents (I_{to}), inward rectifier (I_{K1}) and the sustained outward current (I_{sus}) (Nerbonne and Kass, 2005). The voltage-

and time-dependent characteristics of these individual K^+ currents determine, on the most part, the shape and duration of the action potential.

Notably, species differences in transient outward K^+ current (I_{to}) contribute heavily to the diversity of action potential waveforms. Electrophysiological measurements of I_{to} in different species (Marionneau, et al. 2008; Li, et al. 2002; Nabauer, et al. 1996) have demonstrated varying levels of peak current amplitude, the differences of which are especially dramatic when comparing small rodents (mouse, rat) to larger mammals (humans, dog, rabbit). Under similar whole-cell patch clamp conditions, reported values of ventricular peak I_{to} densities at test potentials of +40 mV range from 33 to 53 pA/pF in mouse (Marionneau, et al. 2008), 3 to 7 pA/pF in canine (Li, et al. 2002) and 2 to 11 pA/pF in human (Nabauer, et al. 1996). Additionally, voltage clamp recordings of I_{to} mouse LV myocytes display bi-exponential decay characteristics whereas a single component describes I_{to} decay in canine and human LV (Marionneau, et al. 2008; Li, et al. 2002; Nabauer, et al. 1996). This has been attributed to multiple types of I_{to} channels that are functionally expressed in the mouse LV consisting of two main types distinguished by their rates of inactivation. The fast inactivating component of I_{to} ($I_{to,fast}$) in mouse LV is consistent with I_{to} in humans and dog. In mouse LV, an additional component of I_{to} ($I_{K,slow}$) exists but this current is not expressed in the LV of larger mammals. Interestingly, I_{to} is absent in guinea pig LV (Varro, et al. 1993).

The contribution of I_{to} to the action potential shape and duration is species dependent though in most species, the shape of the early phase 1 of the action potential is in large part determined by I_{to} due to its rapid activation especially at positive potentials. This is true for large species including humans and dog, in which a significant presence of I_{to} results in a phase 1 'notch' in the action potential (Litovsky and Antzelevitch, 1988). Most researchers agree that I_{to}

influences L-type Ca^{2+} currents ($I_{Ca,L}$) and Ca^{2+} handling, but the contribution of I_{to} to action potential duration and electrical propagation remains a controversial issue, especially in larger species. In mouse and rat LV, I_{to} is the dominant outward current and exceeds inward $I_{Ca,L}$ at depolarizing potentials, resulting in rapid repolarization and return to subthreshold potentials within a few tens of milliseconds (Watanabe, et al. 1983; Fiset, et al. 1997). Thus, in small rodents, both electrical activity and Ca^{2+} handling—and therefore mechanical properties—are strongly dependent on I_{to}.

Morphological changes in the action potential reflect changes in the activity of voltage- and time-dependent membrane ion channels and transporters that are also key regulators of intracellular Ca^{2+} and contractility. Therefore, remodeling of K^+ currents can drastically affect cardiac performance and indeed, a vast number of studies (reviewed in Tomaselli and Marban, 1999) have demonstrated remodeling of one or more K^+ currents in association with heart failure. Among these studies, I_{to} downregulation has been consistently observed in various animal heart failure models (Oudit, et al. 2001). Hence, discovering the mechanisms that result in the signature reduction of I_{to} should enhance our current understanding of heart failure.

1.4 Molecular Correlates of I_{to}

Species differences in I_{to} can be attributed to differences in the molecular basis of I_{to} expression. The fast component of I_{to}, which is expressed in mouse, rat, canine and human LV, is correlated with the Kv4 subfamily of pore-forming K^+ channel α subunits (reviewed in Niwa and Nerbonne, 2010). These subunits associate to form tetramers that are highly selective K^+ channels, which associate with various regulatory subunits that can alter the surface density or biophysical properties of these channels. The bulk of I_{to} in canine (Dixon, et al. 1996) and

human (Kaab, et al. 1998) LV is attributed to Kv4.3 whereas in the mouse, the majority of $I_{to,fast}$ is encoded by Kv4.2 though Kv4.3 is also expressed (Guo, et al. 2002; Guo, et al. 2005). The amino acid sequences of Kv4.2 and Kv4.3 are quite similar, especially in the pore region, which may explain the similarities in their time- and voltage-dependent characteristics. Additionally, Kv4.3 subunits have been shown to form heteromultimers with their homologous Kv4.2 counterparts, resulting in the formation of functional I_{to} channels in mouse LV (Guo, et al. 2002). Several previous reports have demonstrated that in mouse LV, functional $I_{K,slow}$ channels are formed by Kv1.5 and Kv2.1 (London, et al. 2001; Xu, et al. 1999). The absence of $I_{K,slow}$ in the LV of larger species such as the dog is confirmed by the lack of Kv2.1 mRNA expression though some levels of Kv1.5 transcript were detected (Dixon, et al. 1996). Despite the lack of Kv1.5 currents in canine LV, functionally expressed Kv1.5 channels and resulting $I_{K,slow}$-like currents are present in the canine atrium (Fedida, et al. 2003). This is one example of regional variations in K^+ channel expression, including those of Kv4.2/4.3, that are common among different species.

1.5 Regulatory Subunits of I_{to}

Various regulatory subunits and their influence on Kv channels in the heart have been extensively studied. In particular, Kv channel-interacting proteins (KChIPs) are ancillary subunits that are known to modulate Kv4 channel density and gating characteristics (Patel, et al. 2004). KChIP2 is the predominant isoform expressed in ventricular muscle and one report demonstrated the complete loss of Kv4.2/4.3 surface expression in KChIP2 knockout mice (Kuo, et al. 2001), demonstrating the importance of KChIP2 in I_{to} expression and electrical activity. In humans and dog, the level of I_{to} expression correlates with KChIP2 levels and thus it was

suggested that KChIP2 expression is the primary determinant regulating cardiac expression of I_{to} (Rosati, et al. 2001). However, angiotensin II-mediated regulation of the transmural gradient in I_{to} (reviewed below) is not consistent with this interpretation. Kv4.3 channels are also modulated by members of a family of Kvβ subunits (Yang, et al. 2001) which have also been shown to regulate the surface expression and kinetics of Kv1 channels (England, et al. 1995). Therefore, Kvβ subunits may potentially be involved in the regulation of both $I_{to,fast}$ and the Kv1.5 component of $I_{K,slow}$ in mouse LV. KChAPs (Kv channel-associated proteins) are another group of regulatory subunits that increases the surface expression of various Kv channels, but KChAPs do so without altering the gating or kinetics of the Kv channel (Kuryshev, et al. 2000). Associations with KChAPs have been shown to increase the amplitude, hence the plasma membrane expression levels, of Kv2.1, Kv2.2 (Wible, et al. 1998), Kv1.3 and Kv4.3 currents (Kuryshev, et al. 2000) some of which mediate I_{to} in the LV.

1.6 The Role of I_{to} in Heart Failure

Electrophysiological remodeling in various animal models of heart failure have been reported (reviewed in Tomaselli and Marban, 1999). This includes consistent patterns of I_{to} downregulation in failing hearts of animals (Benitah, et al. 1993) and humans (Beuckelmann, et al. 1993). Several of these studies used surgical techniques to induce heart failure in animals. In particular, aortic constriction (also known as aortic banding) is a common surgical procedure involving the use of a suture to constrict a section of the aortic arch to artificially increase hemodynamic stress, which eventually results in the development of pressure overload-induced cardiac hypertrophy and progression into failure (Rockman, et al. 1991). This is a widely used model of heart failure that mimics cellular remodeling in response to increased stress which can

be the result of hypertension, myocardial infarction, genetic mutations or valvular disease. Previous studies have demonstrated significant reductions in peak I_{to} density in aortic constriction-induced hypertrophied LV of rats (Benitah, et al. 1993; Tomita, et al. 1994) and mice (Wang, et al. 2007; Marionneau, et al. 2008). Similar trends in I_{to} downregulation were observed in larger species with heart failure induced using a variety of other methods (Lue, et al. 1992; Qin, et al. 1996; Kaab, et al. 1996; Rozanski, et al. 1997). However, the mechanisms underlying the reductions in I_{to} have not been elucidated.

More recently, experiments were conducted using mice with genetically altered reductions in I_{to}. Wickenden, et al. (1999) overexpressed the N-terminal fragment of the pore-forming Kv4.2 subunit, causing reductions in $I_{to,fast}$ through a dominant-negative mechanism (Wickenden, et al. 1999). These hearts displayed significant remodeling that included hypertrophy and action potential prolongations that eventually progressed to heart failure. In a separate study, the coding region of Kv4.2 was specifically deleted in the heart, effectively eliminating $I_{to,f}$, but unpredictably, a slow inactivating K^+ current (Kv1.4) was expressed and this current may have compensated for the lack of Kv4.2 (Guo, et al. 2005). Moreover, action potentials were not significantly different from controls and these hearts exhibited no signs of hypertrophy or myocardial dysfunction. The reasons for these disparate results, apart from the fact that different genetic methods were used, are unclear. Dominant-negative suppression of both Kv1 and Kv4 channels in mouse hearts, which do not express a compensating Kv1.4 current, resulted in significant prolongations of the action potential and QT interval (Brunner, et al. 2001). Despite the significant delay in repolarization, these mice displayed minimal increases in susceptibility to arrhythmogenesis compared with the drastic increases exhibited in Kv1 suppressed mice. A possible reason for this (suggested by Brunner, et al. 2001) was that Kv1

suppression (resulting in the attenuation of $I_{K,slow}$) enhanced the dispersion of repolarization, which is defined as a deviation from synchronous repolarization of the ventricles, whereas the homogenous prolongation of action potentials in Kv4/Kv1 suppressed mice, which have attenuated $I_{to,fast}$ and $I_{K,slow}$, prevented dispersion. If this is true, the expression ratio $I_{to,fast}$:$I_{K,slow}$ may be an important determinant of arrhythmogenesis in the mouse heart. In larger species, I_{to} is less dominant and therefore the translation of conclusions drawn from genetic studies in mice to studies of larger species needs to be carried out with caution.

Myocardial contraction is highly dependent on the regulated release of SR Ca^{2+}. Therefore, factors that control SR Ca^{2+} release strongly influence the mechanical properties of the heart. One of the major factors that governs the release of SR Ca^{2+} is the time dependence and magnitude of Ca^{2+} influx through L-type channels ($I_{Ca,L}$), which are the primary "trigger" for the ensuing events that culminate in Ca^{2+} dependent contraction. Several studies (Greenstein, et al. 2000; Sah, et al. 2002b) have addressed the importance of I_{to} in regulating myocardial contraction through its influence on the rate of repolarization, which determines the magnitude and time course of $I_{Ca,L}$. In small rodents, attenuation of I_{to} is correlated with increases in net Ca^{2+} entry via $I_{Ca,L}$, enhanced Ca^{2+} transient amplitudes and increased contraction (Brouchard, et al. 1995; Sah, et al. 2002a). These studies suggest that I_{to} reduction mediates a positive inotropic effect in mice and rats by prolonging the action potential and increasing net influx of Ca^{2+} via $I_{Ca,L}$. It is therefore plausible that I_{to} reduction is triggered during the progression to heart failure as an early response to compensate for increasing demand. In larger species, the physiological and pathological role of I_{to} is more controversial. In these species, I_{to} influences early repolarization (Greenstein, et al. 2000) similar to rodents, but unlike these smaller animals, repolarization of the action potential is dependent not only on I_{to} but on the interplay of multiple

ionic currents including $I_{Ca,L}$ and the sodium-calcium exchanger current (I_{NCX}) (Armoundas, et al. 2003). Indeed, electrophysiological remodeling in failing hearts usually involves alterations in multiple ionic currents and the complexity of this combined activity is difficult to study without the aid of computer modeling. In one study, simulations of the canine action potential revealed that when I_{to} amplitude is low, which is typical in humans and dog, increasing I_{to} augments the driving force for $I_{Ca,L}$, thus increasing Ca^{2+} influx (Greenstein, et al. 2000). In contrast with findings in small rodents, this study indicates that a reduction in I_{to} leads to decreased L-type channel Ca^{2+} influx that contributes to decreased myocyte contractility and overall depression in cardiac function. However, this investigation did not consider how changes in I_{to} in conjunction with changes in other ionic currents affect the action potential configuration.

Regional heterogeneities in action potential morphology are thought to play a critical role in the maintenance of normal electrical propagation and contraction throughout the myocardium. Underlying these differences are regional heterogeneities in ionic currents. These include transmural differences in the functional expression of membrane currents such as I_{to} (Litovsky and Antzelevitch, 1988), $I_{Ca,L}$ (Wang and Cohen, 2003) and the Na/K ATPase current (I_P) (Gao, et al. 2005). In canine hearts, endocardial $I_{Ca,L}$ is higher than epicardial, but I_{to} and I_P are smaller. Transmural differences in I_{to} are also present in mouse LV (Brunet, et al. 2004) and these differences are abolished in pressure overload induced hypertrophy with overall reductions in I_{to} to endocardial levels (Wang, et al. 2007; Marionneau, et al. 2008).

Taken together, it appears that transmural heterogeneities in electrophysiological properties contribute to transmural differences in myocyte contractility. A distinguishable difference in stress distribution exists during diastole between the endocardium and the epicardium in which the endocardium experiences stresses that are much greater (Streeter, et al.

1970). A transmural gradient in passive tension through the thickness of the myocardium may differentially regulate the functional expression of ionic currents in each transmural region via mechanotransduction, which could explain the reported transmural differences in I_{to}, $I_{Ca,L}$ and I_P. In response to higher levels of mechanical stress, the endocardium may respond by expressing higher $I_{Ca,L}$ with lower I_P and I_{to} to generate a higher level of contractility relative to the epicardium. Regulation of contractility between epicardial and endocardial layers is plausible given the transmural difference in load distribution. Furthermore, under pressure overload conditions, increased hemodynamic stress beyond physiological levels may initially reduce I_{to}, I_P and increase $I_{Ca,L}$ in all transmural layers to endocardial levels as a part of a fast compensatory response to increased load, eventually followed by cardiac hypertrophy as a late response to equalize wall stress (Fig 1.2). In tandem with other electrophysiological changes, I_{to} reduction may contribute to an immediate compensatory response to enhance force generation under conditions of increased hemodynamic stress. The following section will discuss our hypothesis on the mechanisms underlying this response.

1.7 Angiotensin II and AT_1 Receptor Mediated Regulation of I_{to}

Various physiological stimuli, which include activation of surface membrane receptors by autocrine/paracrine factors, regulate the functional expression of I_{to} in cardiac myocytes (Niwa and Nerbonne, 2010). We propose a novel mechanism that involves the angiotensin II type 1 (AT_1) receptor and its agonist angiotensin II (A2) in mechanical stress mediated regulation of I_{to}. A2, which is commonly known as a pressure regulator in blood vessels, activates AT_1 receptors to initiate a cascade of intracellular signaling pathways that systemically increase vascular constriction (Mehta and Griendling, 2007). The AT_1 receptor is a seven-pass

transmembrane G protein coupled receptor (GPCR) that undergoes endocytosis upon the binding of its agonist A2 (van Kats, et al. 1997). Stimulation of the AT_1 receptor results in the parallel activation of various intracellular pathways, many of which start with activated G protein subunits. The canonical signaling pathway involves activation of phospholipase C (PLC) which hydrolyzes phosphatidylinositol 4,5-biphosphate to form inositol 1,4,5-triphosphate (IP_3) and diacylglycerol (DAG). IP_3 releases Ca^{2+} from intracellular stores and thereby enhances the activity of these second messengers. A rise in Ca^{2+} and DAG is known to increase the activity of protein kinase C (PKC) which phosphorylates various downstream molecules. Furthermore, AT_1 receptor stimulation eventually results in receptor phosphorylation by G protein-coupled receptor kinases (GRKs) and this promotes the recruitment and binding of β-arrestin to the receptor. The interaction of β-arrestins with AT_1 receptors prevents further G protein signaling and desensitizes the receptor to external stimulation. β-arrestin then serves as a scaffold for the binding of various proteins that include trafficking proteins (i.e. clathrin) and signaling molecules (Lefkowitz and Shenoy, 2005). As a result, β-arrestin mediates G protein-independent mechanisms of the AT_1 receptor that include receptor internalization via clathrin-coated pits and various signaling pathways.

In cardiac myocytes, AT_1 receptor mediated signal transduction results in hypertrophic growth (Sadoshima and Izumo, 1993; Paradis, et al. 2000) and electrical remodeling involving upregulated L-type Ca^{2+} current ($I_{Ca,L}$) (Ichiyanagi, et al. 2002; Aiello, et al. 2001) which contributes to a positive inotropic effect (Freer, et al. 1976). Additionally, A2 and AT_1 receptor activity have been shown to modulate I_{to} in cardiac myocytes. In canine left ventricle (LV), external application of A2 for 2 or more hours induced a considerable reduction of I_{to} in epicardial myocytes, resulting in levels that were comparable to I_{to} in the endocardium (Yu, et al.

2000). Conversely, application of an AT_1 receptor antagonist increased I_{to} in endocardial cells to levels that approached epicardial I_{to}. In a separate report, cardiac-specific overexpression of human AT_1 receptors in mouse hearts displayed attenuated I_{to} which was accompanied by hypertrophy and increased incidence of cardiac arrhythmias (Rivard, et al. 2008). These reports suggest an important role of AT_1 receptors in modulating I_{to} particularly in the context of cardiac disease progression.

The existence of circulating A2 produced in the kidneys is well known, but recently, the existence of a local renin-angiotensin system (RAS) in the myocardium has been demonstrated (van Kats, et al. 1998). In addition, Sadoshima et al. (Sadoshima, et al. 1993) mechanically stretched neonatal cardiac myocytes in vitro and observed acute A2 secretion that resulted in the induction of the hypertrophic response. This response was inhibited in the presence of AT_1 receptor antagonists suggesting that mechanical stretch induced secretion of A2 stimulates receptors in an autocrine fashion. Several years later, researchers produced new evidence to support mechanical stress-induced AT_1 receptor mediated cardiac hypertrophy without the involvement of A2 (Zou, et al. 2004, Yasuda, et al. 2008a). It was determined that mechanical stretch induced a conformational switch of the AT_1 receptor into an active conformation that could be prevented with an AT_1 receptor antagonist (Yasuda, et al. 2008b). Interestingly, there is evidence suggesting that different conformational states of the AT_1 receptor trigger unique sets of intracellular signaling pathways (Holloway, et al. 2002; Wei, et al. 2003). Thus, the activation stimulus (e.g. agonist binding, mechanical stress) may be an important determinant of which downstream signals of the AT_1 receptor are triggered and which are not.

We recently presented work in an abstract form (Gao, et al. *Biophysical Meeting*, 2008) documenting the effects of A2 on I_{to} measured from cardiac myocytes that were isolated from

different transmural layers of the canine LV. Application of receptor saturating A2 concentrations (5 μM) abolished transmural differences and attenuated I_{to} uniformly to endocardial values (Fig 1.3). Conversely, application of saturating concentrations (5 μM) of the AT_1 receptor antagonist Losartan increased I_{to} uniformly in all layers to epicardial levels (not shown). These results suggest that the maximal I_{to} capacity is similar in all transmural layers but the presence of a transmural gradient in endogenous A2 concentration results in a gradient in I_{to}. Assuming the LV wall experiences a transmural gradient in load and therefore a transmural gradient in passive tension, we hypothesize that the gradient in tension produces a corresponding gradient in autocrine A2 release as indicated by a transmural gradient in I_{to}. In other words, the level of endogenous A2 secretion in the LV wall appears to be proportional to the degree of cell stretch. Therefore, it is our working hypothesis that mechanical stress induced reductions in I_{to} are mediated by AT_1 receptor activation, which also have a prominent role in initiating the hypertrophic program.

1.8 Summary

The heart possesses the means to adapt to transient and chronic increases in hemodynamic load, but the mechanisms by which these adjustments are implemented continue to elude us. We have outlined past and current research, which address the relationships between electrical remodeling of the myocardium, particularly that of I_{to}, and heart failure, and also presented evidence to support AT_1 receptor-mediated regulation of I_{to}. Synthesizing this knowledge allows us to construct a mechanistic understanding of how the heart may adjust to compensate for increased load. A theoretical diagram of this mechanism is shown in Figure 1.4. We hypothesize that increased load triggers the secretion of A2 and increases AT_1 receptor

activity, which initially induces electrical remodeling of the myocardium that includes I_{to} reduction. As a result, these changes contribute to increases in $[Ca^{2+}]_i$ and increased contractility as a means to compensate for increasing demand before the onset of cardiac hypertrophy. The work presented here comprises experimental evidence to support some of these relationships while providing new molecular insights, and the use of computational models to understand the relative contributions of different ionic current properties to the action potential morphology. Experiments were conducted on LV cells from mice to complement an increasing amount of knowledge concerning cardiac disease that is largely based on studies using genetically altered mice. Accordingly, we attempted to fulfill the following objectives:

1) to demonstrate AT_1 receptor involvement in electrical remodeling that precedes hypertrophy under conditions of increased hemodynamic load,
2) to understand the molecular mechanisms underlying AT_1 receptor-mediated regulation of I_{to},
3) and to utilize a mathematical model to quantify relative contributions of I_{to} characteristics in influencing the action potential morphology.

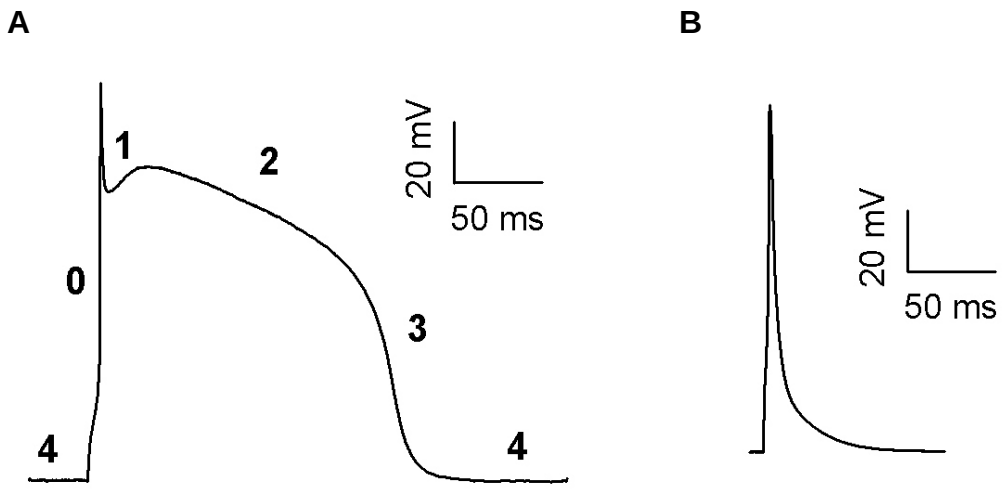

Figure 1.1: Example of interspecies differences in action potential morphology. (A) Canine left ventricular epicardial action potential "spike-and-dome" morphology. Each phase of the action potential is numerically represented (0: fast depolarization, 1: "notch", 2: plateau phase, 3: repolarization, 4: resting phase). (B) Mouse left ventricular action potential. Large I_{to} amplitudes in mouse cardiac myocytes cause rapid repolarization without a plateau phase.

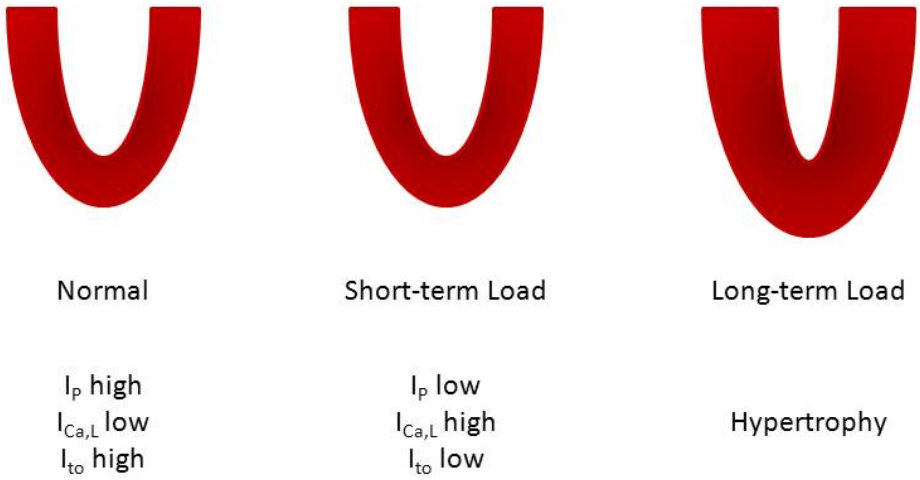

Figure 1.2: Theoretical model of electrical and structural remodeling of the LV over time in response to increased hemodynamic load. Short-term response to increased load may involve remodeling of I_P, $I_{Ca,L}$ and I_{to} as part of an immediate compensatory adaptation to generate increasing contractile force. Cardiac hypertrophy develops later in response to sustained load.

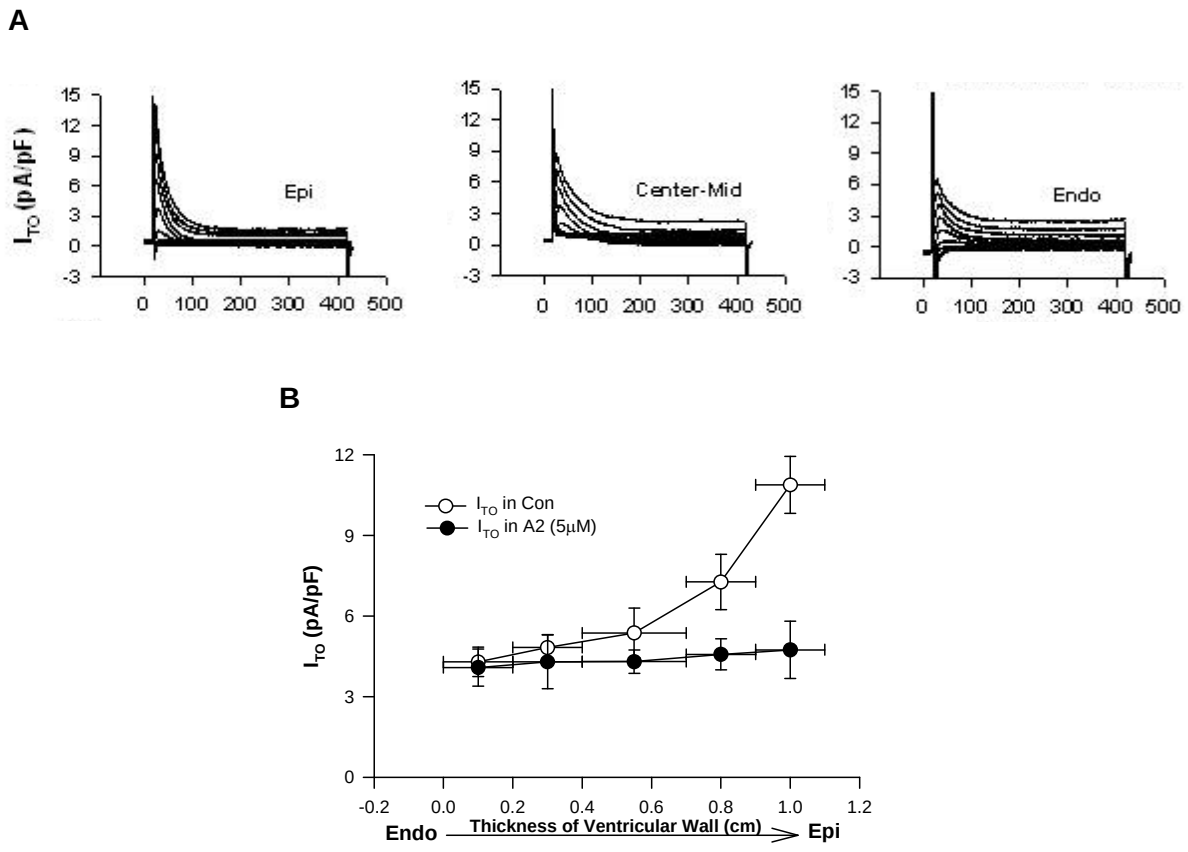

Figure 1.3: (A) Representative whole-cell patch clamp traces of I_{to} obtained from canine epicardial (Epi), midmyocardial (Center-Mid) and endocardial (Endo) myocytes. (B) Mean values of peak I_{to} through the thickness of the LV wall (open circles). Incubation with saturating concentrations of A2 reduces I_{to} in all transmural layers to endocardial values (filled circles). Treatment with A2 abolishes the transmural gradient in I_{to}. (Unpublished data by Gao et al.)

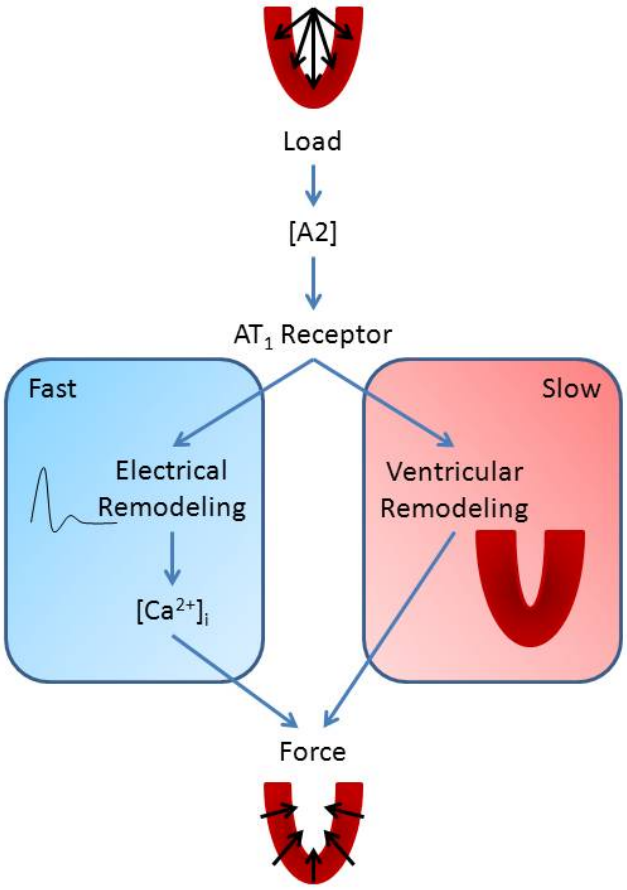

Figure 1.4: Summary of the hypothetical mechanism that senses and adjusts in response to increasing load in the progression to heart failure. Increasing hemodynamic load stretches the myocardium, increasing the secretion of autocrine A2 and activating more AT_1 receptors. The ensuing events can be divided into fast and slow sets of responses. The fast response involves remodeling of membrane currents I_P, I_{to} and $I_{Ca,L}$ that contributes to the rise in $[Ca^{2+}]_i$ and enhanced contractility. The slow response involves hypertrophic signaling through a G protein dependent pathway that results in increased protein synthesis and the addition of myofibrils, which provides the force to offset the increase in load.

Chapter 2

Role of AT_1 Receptors in Mechanical Stress-Induced Electrical Remodeling

2.1 Introduction

The heart is composed of specialized cells that possess the ability to respond appropriately to increased mechanical stress with structural and functional adaptations. This inherent ability of the heart involves a vast network of cellular and molecular interactions that regulate hypertrophic growth and electrophysiological activity within individual cells. In cardiac myocytes, sustained increases in mechanical stress trigger the hypertrophic program which includes the induction of immediate-early genes such as *c-fos, c-jun, Egr-1 and c-myc* as well as the reactivation of fetal genes, which are typically expressed in developing hearts (Sadoshima and Izumo, 1997; Lammerding, et al. 2004). Re-expressed fetal genes in adult hearts allow protein synthesis thereby resulting in increased myocyte size. In particular, expression levels of myosin heavy chains, natriuretic peptides and α-actinin increase dramatically in hypertrophied cells. Functionally, the synthesis and addition of sarcomeric proteins in hypertrophied myocytes promote increased contractility.

A considerable number of studies have demonstrated the involvement of the angiotensin type 1 (AT_1) receptor in the control and regulation of the hypertrophic program in cardiac myocytes (Barry, et al. 2008; Heineke and Molkentin, 2006). The classical mechanism of AT_1 receptor activation involves the binding of its agonist angiotensin II (A2) to the extracellular domain of the AT_1 receptor, resulting in G protein stimulation and receptor internalization. Previous studies have demonstrated the existence of local A2 production in cardiac tissue (Van Kats, et al. 1998) and evidence of A2 acting locally within cardiac tissue to enhance protein synthesis and cell growth (Baker and Aceto, 1990). Additionally, increased mechanical stress has been linked to heightened AT_1 receptor activity via autocrine secretion of A2 in cardiac myocytes that results in enhanced expression of hypertrophic genes (Sadoshima, et al. 1993).

In addition to these structural adaptations, mechanical stress and neurohormonal stimulation of the AT_1 receptors have been identified as external signals that induce electrical remodeling in cardiac myocytes (Cutler, et al. 2011). For instance, in the dog left ventricle, rapid pacing triggered action potential prolongations that were attributed to increased circumferential strain (Jeyaraj, et al. 2007). With respect to neurohormonal stimulation, alterations in the action potential morphology and reduced transient outward K^+ current densities (I_{to}) were observed in dog left ventricular epicardial myocytes that were incubated in the presence of A2 (Yu, et al. 2000). Additionally, increased L-type Ca^{2+} currents and positive inotropic effects have been observed in cardiac myocytes stimulated with A2 across various species (Ichiyanagi, et al. 2002; Aiello and Cingolani, 2001; Freer, et al. 1976).

Taken together, the evidence suggests a central role of the cardiac AT_1 receptor in mechanical stress induced structural and electrical remodeling. The aforementioned findings prompted the present study to test the hypothesis that mechanical stress induces electrical remodeling via AT_1 receptor activation in cardiac myocytes. Mechanical stress was applied to left ventricular myocytes *in vivo* with aortic constriction and cells were harvested both before and after the onset of hypertrophy. Our results indicate that mechanical stress induced electrical remodeling precedes hypertrophic growth and this remodeling is reversible with AT_1 receptor blockade.

2.2 Materials and Methods

2.2.1 Transverse Aortic Constriction

In 2 to 3 month old wild-type C57/BL6 mice, transverse aortic constriction (TAC) was employed to apply pressure-overload induced mechanical stress on left ventricular myocytes.

The surgical procedure used in these studies to apply TAC in mice is outlined in a previous report (Hu, et al. 2003). A 27-gauge needle was used for ligation, which was sufficiently narrow to induce hypertrophy within 1 to 2 weeks of surgery. For each TAC mouse, sham surgery was performed in a separate mouse to serve as a negative control. Identical procedures, with exception to ligation, were followed for both TAC and sham surgery. TAC and sham mice were sacrificed at 24 hours, 48 hours, 1 week and 2 weeks post-surgery to examine the effects of short-term and long-term aortic constriction in isolated cardiac myocytes.

2.2.2 Isolation of Left Ventricular Myocytes

At the appropriate time points following TAC or sham surgery, mice were euthanized via CO_2 inhalation in an enclosed chamber and upon their death, the weight of each animal was recorded. The chest cavity was opened and the heart was gently excised and immediately transferred into a 35mm dish with ice-cold Normal Tyrode Solution containing (in mM) 137.7 NaCl, 2.3 NaOH, 5.4 KCl, 1 $MgCl_2$, 10 Glucose and 5 HEPES (pH adjusted to 7.4 with NaOH). Extraneous tissues surrounding the aorta including the lungs, thymus and adipose tissue were carefully cleaned off using small scissors to expose the aorta for cannulation. The heart was then weighed in order to calculate the heart to body weight ratio for each mouse. A non-beveled needle was used to cannulate the aorta and the cannula was then attached to a temperature-controlled Langendorf apparatus that allows solution switching. The heart was first perfused with Normal Tyrode Solution at 37°C for 2 to 3 minutes to wash out residual blood in the coronary vessels. Perfusion was then switched to a Normal Tyrode Solution containing 0.16 mg/ml Liberase TH (Roche Applied Science, Inc., Indianapolis, IN) for 9 to 10 minutes or until the perfusion speed increased dramatically indicating significant tissue digestion. The cannula

with heart attached was then removed and KB solution containing (in mM) 83 KCl, 30 K_2HPO_4, 5 $MgSO_4$, 5 Na-Pyruvic Acid, 5 β-OH-Butyric Acid, 5 Creatine, 20 Taurine, 10 Glucose, 0.5 EGTA and 5 HEPES (pH adjusted to 7.2 with HCl) was manually perfused through the heart with a syringe to wash out the Liberase solution. The heart was placed in a dish containing KB solution and the left ventricle was separated from the rest of the heart. The left ventricle was gently teased apart by mechanical agitation and filtered through a nylon mesh to collect the cell suspension. The isolated myocytes were stored in KB solution at 22°C for the duration of the experiments which did not last more than 12 hours post-isolation.

2.2.3 Cell Preparation

For each set of experiments (using either sham or TAC myocytes), the cell suspensions were divided into control and experimental groups for comparison. Cells in the experimental groups were treated for 2 to 12 hours with 5 μM saralasin (Sigma-Aldrich Inc.).

2.2.4 Electrophysiological Recordings

Whole-cell patch clamp experiments were conducted at room temperature (22°C) within 12 hours of cell isolation. For K^+-current measurements, the internal pipette solution contained (in mM) 115 K-Aspartic Acid, 25 KOH, 10 KCl, 3 $MgCl_2$, 11 EGTA, 10 HEPES and 5 Na_2-ATP (pH adjusted to 7.2 with KOH). Pipette series resistances were between 4-7 MΩ in whole-cell mode. During patch clamp recordings, myocytes were perfused with an external solution containing (in mM) 137.7 NaCl, 2.3 NaOH, 5.4 KCl, 1 $MgCl_2$, 1.8 $CaCl_2$, 2 $CoCl_2$, 10 Glucose and 5 HEPES (pH adjusted to 7.4 with NaOH). Voltage-clamp experiments were performed using an Axopatch 1D amplifier (Axon Instruments Inc.) interfaced to a computer with a

Digidata 1200 digitizer and pClamp 8.2 software (Axon Instruments Inc.). K^+ currents were measured in response to a short prepulse (10 ms) to -30mV to inactivate Na^+ channels followed by 6000 ms voltage steps (V_{test}) between +10 mV and +50 mV from a holding potential of -65 mV. For all voltage-clamp recordings, series resistances were compensated electronically by ~85%.

2.2.5 Data Analysis and Statistics

Voltage-clamp data were analyzed using Clampfit 8.2 (Axon Instruments Inc.), Microsoft Excel 7 (Microsoft Inc.), SigmaPlot 10 (Systat Software Inc.) and MATLAB (various versions, Mathworks Inc.). Distinct K^+ current components ($I_{to,fast}$, $I_{K,slow}$ and I_{sus}) were extracted from the obtained K^+ current recordings using the Curve Fitting Toolbox in MATLAB to fit a two-exponential decay function in the form of $A_1\exp(-t_1/\tau_1)+A_2\exp(-t_2/\tau_2)+A_3$ (Xu, et al. 1999). A_1 and A_2 represent peak amplitudes of $I_{to,fast}$ and $I_{K,slow}$ and their respective inactivation time constants differ by a factor of approximately 20. $I_{to,fast}$ was identified as the inactivating component with a decay time constant less than 100 ms and $I_{K,slow}$ was identified as the slower inactivating component (τ_{decay} > 1000 ms). A_3 represents the steady-state component I_{sus}. Peak current amplitudes were normalized to the cell capacitance (C_m), which was measured in each cell using the Membrane Test function in the pClamp software, and presented as current densities (pA/pF).

Differences in peak $I_{to,fast}$ and $I_{K,slow}$ current densities and amplitudes between groups were assessed with the Student's *t*-test.

2.3 Results

2.3.1 Evidence of Structural Remodeling

In this report, "short-term" is defined as a period lasting 1 to 2 days and "long-term" refers to a period lasting 1 to 2 weeks. To determine the extent of structural remodeling present in hearts that were subjected to various durations of pressure overload via aortic constriction, cell capacitances (C_m) and heart to body weight ratios (HT/BW) were documented. According to results presented in Fig 2.1A, short-term TAC myocytes yielded C_m values that were comparable to values measured from sham myocytes (Sham: 155.9 ± 7.1 pF, n = 14; TAC: 163.7 ± 5.1 pF, n = 15). Similarly, HT/BW measurements (Fig 2.1C) were not significantly different in these two groups (Sham: 8.22 ± 0.21 mg/g, n = 5; TAC: 8.44 ± 0.12 mg/g, n = 5). In contrast, long-term aortic constriction induced a significant rise in both C_m (Sham: 164.4 ± 8.8 pF, n = 12; TAC: 207.6 ± 7.2 pF, n = 14) and HT/BW (Sham: 7.57 ± 0.34 mg/g, n = 6; TAC: 9.83 ± 1.08 mg/g, n = 6) as displayed in Figs 2.1B and 2.1D. An increase in HT/BW indicates growth of heart mass which is related to an increased C_m, which is approximately proportional to the total surface membrane area and hence a good indicator of cell size.

2.3.2 Downregulation of $I_{to,fast}$ and $I_{K,slow}$ Induced by Short-Term Aortic Constriction

Having determined that structural remodeling has not occurred in response to short-term constriction, we investigated whether or not cardiac cells respond with electrical remodeling in response to short-term pressure overload. Specifically, we used whole-cell patch clamp methods to record $I_{to,fast}$ and $I_{K,slow}$, which contribute heavily to action potential repolarization in small rodents. Typical traces of outward K^+ currents, elicited with a voltage clamp protocol, are displayed in Fig 2.2 (voltage clamp protocol is also shown). $I_{to,fast}$ and $I_{K,slow}$ were

mathematically derived from these traces and the peak currents at each test potential (I-V relationships) were plotted (Fig 2.3). From these results, it appears that $I_{to,fast}$ is reduced (with statistical significance at two test potentials) in TAC myocytes relative to sham (At V_{test} = +50 mV, Sham: 27.3 ± 3.3 pA/pF; TAC: 20.1 ± 3.1 pA/pF) and $I_{K,slow}$ is also significantly reduced in TAC myocytes (Sham: 14.1 ± 2.2 pA/pF; TAC: 7.8 ± 0.9 pA/pF).

2.3.3 AT_1 Receptor Blockade Restores $I_{to,fast}$ and $I_{K,slow}$ in Myocytes Subjected to Short-Term Load

Reductions of $I_{to,fast}$ and $I_{K,slow}$ in short-term TAC myocytes were reversible upon stimulation of the isolated myocytes with the AT_1 receptor blocker saralasin. These results are presented in the I-V relationships of Fig 2.3, from which it can be appreciated that application of saralasin significantly increases both $I_{to,fast}$ (At V_{test} = +50 mV, TAC+Sar: 29.8 ± 3.1 pA/pF) and $I_{K,slow}$ (TAC+Sar: 15.4 ± 1.3 pA/pF) in TAC myocytes to values that are slightly higher than those of sham myocytes. In fact, $I_{to,fast}$ and $I_{K,slow}$ of saralasin treated cells in TAC myocytes are essentially the same as those of saralasin treated cells in the sham population (Sham+Sar: 29.1 ± 3.1 pA/pF and 15.8 ± 2.6 pA/pF for $I_{to,fast}$ and $I_{K,slow}$, respectively).

2.3.4 Downregulation of $I_{to,fast}$ Induced by Long-Term Aortic Constriction

Structural remodeling induced by long-term aortic constriction is apparent based on measurements of C_m and HT/BW (Fig 2.1). Having observed that both $I_{to,fast}$ and $I_{K,slow}$ are significantly attenuated in response to short-term aortic constriction, we investigated whether these changes are preserved in hypertrophied (long-term aortic constriction) cells. The I-V relationships of peak $I_{to,fast}$ densities (Fig 2.5A), which were derived from whole-cell patch clamp

recordings of outward K^+ currents (Fig 2.4). Based on this figure, $I_{to,fast}$ density of TAC myocytes appears to be significantly lower than sham $I_{to,fast}$ density (At V_{test} = +50 mV, Sham: 24.6 ± 2.3 pA/pF; TAC: 12.2 ± 1.1 pA/pF). To examine whether or not C_m accounts for this difference, we also documented peak $I_{to,fast}$ amplitudes (Fig 2.5C), which are current magnitudes not normalized by C_m. $I_{to,fast}$ amplitudes were also significantly less in TAC myocytes (Sham: 4219.4 ± 393.1 pA, TAC: 2558.6 ± 240.0 pA), indicating that the increase in C_m itself cannot account for the lower $I_{to,fast}$ density measured in TAC myocytes.

2.3.5 AT_1 Receptor Blockade Restores $I_{to,fast}$ in Myocytes Subjected to Long-Term Load

To test for the involvement of AT_1 receptors in pressure overload induced remodeling of $I_{to,fast}$, saralasin was applied to both sham and TAC myocytes. According to the results (Fig 2.5A and 2.5C), saralasin partially restored $I_{to,fast}$ density (At V_{test} = +50 mV, Sham+Sar: 26.0 ± 2.3 pA/pF; TAC+Sar: 19.2 ± 2.2 pA/pF) but fully restored the amplitude (Sham+Sar: 4087.1 ± 364.2 pA; TAC+Sar: 3933.5 ± 445.0 pA) in TAC myocytes. These results suggest that AT_1 receptor activation in response to pressure overload reduces $I_{to,fast}$ magnitude, resulting in reduced $I_{to,fast}$ density. Increased cell surface area also contributes to lower $I_{to,fast}$ density.

2.3.6 Reduced $I_{K,slow}$ in Myocytes Subjected to Long-Term Load is Less Responsive to AT_1 Receptor Blockade

$I_{K,slow}$ densities (Fig 2.5B) were significantly different between sham and TAC myocytes (At V_{test} = +50 mV, Sham: 11.3 ± 1.6 pA/pF; TAC: 7.3 ± 1.5 pA/pF) but the amplitudes (Fig 2.5D) were presented with only slight differences (Sham: 1938.7 ± 282.6 pA; TAC: 1529.4 ± 310.1 pA). Unlike $I_{to,fast}$, stimulation with saralasin only slightly increased $I_{K,slow}$ amplitude in

TAC myocytes (TAC+Sar: 1727.1 ± 230.2 pA) though it was difficult to determine whether or not it was significantly different from the sham group stimulated with saralasin (2136.7 ± 223.5 pA).

2.4 Discussion

Prior studies on mice have demonstrated electrical remodeling, particularly with regards to reductions in $I_{to,fast}$ and $I_{K,slow}$ (Wang, et al. 2007; Marionneau, et al. 2008), as part of a vast set of cellular and molecular changes that occur in response to sustained pressure overload. However, previous to our study, reductions in $I_{to,fast}$ and $I_{K,slow}$ were only observed in conjunction with the development of cardiac hypertrophy that resulted from pressure overload for periods of several days up to weeks. Therefore, we employed aortic constriction in wild type mice to document changes in $I_{to,fast}$ and $I_{K,slow}$ at earlier time points (1 to 2 days post-operation). Additionally, we investigated the role of AT_1 receptors in mediating mechanical stress induced changes in $I_{to,fast}$ and $I_{K,slow}$. In summary, aortic constriction for 1 to 2 days was not sufficiently long to induce hypertrophy in ventricular myocytes, yet $I_{to,fast}$ and $I_{K,slow}$ were significantly reduced. These reductions were fully reversible with the application of an AT_1 receptor antagonist (saralasin) to isolated myocytes for 2 or more hours. In hypertrophied myocytes, which were subjected to pressure overload for 1 to 2 weeks, $I_{to,fast}$ amplitude (un-normalized to C_m) fully recovered with the application of saralasin, but $I_{to,fast}$ density was only partially restored. In these cells, $I_{K,slow}$ displayed moderate reduction and minimal response to the application of saralasin.

2.4.1 Time to Pressure Overload-Induced Hypertrophy in Mice

Studies that have used similar methods of pressure overload (transverse aortic constriction) have provided evidence of the development of hypertrophy at various post-operation time points which range from 7 days (Marionneau, et al. 2008) to 3 weeks (Wang, et al. 2007) or more. Our observation of significant hypertrophy at 1 to 2 weeks is in agreement with these previous studies, which also used similarly sized needles for ligation, making these comparisons valid. A separate report (Deckmann, et al. 2010) documented changes in left ventricular weight to body weight ratio (LV/BW) from one hour to 48 hours post-operation from which it was apparent that between 12 to 48 hours, no significant change in LV/BW had occurred, consistent with our findings. One cause for concern was the potential for unknown stresses associated with anesthesia and surgery to induce changes at early time points in response to stress rather than aortic banding. Based on the consistency of relevant mRNA expression levels, one study demonstrated that the non-specific effects of stresses were minimal by 24 hours in mice with aortic constriction surgery (Spruill, et al. 2008). Additionally, the use of sham-operated controls in our study likely reduced the errors in our interpretation due to unknown effects of surgery-related stresses.

2.4.2 Role of Angiotensin II and AT_1 Receptors in Pressure Overload-Induced Electrical Remodeling

As previously discussed, the role of AT_1 receptors in the development of pressure overload-induced cardiac hypertrophy is well known. In this study, we presented evidence that suggests an additional role of the AT_1 receptors, specifically, pressure overload-induced downregulation of $I_{to,fast}$ and $I_{K,slow}$. Our results suggest that reductions in $I_{to,fast}$ and $I_{K,slow}$ in

response to pressure overload occur before the onset of hypertrophic growth and that reduced $I_{to,fast}$ and $I_{K,slow}$ are restored approximately to control values with the application of an AT_1 receptor blocker. Evidence of $I_{to,fast}$ and $I_{K,slow}$ restoration in short-term TAC myocytes but no significant rise in these currents in sham myocytes in response to AT_1 receptor blockade suggests that pressure overload-induced reductions in $I_{to,fast}$ and $I_{K,slow}$ can be attributed to AT_1 receptor stimulation. In previous studies, mechanical strain and AT_1 receptor activation have been related with two very distinct molecular mechanisms based on experimental observations. In one study, mechanical strain on cardiac myocytes *in vitro* induced autocrine secretion of angiotensin II (A2) that resulted in the induction of the hypertrophic program (Sadoshima, et al. 1993). A more recent study presented evidence for AT_1 receptor stimulation in response to mechanical stress without A2 (Zou, et al. 2004) suggesting mechano-sensitivity of AT_1 receptors as a potential mechanism to explain the relationship between mechanical strain and AT_1 receptor activation. However, the former mechanism (Sadoshima, et al. 1993) better explains our experimental results since the external application of an AT_1 receptor inhibitor is required to induce increases in $I_{to,fast}$ and $I_{K,slow}$ in isolated TAC myocytes, which are no longer subjected to strain. If mechano-sensitivity were to be the underlying mechanism, $I_{to,fast}$ and $I_{K,slow}$ in TAC myocytes should have been similar to control values since AT_1 receptor stimulation would have been inhibited when the cells were isolated and freed from mechanical strain.

Given that mechanical strain-induced release of autocrine A2 explains our results, we must address how A2 might retain its activity within isolated cells, which are no longer subjected to stress. One plausible explanation is that A2 secretion and re-uptake is localized mainly within the transverse tubules (t-tubules), which restricts the diffusion of A2 away from cells. In mammalian species, t-tubular membrane makes up a significant percentage of the total

membrane area that contacts the extracellular environment, with values of 39.6% in guinea pig left ventricle (Forbes and van Neil, 1988) and 32.6% in the rat left ventricle (Page, 1978). If the majority of AT_1 receptor stimulation was to take place within the t-tubules, one implication is that a significant percentage of $I_{to,fast}$ and $I_{K,slow}$ channels are also localized to the t-tubular membrane, especially if the channels co-internalize with AT_1 receptors (Doronin, et al. 2004). Localization of the majority of plasma membrane $I_{Ca,L}$ channels to t-tubules has been well documented (Kawai, et al. 1999) and has been suggested to be an important aspect of excitation-contraction coupling. One previous study also presented evidence for high Kv4.2 localization to the t-tubules, although these channels were appreciably detected in non-tubular membrane as well (Takeuchi, et al. 2000). It would certainly be of interest for the future to investigate the localization of AT_1 receptor mediated downregulation of $I_{to,fast}$ and $I_{K,slow}$ using detubulation methods on isolated myocytes.

2.4.3 Interpreting $I_{to,fast}$ and $I_{K,slow}$ Reductions

Marionneau, et al. (2008) made the suggestion, based on the lack of difference in $I_{to,fast}$ and $I_{K,slow}$ amplitudes between long-term sham and TAC myocytes, that the disparity in $I_{to,fast}$ and $I_{K,slow}$ densities between sham and TAC myocytes can be explained by the increase in cell size. This is in contrast with our experimental observations which indicate significant reductions in $I_{to,fast}$ and $I_{K,slow}$ densities between sham and TAC myocytes at 1 to 2 days of aortic banding, at which point cell size between the two groups were similar. Even at 1 to 2 weeks of aortic banding, when hypertrophy is evident, $I_{to,fast}$ amplitude was significantly lower and $I_{K,slow}$ amplitude was moderately lower in TAC myocytes. $I_{to,fast}$ amplitude in 1 to 2 week TAC myocytes were restored to sham values upon application of saralasin but minimal increases were

observed in $I_{K,slow}$ amplitude. These results suggest that pressure overload induces reduction of $I_{to,fast}$ primarily via AT_1 receptor stimulation and when hypertrophy occurs, the density of $I_{to,fast}$ is further reduced due to the increase in cell size with no change in how AT_1 receptors regulate the number of functional $I_{to,fast}$ channels. At early time points of pressure overload, $I_{K,slow}$ is similarly reduced by AT_1 receptor stimulation but our results indicate that AT_1 receptors have minimal involvement in regulating $I_{K,slow}$ once hypertrophy has set in. The reason for this is unclear but we hypothesize that it involves the synthesis and recruitment of new Kv1.5 and Kv2.1 channels to the membrane, as indicated by reports of increased surface expression of these channels in hypertrophied myocytes (Marionneau, et al. 2008). These new channels may not be coupled to AT_1 receptors, possibly due to their localization in the membrane, which may explain their insensitivity to AT_1 receptor activity. In the same report, Kv4.2 and Kv4.3 expression was relatively unchanged, which is consistent with our hypothesis.

2.4.4 Conclusions

This study suggests a novel mechanism of $I_{to,fast}$ and $I_{K,slow}$ downregulation, which exists as a precursor to pressure overload induced cardiac hypertrophy and heart failure. The suggested role of AT_1 receptors in altering electrophysiological currents is not completely surprising with the understanding that angiotensin converting enzyme (ACE) inhibitor and angiotensin receptor blocker (ARB) therapy is in widespread use for the treatment of heart disease (Scow, et al. 2003). This study provides the impetus for ongoing research into specific signaling mechanisms downstream of AT_1 receptors that are involved in the disease process and in doing so, more focused strategies for the treatment of heart failure, at early stages of disease progression, may be discovered.

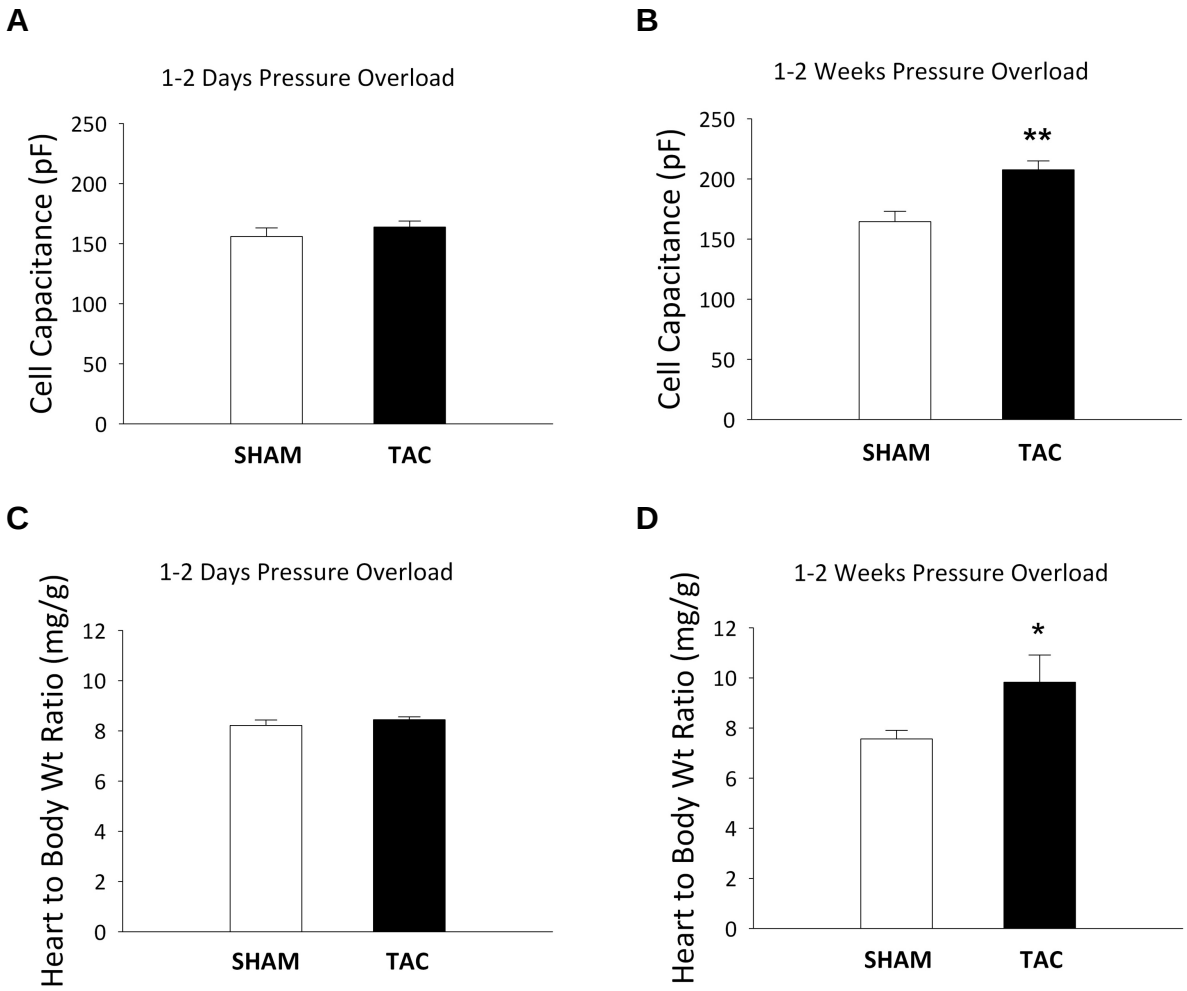

Figure 2.1: Whole-cell patch clamp measurements of cell capacitance (C_m) recorded from isolated left ventricular myocytes from mice that underwent sham or TAC surgery. Cells were harvested either 1 to 2 days or 1 to 2 weeks post-surgery. Mean C_m at 1 to 2 days (A) was similar for sham (n = 14) and TAC (n = 15) myocytes whereas at 1 to 2 weeks (B), C_m of TAC (n = 12) myocytes was significantly increased relative to sham (n = 14). Similarly, heart-to-body weight ratios (sham: n = 5; banded: n = 5) were unchanged at 1 to 2 days post-surgery (C) but were significantly higher in TAC mice (sham: n = 6; banded: n = 6) at 1 to 2 weeks (D), indicating that although long-term aortic constriction induces growth in cell size and cardiac hypertrophy, hearts subjected to short periods (1 to 2 days) of pressure overload do not undergo structural remodeling. Significance denoted by * ($p < 0.05$) and ** ($p < 0.001$).

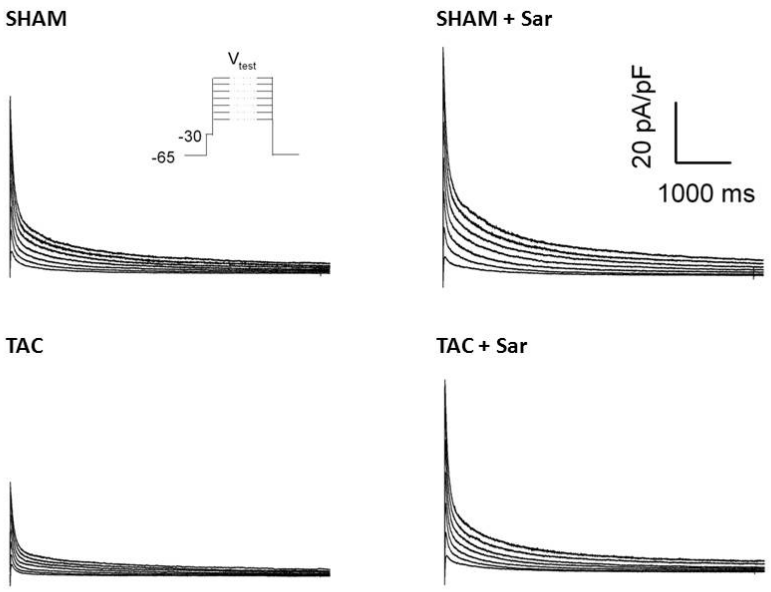

Figure 2.2: Representative whole-cell patch clamp traces of outward K^+ current recordings from mouse left ventricular myocytes. Mice that underwent TAC or sham surgery were sacrificed 1 to 2 days post-surgery and cells were obtained for electrophysiological recordings. Saralasin was applied to some sham and TAC myocytes. Inset on the left side depicts the voltage clamp protocol to obtain the current traces (V_{test}: test potential).

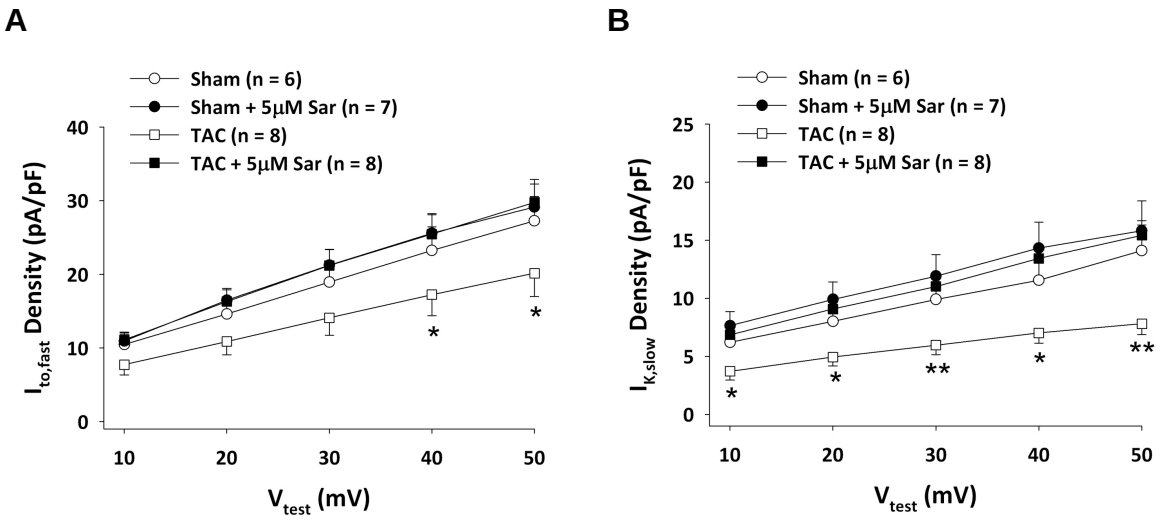

Figure 2.3: Voltage dependences of peak $I_{to,fast}$ (A) and $I_{K,slow}$ (B) densities measured from short-term sham and TAC myocytes. Additionally, sham and TAC myocytes were stimulated with saralasin to test for the involvement of AT_1 receptors. $I_{to,fast}$ and $I_{K,slow}$ were significantly reduced in TAC myocytes whereas the application of saralasin to these cells restored the levels of $I_{to,fast}$ and $I_{K,slow}$ to those of sham myocytes incubated with saralasin. Significant differences between TAC and sham values are indicated by * ($p < 0.1$) and ** ($p < 0.05$).

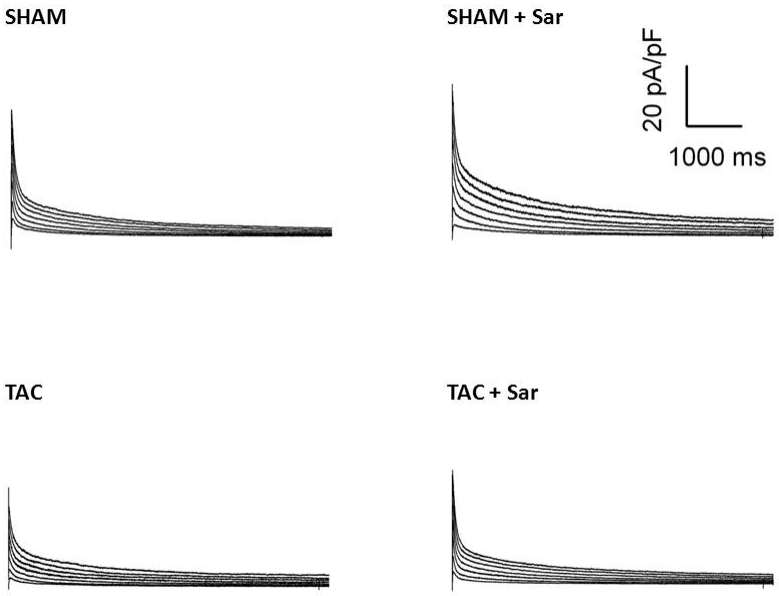

Figure 2.4: Representative whole-cell patch clamp traces of outward K^+ current recordings from long-term sham and TAC myocytes, including traces obtained from sham and TAC myocytes treated with saralasin.

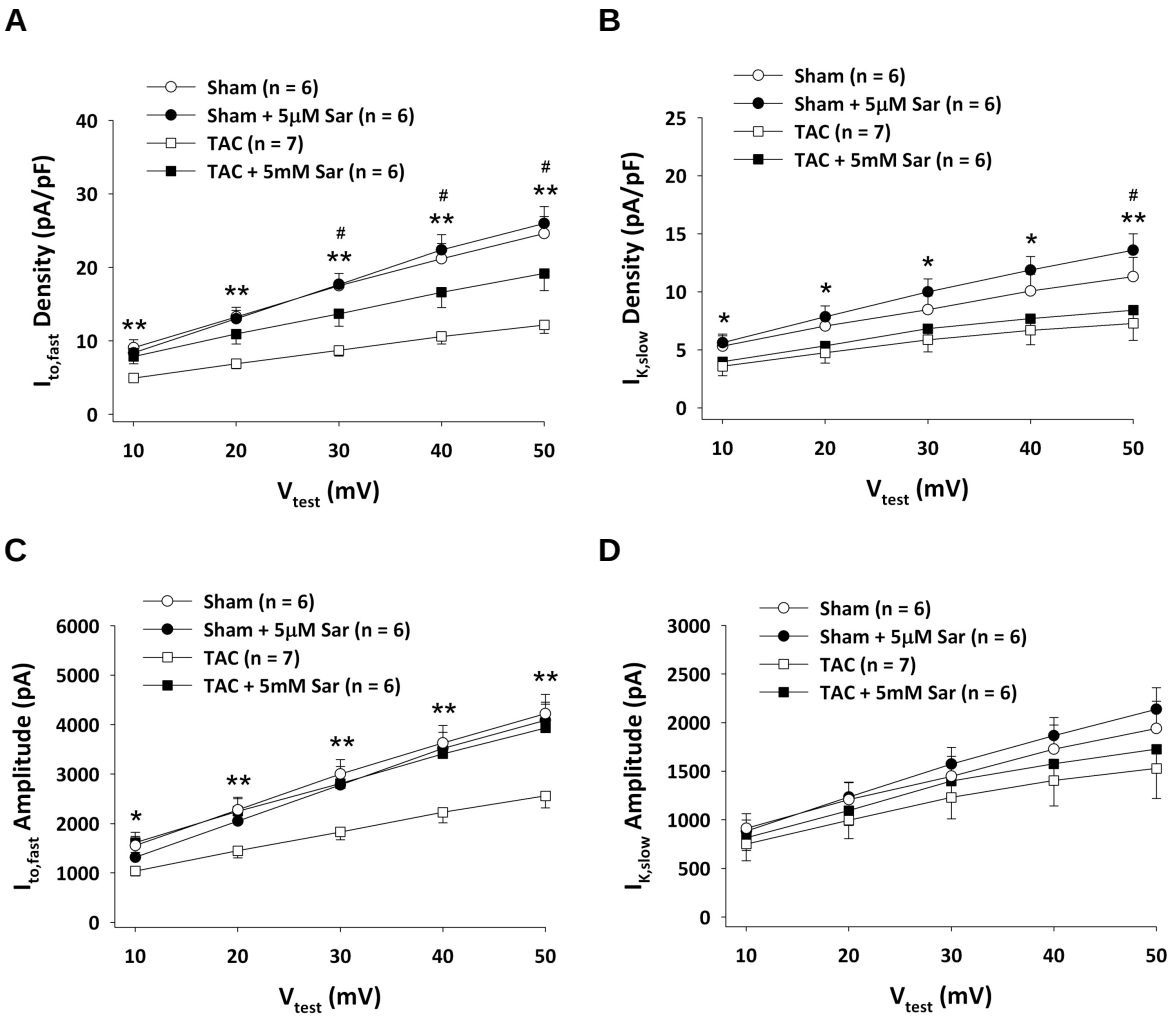

Figure 2.5: Voltage dependences of peak $I_{to,fast}$ (A) and $I_{K,slow}$ (B) densities measured from long-term sham and TAC myocytes. Additionally, sham and TAC myocytes stimulated with saralasin were included in this analysis. $I_{to,fast}$ and $I_{K,slow}$ densities were significantly reduced in cells subjected to 1 to 2 weeks of pressure overload but the application of saralasin to these cells only partially restored the level of $I_{to,fast}$ to those of control cells and did not significantly affect $I_{K,slow}$. Voltage dependences of peak $I_{to,fast}$ (C) and $I_{K,slow}$ (D) amplitudes indicate that saralasin fully restores $I_{to,fast}$ amplitude in TAC myocytes to control values but in contrast, does not appear to affect $I_{K,slow}$ amplitude. Significant differences between TAC and sham values are indicated by * ($p < 0.1$) and ** ($p < 0.05$) whereas differences between TAC+Sar and sham values are denoted by # ($p < 0.1$) and ## ($p < 0.05$).

Chapter 3

G Protein-Independent AT_1 Receptor-Mediated Electrical Remodeling in Cardiac Myocytes

3.1 Introduction

The angiotensin type 1 (AT_1) receptor is responsible for the transactivation of various intracellular signaling pathways that affect a number of different cellular phenotypes. The AT_1 receptor is a G protein coupled seven-pass transmembrane receptor that typically activates when it is agonist-bound. The primary agonist of the AT_1 receptor, the neuropeptide angiotensin II (A2), is an end-product of the renin-angiotensin system (RAS). A2 is classically known to exist as a pressure regulating neurohormone in vasculature but an increasing number of reports have demonstrated local production and secretion of A2 in cardiac tissue (Dostal, et al. 1992; Van Kats, et al. 1998) and A2 acting locally in cardiac myocytes via an autocrine mechanism (Sadoshima, et al. 1993).

Conventional AT_1 receptor activation involves G protein signaling and β-arrestin mediated receptor internalization. Upon receptor activation, the three subunits of the heterotrimeric G protein dissociate and activate downstream effectors including phospholipase C (PLC) which leads to inositol-1,4,5-triphosphate (IP_3) and diacylglycerol (DAG) production. DAG is known to activate protein kinase C (PKC) which exerts various downstream effects. One of the major phenotypic changes that result from G protein activation, in particular from the activity of the $G\alpha_q$ subtype, is the development of cardiac hypertrophy and failure (D'Angelo, et al. 1997; Adams, et al. 1998). Another well-described aspect of AT_1 receptor signaling involves β-arrestin mediated receptor internalization. Many classes of plasma membrane receptors, including the AT_1 receptor, undergo internalization in clathrin-coated vesicles to exert various cellular effects (Brown, et al. 1991). AT_1 receptors having point mutations that effectively block G protein signaling have been used by researchers to show that AT_1 receptor internalization can be retained with normal kinetics independent of G protein activation (Hunyady, et al. 1994;

Feng, et al. 2005). More recently, wild type AT_1 receptors were stimulated using a "biased agonist"—an analog of A2 with substituted side-chains—that selectively activated β-arrestin2 dependent signals and receptor internalization without G protein stimulation (Holloway, et al. 2002; Wei, et al. 2003). It has been suggested that the interaction between the receptor and a biased agonist induces a distinct conformation of the receptor that differs from the conventional receptor conformation induced by A2. In this way, biased agonists may alter the interactions of the receptor with certain downstream signaling molecules, in effect blunting certain pathways while preserving or even enhancing others.

The discovery of biased agonists affords investigators with a unique opportunity to study and reveal molecular mechanisms underlying a particular phenotype associated with AT_1 receptor activation. Numerous reports have shown that activation of the AT_1 receptor is involved in both electrical (Yu, et al. 2000; Rivard, et al. 2008; Shimoni, 2001; Wang, et al. 2008; Matsuda, et al. 2004; Ichiyanagi, et al. 2002; Aiello, et al. 2001) and structural (Sadoshima and Izumo, 1993; Paradis, et al. 2000) remodeling of the heart but many of these phenotypic outcomes are regulated by different pathways downstream of AT_1 receptor activation. Cardiac hypertrophy typically involves heightened levels of G protein activity whereas β-arrestin2 activity supports proliferation of cardiac myocytes and does not induce hypertrophic growth (Aplin, et al. 2007). β-arrestin2 additionally mediates positive inotropic effects of the AT_1 receptor independent of G proteins (Rajagopal, et al. 2006) which may involve electrical remodeling mechanisms that are separate from those that are G protein dependent. For example, β-arrestin2 dependent signaling may induce co-internalization of the AT_1 receptor with voltage-gated K^+ channels Kv4.3 in the heart (Doronin, et al. 2004). Electrical remodeling, such as the

removal of Kv4.3 from the surface membrane, can profoundly affect cardiac function by changing the shape and duration of the action potential and by altering $[Ca^{2+}]_i$ dynamics.

The previous chapter presented evidence suggesting the AT_1 receptor mediates mechanical stress induced reductions in transient outward K^+ currents (I_{to}) in mouse left ventricular (LV) myocytes. The present study focuses on the mechanisms by which AT_1 receptor activation results in electrical remodeling involving the downregulation of I_{to}. Our results indicate that two distinct I_{to} currents ($I_{to,fast}$ and $I_{K,slow}$) are coherently modulated by A2 in a dose dependent manner and that A2 induced changes in these currents are likely the result of β-arrestin2 dependent AT_1 receptor internalization.

3.2 Materials and Methods

3.2.1 Isolation of Left Ventricular Myocytes

Wild type mice (7 to 16 weeks old) were euthanized via CO_2 inhalation in an enclosed chamber. Using surgical scissors, the chest cavity was exposed and the heart was gently excised and immediately transferred into a 35 mm dish filled with ice-cold Normal Tyrode Solution containing (in mM) 137.7 NaCl, 2.3 NaOH, 5.4 KCl, 1 $MgCl_2$, 10 Glucose and 5 HEPES (pH adjusted to 7.4 with NaOH). The lungs and thymus were removed and adipose tissues surrounding the aorta were carefully cleaned off using small scissors to expose the aorta. To cannulate the aorta, the tip of a non-beveled needle was inserted in the aorta and tied together with a 5-0 gauge nylon suture. The heart was then connected to a temperature-controlled Langendorf perfusion apparatus that allows solution switching. The heart was first perfused with Normal Tyrode Solution at 37°C for 2 to 3 minutes to wash out residual blood in the coronary vessels. Perfusion was then switched to a Normal Tyrode Solution containing 0.16 mg/ml

Liberase TH (Roche Applied Science, Inc.) for 9 to 10 minutes or until the perfusion speed dramatically increased, which indicated sufficient tissue digestion. The cannula with heart attached was then removed and KB solution containing (in mM) 83 KCl, 30 K_2HPO_4, 5 $MgSO_4$, 5 Na-Pyruvic Acid, 5 β-OH-Butyric Acid, 5 Creatine, 20 Taurine, 10 Glucose, 0.5 EGTA and 5 HEPES (pH adjusted to 7.2 with HCl) was manually perfused through the heart with a syringe to wash out the Liberase solution. The heart was placed in a dish containing KB solution and the left ventricle was separated from the rest of the heart. The left ventricle was gently teased apart by mechanical agitation and filtered through a nylon mesh to collect the cell suspension. The isolated myocytes were stored in KB solution at 22°C for up to 12 hours while electrophysiological recordings were being obtained.

3.2.2 Cell Preparation

For each set of experiments, the cell suspension was divided into control and experimental groups for comparison. Cells in the experimental groups were treated for 2 to 12 hours with A2 (Sigma-Aldrich Inc.) at various concentrations ranging from 50 nM to 10 µM or with 5 µM SII ([Sar^1-Ile^4-Ile^8]AngII) which was obtained from the Cleveland Clinic Core Facility (Cleveland, OH). In some experiments, 5 µM colchicine (Sigma-Aldrich Inc.) was applied to both the control and experimental groups 2 hours before the addition of A2.

3.2.3 Electrophysiological Recordings

Whole-cell patch clamp experiments were conducted at room temperature (22°C) within 12 hours of cell isolation. For both K^+-current and action potential measurements, the internal pipette solution contained (in mM) 115 K-Aspartic Acid, 25 KOH, 10 KCl, 3 $MgCl_2$, 11 EGTA,

10 HEPES and 5 Na_2-ATP (pH adjusted to 7.2 with KOH). Pipette series resistances were between 4-7 MΩ in whole-cell mode. For K^+-current measurements, myocytes were perfused with an external solution containing (in mM) 137.7 NaCl, 2.3 NaOH, 5.4 KCl, 1 $MgCl_2$, 1.8 $CaCl_2$, 2 $CoCl_2$, 10 Glucose and 5 HEPES (pH adjusted to 7.4 with NaOH). For action potential recordings, $CoCl_2$ was omitted from the external solution.

Both voltage-clamp and current-clamp experiments were performed using an Axopatch 1D amplifier (Axon Instruments Inc.) interfaced to a computer with a Digidata 1200 digitizer and pClamp 8.2 software (Axon Instruments Inc.). In current-clamp mode, action potentials were elicited with short depolarizing current injections (~2 ms) at a frequency of 2.5 Hz (lower stimulation frequencies did not significantly alter the shape of the action potential). In voltage-clamp mode, K^+ currents were measured in response to a short prepulse (10 ms) to -30mV to inactivate Na^+ channels followed by 6000 ms voltage steps (V_{test}) between +10 mV and +50 mV from a holding potential of -65 mV. For all voltage-clamp recordings, series resistances were compensated electronically by ~85%.

3.2.4 Data Analysis and Statistics

Voltage- and current-clamp data were analyzed using Clampfit 8.2 (Axon Instruments Inc.), Microsoft Excel 7 (Microsoft Inc.), SigmaPlot 10 (Systat Software Inc.) and MATLAB (various versions, Mathworks Inc.). Action potential durations to 50% and 90% repolarization (APD_{50} and APD_{90}, respectively) were accurately determined using MATLAB. Distinct K^+ current components ($I_{to,fast}$, $I_{K,slow}$ and I_{sus}) were extracted from the obtained K^+ current recordings using the Curve Fitting Toolbox in MATLAB to fit a two-exponential decay function in the form of $A_1\exp(-t_1/\tau_1)+A_2\exp(-t_2/\tau_2)+A_3$ (Xu, et al. 1999). A_1 and A_2 represent peak

amplitudes of $I_{to,fast}$ and $I_{K,slow}$ and their respective inactivation time constants differ by a factor of approximately 20. $I_{to,fast}$ was identified as the inactivating component with a decay time constant less than 100 ms and $I_{K,slow}$ was identified as the slower inactivating component (τ_{decay} > 1000 ms). A_3 represents the steady-state component I_{sus}. Peak current amplitudes were normalized to the cell capacitance (C_m), which was measured in each cell using the Membrane Test function in the pClamp software, and presented as current densities (pA/pF).

Differences in action potential characteristics and K^+ current amplitudes between control and experimental cells were assessed with the Student's *t*-test. Percentage inhibitions in $I_{to,fast}$ and $I_{K,slow}$ were plotted as functions of A2 concentration and sigmoidal dose-response curves were fitted to the data using SigmaPlot.

3.3 Results

3.3.1 A2 Dose Dependent Action Potential Prolongation

The action potential morphology is a global representation of the activity of membrane currents in a single cell. We measured action potentials from cells stimulated with externally applied A2 to demonstrate that one or more membrane currents are altered dose dependently in response to A2. Representative action potential recordings obtained from control (CON) LV myocytes that were compared with recordings from LV cells incubated in the presence of 100 nM A2 and 5 μM A2 for 2 to 12 hours are presented in Fig 3.1A. From these traces, it is evident that LV myocytes display A2 concentration dependent prolongation in action potential duration. Action potential durations in both early and late phase repolarization (APD_{50} and APD_{90}, respectively) exhibit increases that are commensurate with an increased dosage of externally applied A2 (Fig 3.1B). The mean ± S.E.M. values of APD_{50} we obtained were 3.82 ± 0.30 ms (n

= 20), 5.19 ± 0.76 ms (n = 19) and 6.61 ± 1.08 ms (n = 22) for CON, 100nM A2 and 5 µM A2 cells, respectively. A similar trend in APD_{90} was observed as well (16.21 ± 1.17 ms, 21.18 ± 2.63 ms and 25.37 ± 3.28 ms for CON, 100nM A2 and 5 µM A2 cells, respectively). A2 dose dependent prolongation of the action potential was not accompanied by changes in either the resting potential, V_{rest} (Fig 3.1C) or the peak potential, V_{max} (Fig 3.1D). The data indicates A2 stimulation in LV myocytes triggers the remodeling of one or more underlying membrane currents that significantly contribute to action potential repolarization delay.

3.3.2 Conserved Voltage Dependence of $I_{to,fast}$ and $I_{K,slow}$ in A2 Stimulated LV Cells

Having demonstrated that stimulation of LV cells with varying concentrations of A2 results in dose dependent prolongations in the action potential, we sought to understand how A2 affects the voltage dependence and magnitude of repolarizing K^+ currents. LV cells were incubated for 2 to 12 hours with various concentrations (50 nM to 10 µM) of A2 and cells with clear striations were chosen at random for the whole-cell patch clamp experiments. Voltage clamp recordings obtained from cells incubated with a given concentration of A2 were compared with recordings measured in CON cells from the same population of cells. Representative traces depicting the difference in the total outward current between CON and 5 µM A2 cells are displayed in Fig 3.2A. A voltage clamp protocol consisting of 6-s depolarizing test potentials between +10 and +50 mV from a holding potential of -65 mV caused a rapid, transient increase in the outward current that was consistent with K^+ currents that have been described previously in mouse left ventricular myocytes (Xu, et al. 1999). $I_{to,fast}$ and $I_{K,slow}$ were separated from these traces as described in MATERIALS AND METHODS and their peak current densities were averaged and plotted as a function of the test potential (V_{test}). As an example, peak $I_{to,fast}$ and

$I_{K,slow}$ current-voltage relationships obtained from CON vs 5 μM A2 cells are presented in Fig 3.2B and 3.2C.

To assess A2 induced changes in the voltage dependences of $I_{to,fast}$ and $I_{K,slow}$, peak current amplitudes measured from CON cells (n = 8) and cells treated with 5 μM A2 (concentration at which $I_{to,fast}$ and $I_{K,slow}$ display near-maximal inhibition , n = 8) were compared. A2 induced percent inhibitions of $I_{to,fast}$ and $I_{K,slow}$ were calculated by taking the difference in the mean current amplitude at every test potential between CON and A2 groups and dividing the difference by the mean of the CON group. A2 induced percent inhibitions at test potentials between +10 and +50 mV are shown in Fig 3.3A ($I_{to,fast}$) and 3.3B ($I_{K,slow}$). On average, peak currents in A2 stimulated cells were 34.5 ± 11.4% and 43.3 ± 10.3% inhibited for $I_{to,fast}$ and $I_{K,slow}$, respectively, with minimal deviations at each test potential. This indicates that the voltage dependences of $I_{to,fast}$ and $I_{K,slow}$ are unshifted despite the reductions in their peak amplitude. These results suggest that A2 induces reductions in the number of functional K^+ channels per unit area of surface membrane, hence a reduction in channel density, without altering channel properties.

3.3.3 Coherent Regulation of $I_{to,fast}$ and $I_{K,slow}$ in A2 Stimulated LV Cells

Table 3.1 displays peak $I_{to,fast}$ and $I_{K,slow}$ current densities and their respective inactivation time constants ($\tau_{to,fast}$ and $\tau_{K,slow}$, respectively) measured in response to V_{test} = +50 mV in LV cells incubated with varying [A2]. Relative changes (%) in peak $I_{to,fast}$ and $I_{K,slow}$ at V_{test} = +50 mV were plotted as a function of [A2] and sigmoidal dose-inhibition curves were fit to the data as shown in Fig 3.4. The dose-inhibition relationships reveal that in LV cells stimulated with saturating [A2], the peak $I_{to,fast}$ and $I_{K,slow}$ densities are attenuated by 41% and 47%, respectively.

Additionally, the half maximal inhibitory concentration (IC_{50}) of A2 for $I_{to,fast}$ (400 nM) and $I_{K,slow}$ (368 nM) appear to be similar and may be identical given experimental variability. Likewise, the 90%-maximal inhibitory concentrations (IC_{90}) were also similar ($I_{to,fast}$: 1643 nM, $I_{K,slow}$: 1462 nM). These findings indicate that A2 stimulation coherently attenuates $I_{to,fast}$ and $I_{K,slow}$ in a dose dependent manner which suggests the mechanisms underlying the regulation of these two currents are similar, if not the same.

3.3.4 Colchicine Inhibition of AT_1 Receptor Mediated Electrical Remodeling

Having established that AT_1 receptor stimulation modulates $I_{to,fast}$ and $I_{K,slow}$ densities, we sought to understand whether or not this activity depends on intracellular trafficking. To test whether A2 induced electrical remodeling involves receptor and/or channel endocytosis and intracellular trafficking, colchicine was applied to some LV cells 2 hours prior to A2 treatment. Colchicine disrupts vesicular transport by binding to tubulin and inhibiting microtubule polymerization. Fig 3.5 presents the effect of colchicine on A2 induced electrical remodeling in LV myocytes. Fig 3.5A shows representative action potential traces obtained from untreated (Control), colchicine treated, A2 treated and both colchicine and A2 treated cells. Compared with action potential durations (APD_{50} and APD_{90}) measured from CON cells (APD_{50}: 4.59 ± 0.64 ms and APD_{90}: 24.33 ± 2.15 ms, n = 6), A2 treated cells displayed significant prolongations in both APD_{50} (8.61 ± 1.37 ms, n = 6) and APD_{90} (40.40 ± 7.95 ms, n = 6) whereas no significant deviations were observed in either colchicine treated (APD_{50}: 4.85 ± 1.05 ms and APD_{90}: 24.65 ± 4.39 ms, n = 6) or colchicine/A2 treated (APD_{50}: 4.29 ± 0.40 ms and APD_{90}: 23.43 ± 5.04, n = 6) groups (Fig 3.5B and 3.5C). Though colchicine alone appears to have no effect on the action potential, pre-incubation with colchicine blocks A2 induced changes in action potential

morphology. These findings demonstrate that pharmacological inhibition of microtubule assembly and the ensuing disruption of vesicular trafficking alters the normal activity of AT_1 receptors possibly by retaining them within the membrane and disallowing receptor internalization. Another possibility is that certain ion channels including those responsible for $I_{to,fast}$ and $I_{K,slow}$ internalize upon A2 stimulation under normal conditions and disruption of the microtubule network prevents the removal of these channels from the surface membrane. Either possibility is consistent with our data, or perhaps both if receptor and channels are co-internalized upon receptor activation.

3.3.5 AT_1 Receptor Mediated Electrical Remodeling via G Protein Independent Biased Signaling

AT_1 receptor activation stimulates both G protein dependent and independent pathways in which the latter involves β-arrestin2 dependent signaling that includes receptor internalization and desensitization. Having shown data suggesting AT_1 receptor mediated electrical remodeling is dependent on intracellular trafficking, we aimed to understand whether AT_1 receptor activation without G protein stimulation can induce A2-like effects in LV cells. To demonstrate G protein independence in AT_1 receptor mediated electrical remodeling, cells were incubated with 5 μM SII ([Sar^1-Ile^4-Ile^8]AngII) which selectively activates β-arrestin2 dependent signaling and resulting receptor internalization without G protein stimulation (Holloway, et al. 2002; Wei, et al. 2003). Action potentials were elicited from CON and SII treated cells and the voltage traces were analyzed and compared. As shown in Fig 3.6, action potentials from SII treated cells were significantly prolonged compared with controls (CON (n=6): 4.26 ± 0.53 ms and SII (n=6): 5.89 ± 0.51 ms for APD_{50}; CON: 17.55 ± 1.70 ms and SII: 33.81 ± 5.39 ms for APD_{90}), similar to the

prolongations observed in cells treated with A2 (Fig 3.1). These results suggest β-arrestin2 dependent AT_1 receptor mediated electrical remodeling without the involvement of G proteins. Additionally, K^+ currents were recorded from CON (n = 6) and SII treated (n = 7) cells to examine the effect of the biased agonist on peak $I_{to,fast}$ and $I_{K,slow}$. K^+ currents were recorded in response to 6-s voltage steps between +10 and +50 mV from a holding potential of -65 mV (Fig 3.7). Compared with CON cells, peak $I_{to,fast}$ and $I_{K,slow}$ densities were considerably attenuated in SII treated cells ($I_{to,fast}$: -37%, $I_{K,slow}$: -36% at V_{test} = +50 mV), the loss of which may contribute to the delay in the repolarization of the action potential.

3.4 Discussion

3.4.1 Summary of Results

The experiments presented here reveal dose-dependent electrical remodeling in response to varying levels of AT_1 receptor stimulation involving reductions in K^+ current densities and action potential prolongation. In LV myocytes, action potential duration increased commensurate with increasing concentrations of externally applied A2. Additionally, varying levels of A2 stimulation reduced two distinct transient outward K^+ currents $I_{to,fast}$ and $I_{K,slow}$ in a coherent manner without changing their voltage dependence. These findings suggest AT_1 receptor mediated electrical remodeling involves reductions in the number of functionally expressed ion channels, which include $I_{to,fast}$ and $I_{K,slow}$ channels, in the surface membrane and this hypothesis prompted additional experiments to investigate the mechanisms underlying the regulation of these channels. LV cells pre-incubated in colchicine, an inhibitor of microtubule polymerization, blocked A2 induced action potential prolongation which suggests that AT_1 receptor mediated regulation of ion channels requires the availability of intracellular trafficking.

These findings additionally implicate a role for β-arrestin2 dependent receptor internalization and not G protein signaling in AT_1 receptor mediated electrical remodeling. To test for G protein independence in AT_1 receptor mediated electrical remodeling, biased agonist SII, which activates AT_1 receptors without G protein stimulation, was applied to LV cells and the ensuing effects on action potential morphology and $I_{to,fast}/I_{K,slow}$ were observed. Significant action potential prolongation and downregulation of $I_{to,fast}$ and $I_{K,slow}$ were documented in LV cells and these findings support the notion that AT_1 receptor mediated electrical remodeling may be G protein independent.

3.4.2 A2 Induced Electrical Remodeling Involves Reductions in $I_{to,fast}$ and $I_{K,slow}$

In mouse LV myocytes, we observed A2 dose dependent prolongations in action potential duration at early (APD_{50}) and late (APD_{90}) repolarization (Fig 3.1). Effects of A2 stimulation on action potential morphology have been documented from various species including canine LV (Yu, et al. 2000), rat LV (Matsuda, et al. 2004), guinea pig LV (Wang, et al. 2008) and rabbit ventricle (Ichiyanagi, et al. 2002). Due to interspecies differences in action potential morphology, an ideal method of comparing our data with these previous studies eludes us. Certain trends in action potential prolongation, however, are consistent with our results. In canine LV, incubation of A2 for 2 to 52 hours abolished the characteristic phase 1 notch in the epicardial action potential which was attributed to a drastic reduction and alteration of I_{to} properties (Yu, et al. 2000). In rabbit ventricular myocytes, application of 1 μM A2 gradually prolonged the action potential before achieving a steady level at 20 to 30 min of exposure (Ichiyanagi, et al. 2002). Similar increases were observed in guinea pig LV (Wang, et al. 2008), though application of 1 μM A2 did not appear to have an effect in rat LV (Matsuda, et al. 2004)

despite similar patterns of ion channel expression as that of the mouse. This lack of A2 effect may be explained by the short duration (10 min) of exposure to A2 which may not have been sufficient to induce significant remodeling. Indeed, various outcomes of AT_1 receptor activation are not only agonist-specific but also stimulation time dependent (Aplin, et al. 2009).

Previous reports have demonstrated reductions in peak I_{to} in both atrial (Gassanov, et al. 2006) and ventricular (Yu, et al. 2000) myocytes in response to sustained A2 stimulation *in vitro* at micromolar concentrations. Our experimental data obtained from mouse LV myocytes are consistent with these findings and further demonstrate that A2 induces downregulation of a plurality of K^+ currents in a coherent manner (Fig 3.4). Known molecular correlates of K^+ currents in mouse LV include Kv4.2 and Kv4.3 which mediate $I_{to,fast}$ (Guo, et al. 2005; Guo, et al. 2002) and Kv1.5 and Kv2.1 which mediate $I_{K,slow}$ (London, et al. 2001; Xu, et al. 1999). Altered surface expression of two or more of these channels may explain the reductions in $I_{to,fast}$ and $I_{K,slow}$ that we observed but it is still unclear as to which, if not all, are involved. Our experiments indicate no shifts in the voltage-dependence in $I_{to,fast}$ or $I_{K,slow}$ as evidenced by a consistent percentage of peak current inhibition at various test potentials (Fig 3.3). These results differ from A2 induced I_{to} reductions observed in canine LV (Yu, et al. 2000) which were accompanied by a positive shift in the voltage dependence. The reasons for these differences are unknown but may be the result of A2 stimulation at high concentrations (> 0.5 μM) for longer durations (> 12 hours) in canine LV myocytes.

3.4.3 A2 Induced Reductions in $I_{to,fast}$ and $I_{K,slow}$ Involve G Protein Independent AT_1 Receptor Internalization

In addition to I_{to}, previous reports of A2 induced electrical remodeling in cardiac myocytes include changes in $I_{Ca,L}$ (Ichiyanagi, et al. 2002; Aiello, et al. 2001), the rapid component of the delayed rectifier K^+ current (I_{Kr}) (Wang, et al. 2008) and I_{sus} (Matsuda, et al. 2004). Taken together, these experiments reveal that different ion channels possess disparate time dependent responses to A2 stimulation. According to the literature, $I_{Ca,L}$, I_{Kr} and I_{sus} change in response to short term (5 to 10 min) exposure to A2 whereas $I_{to,fast}$ and $I_{K,slow}$ remodeling requires longer incubation times (> 30 min). These differences in time dependence may reflect the involvement of separate AT_1 receptor signaling pathways in regulating various types of ion channel currents. AT_1 receptor stimulation has been classified into two time dependent phases of receptor activation (Aplin, et al. 2009). The 'first wave' of signaling consists of G protein dependent activity which is terminated upon recruitment of β-arrestins to the receptor. Subsequently, β-arrestins mediate localization of AT_1 receptors to clathrin-coated pits for internalization and initiate a 'second wave' of signaling involving various effectors. Therefore, it is reasonable to postulate that $I_{Ca,L}$, I_{Kr} and I_{sus} respond to the first wave of signaling which involves G protein activity while $I_{to,fast}$ and $I_{K,slow}$ are affected primarily by β-arrestin dependent activity which includes receptor internalization. Indeed, A2 induced modulations in $I_{Ca,L}$, I_{Kr} and I_{sus} were shown to be dependent on PKC (Aiello, et al. 2001; Wang, et al. 2008; Matsuda, et al. 2004) which is a downstream effector of G protein activation. To demonstrate that A2 induced regulation of $I_{to,fast}$ and $I_{K,slow}$ involves AT_1 receptor internalization which is known to be G protein independent, intracellular trafficking was disabled with colchicine and then A2 effects were examined. A2 induced prolongations of the action potential were inhibited in cells

pretreated with colchicine (Fig 3.5) suggesting that A2 induced regulation of $I_{to,fast}$ and $I_{K,slow}$, which are the dominant repolarizing currents in mouse LV (Sah, et al. 2003), is dependent on receptor and/or channel internalization. Furthermore, cells stimulated with a biased agonist (SII) that activates AT_1 receptors without G protein stimulation displayed action potential prolongation and reductions in both $I_{to,fast}$ and $I_{K,slow}$ that were similar to the actions of A2 (Fig 3.6 and 3.7). These results further support the hypothesis that A2 induced reductions in $I_{to,fast}$ and $I_{K,slow}$ are dependent on AT_1 receptor signals that do not involve G proteins and hence are likely to depend on β-arrestin2 mediated receptor internalization.

3.4.4 Conclusions

Results from our study suggest that activation of AT_1 receptors in the heart will coordinately downregulate $I_{to,fast}$ and $I_{K,slow}$ and prolong the action potential via a G protein independent mechanism that potentially involves the trafficking and sequestration of the AT_1 receptors. Our findings demonstrate the importance of not only recognizing AT_1 receptors in the heart as regulators of electrical activity, in addition to their well-established role in cardiac hypertrophy and heart failure, but recognizing that certain phenotypic outcomes of the AT_1 receptor, such as hypertrophy and electrical remodeling, depend on different downstream signals that can be differentially triggered with biased agonists. Future work will focus on the long term benefits and detriments associated with biased activation of the AT_1 receptor, in particular the effects of K^+ current downregulation and action potential prolongation which are typically associated with malignant arrhythmias and heart failure.

[A2]	*50 nM*		*100 nM*		*200 nM*		*300 nM*	
	CON	*A2*	*CON*	*A2*	*CON*	*A2*	*CON*	*A2*
$I_{to,fast}$ (pA/pF)	35.7 ± 3.6	30.9 ± 4.7	38.7 ± 3.9	38.0 ± 3.2	34.1 ± 3.1	28.5 ± 6.5	35.7 ± 3.6	31.7 ± 4.1
τ_{fast} (ms)	94.8 ± 4.3	86.9 ± 5.1	71.3 ± 3.3	70.1 ± 6.0	66.4 ± 5.5	60.2 ± 2.3	94.8 ± 4.3	86.6 ± 5.1
$I_{K,slow}$ (pA/pF)	19.1 ± 1.8	15.3 ± 1.8	17.2 ± 2.5	15.6 ± 2.7	15.6 ± 1.0	14.5 ± 2.7	19.1 ± 1.8	15.5 ± 2.8
τ_{slow} (ms)	1418.4 ± 68.8	1455.6 ± 43.8	1280.4 ± 81.1	1324.3 ± 41.0	1277.9 ± 12.8	1326.1 ± 68.3	1418.4 ± 68.8	1530.5 ± 82.3
n	5	5	8	8	6	6	5	5

1 µM		*2 µM*		*5 µM*		*10 µM*	
CON	*A2*	*CON*	*A2*	*CON*	*A2*	*CON*	*A2*
34.1 ± 3.1	22.3 ± 5.4*	35.7 ± 3.6	23.2 ± 2.8**	38.7 ± 3.9	24.6 ± 6.2*	38.4 ± 4.0	23.1 ± 5.5**
66.4 ± 5.5	70.2 ± 6.2	94.8 ± 4.3	81.3 ± 2.0	71.3 ± 3.3	69.4 ± 5.2	77.2 ± 3.8	79.1 ± 5.9
15.6 ± 1.0	10.6 ± 2.0**	19.1 ± 1.8	8.3 ± 1.0**	17.2 ± 2.5	9.6 ± 1.6**	12.0 ± 0.8	7.5 ± 0.8**
1277.9 ± 12.8	1462.0 ± 99.7	1418.4 ± 68.8	1597.8 ± 38.0	1280.4 ± 81.1	1472.7 ± 81.5	1417.8 ± 47.0	1746.3 ± 97.8
6	6	5	5	8	8	7	6

* Denotes significant difference versus CON ($p < 0.09$)
** Denotes significant difference versus CON ($p < 0.05$)

Table 3.1: A2 dose dependent modulation of $I_{to,fast}$ and $I_{K,slow}$.

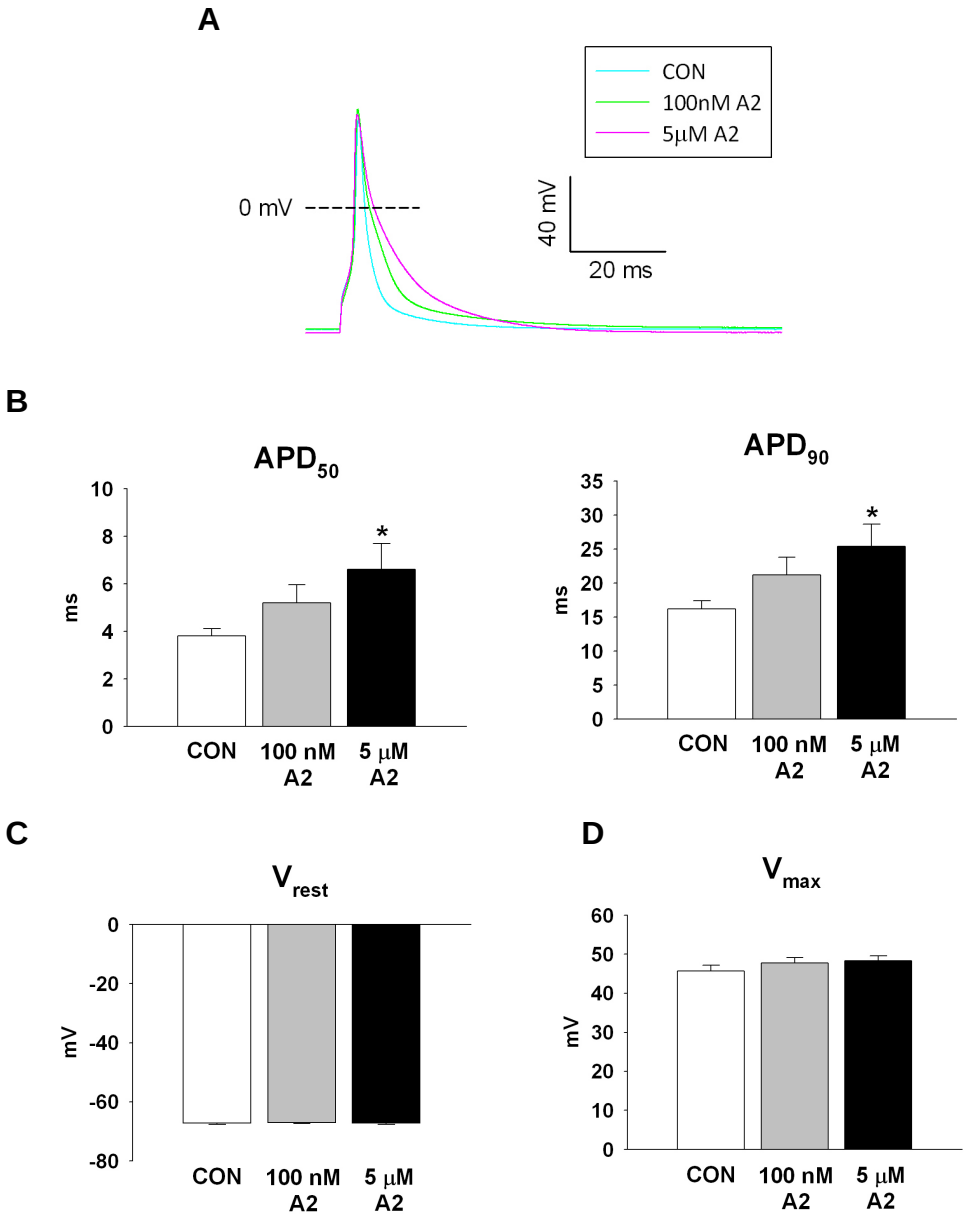

Figure 3.1: Dose dependence of A2 induced action potential prolongation. Representative action potential waveforms measured from LV myocytes incubated in the presence of either 100 nM A2 or 5 μM A2 for 2 to 12 hours (A). Action potentials display A2 dose dependent prolongation of early (APD_{50}) and late (APD_{90}) repolarization (B). A2 stimulated cells exhibit no significant changes in resting potential, V_{rest} (C) or peak potential, V_{max} (D). Bar graphs represent mean ± S.E.M. and significant differences relative to CON are denoted by * ($p < 0.05$).

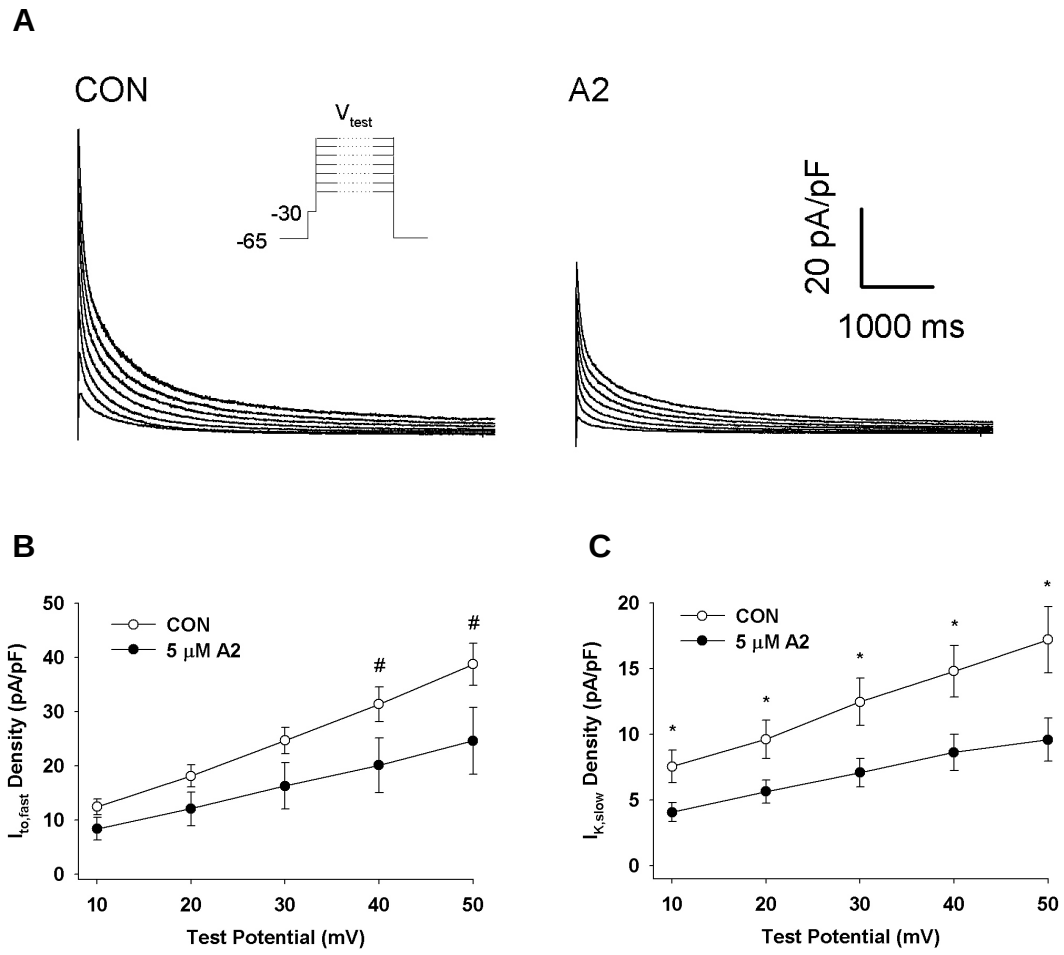

Figure 3.2: A2 induced reductions in $I_{to,fast}$ and $I_{K,slow}$. (A) Representative traces of total outward K^+ currents recorded from untreated (CON) LV myocytes and those treated with 5 μM A2 for 2 to 12 hours. Outward currents were elicited with 6-s test potentials ranging from -10 mV to +50 mV from a holding potential of -65 mV with a 10 ms prepulse to -30 mV to inactivate the fast Na^+ current, as shown in the inset. Voltage dependences of peak $I_{to,fast}$ (B) and $I_{K,slow}$ (C) densities extracted from the current traces. Significant reductions relative to CON are represented by * ($p < 0.05$) and # ($p < 0.09$).

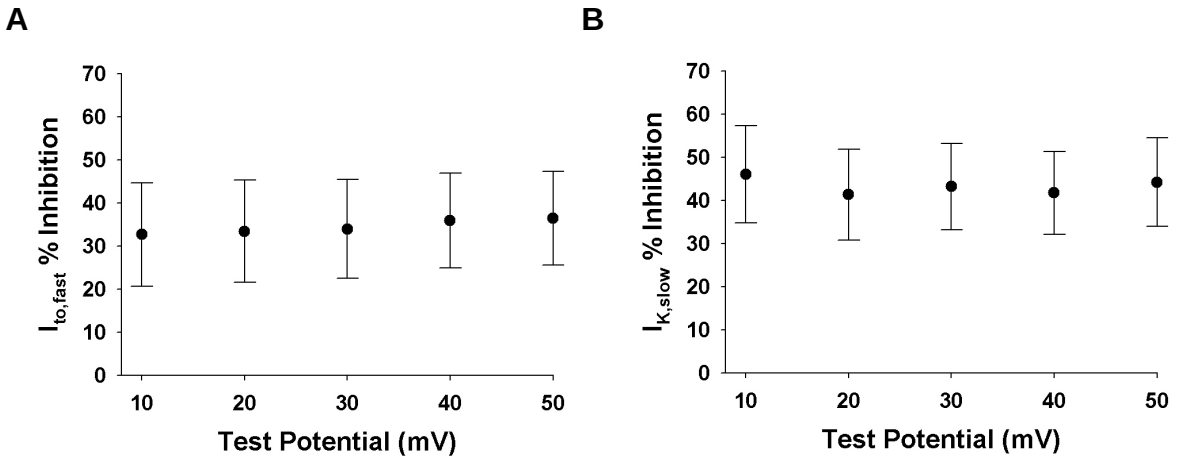

Figure 3.3: Unshifted voltage dependence of reduced peak $I_{to,fast}$ and $I_{K,slow}$ in A2 treated LV cells. Percent inhibitions of peak (A) $I_{to,fast}$ and (B) $I_{K,slow}$ exhibit minimal voltage dependence in 5 µM A2 treated cells suggesting that A2 induces reductions in the number of functional K^+ channels per unit area of surface membrane without altering channel properties. In (A) and (B), data points are presented as percent difference ± S.E. of the percent difference.

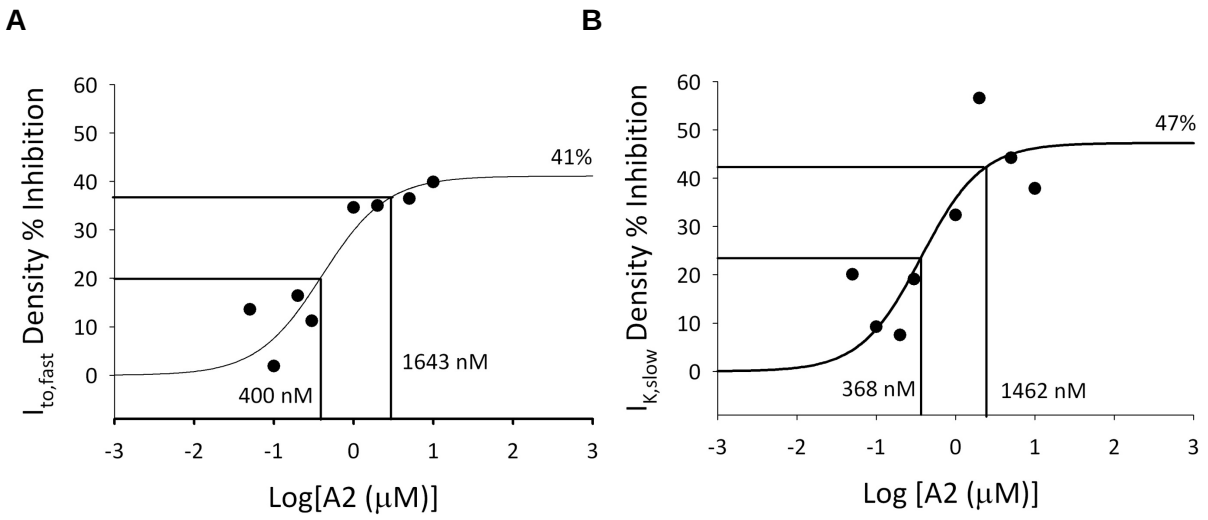

Figure 3.4: A2 effects on $I_{to,fast}$ and $I_{K,slow}$ dose inhibition relationships. Percent inhibitions induced by various concentrations (0.05 to 10 μM) were calculated from peak $I_{to,fast}$ and $I_{K,slow}$ values obtained at V_{test} = +50 mV (Table 3.1). Percent inhibition vs [A2] relationships of (A) $I_{to,fast}$ and (B) $I_{K,slow}$ were plotted and three-parameter sigmoidal curves were fit to the data. Based on the curve fits, half-maximal reductions of $I_{to,fast}$ and $I_{K,slow}$ correspond to A2 concentrations of 400 nM and 368 nM respectively, and 90%-maximal reductions correspond to 1643 nM and 1462 nM respectively, as indicated in the graphs. According to our analysis, stimulation with high [A2] can maximally inhibit $I_{to,fast}$ by 41% and $I_{K,slow}$ by 47%.

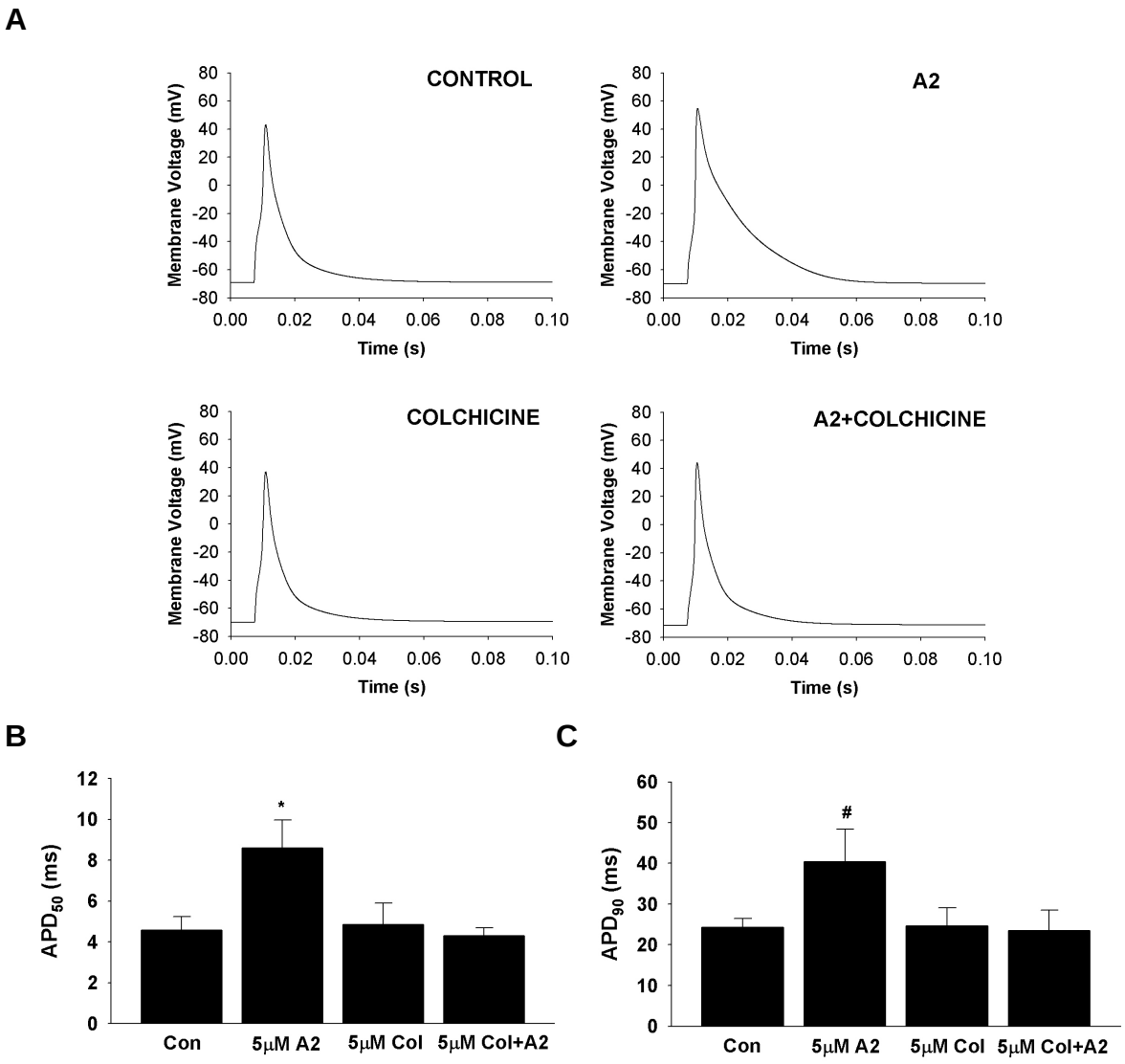

Figure 3.5: A2 induced electrical remodeling blocked in LV cells pretreated for 1 hour with colchicine. (A) Example traces of action potentials recorded from untreated, 5 μM colchicine treated, 5 μM A2 treated and both colchicine and A2 treated cells. Significant repolarization delays were observed in A2 treated myocytes as indicated by prolonged (B) APD_{50} and (C) APD_{90} but these effects were blocked in cells pretreated with colchicine. These results suggest that A2 induced electrical remodeling requires functioning intracellular transport mechanisms and may involve the internalization of AT_1 receptors, ion channels or both. Significant differences are represented by * ($p < 0.05$) and # ($p = 0.10$).

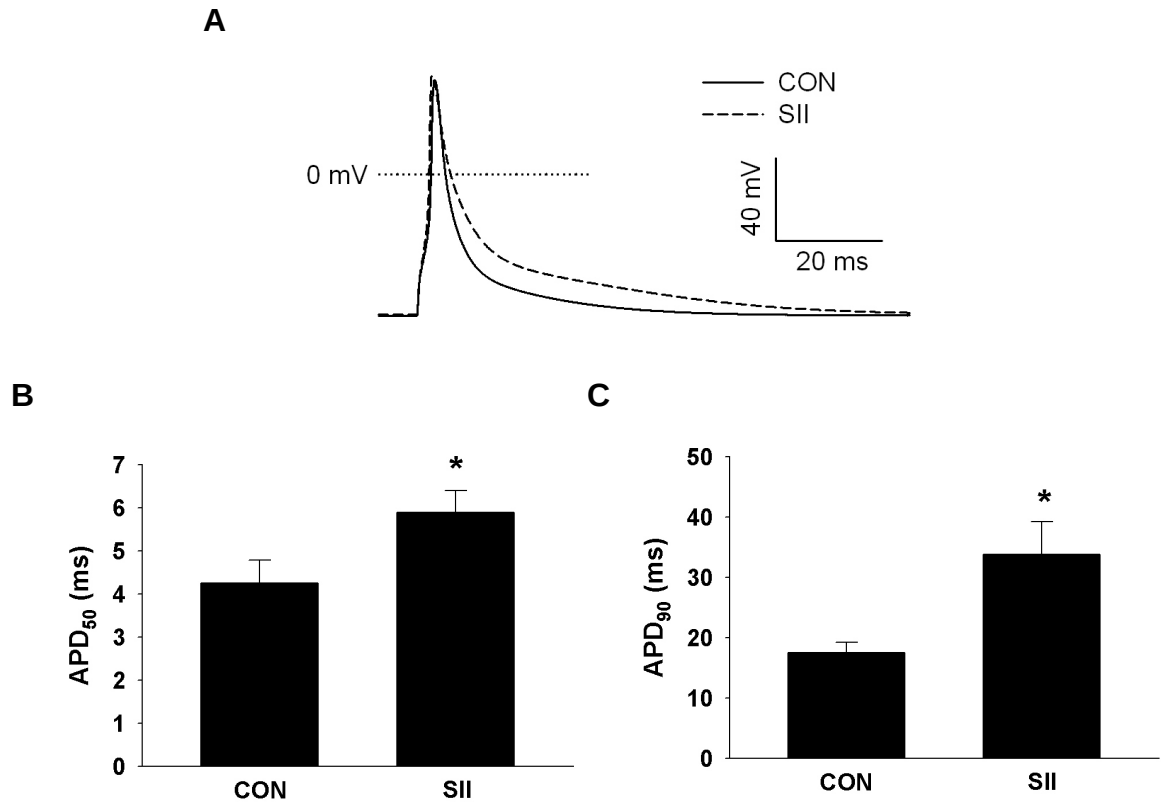

Figure 3.6: G protein independence in AT_1 receptor mediated electrical remodeling. (A) Representative traces of action potential morphology in CON and 5 μM SII incubated LV cells. SII induces action potential prolongation through a G protein independent β-arrestin2 mediated pathway which involves AT_1R internalization. Action potential durations measured from SII treated cells display significant prolongations at both (B) 50% and (C) 90% repolarization to the resting potential. Results suggest that A2 induced electrical remodeling may be mediated via β-arrestin2 dependent signaling and occurs without the involvement of activated G proteins. Statistically significant differences are indicated by * ($p \leq 0.05$).

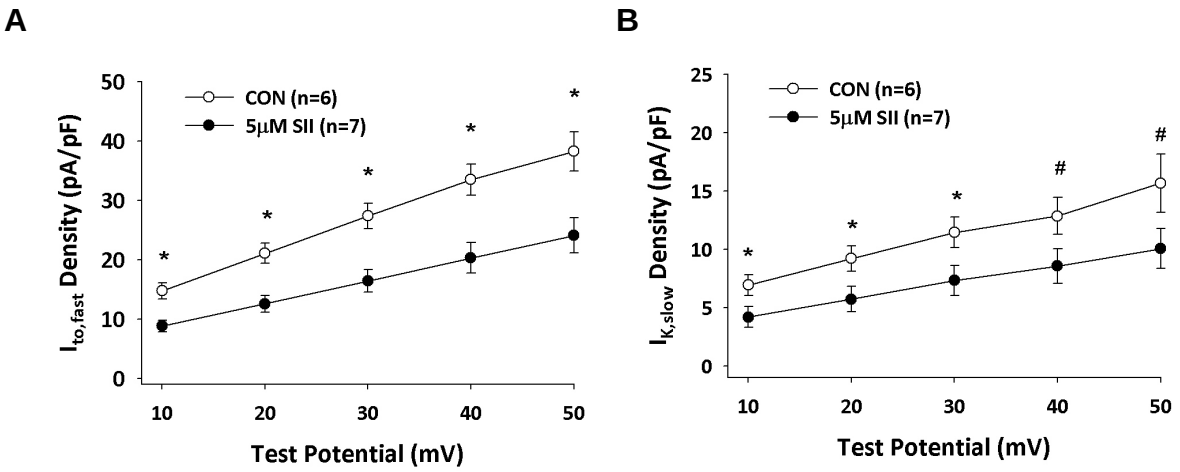

Figure 3.7: G protein independence in AT_1 receptor mediated reductions in (A) $I_{to,fast}$ and (B) $I_{K,slow}$. Significant differences between CON and SII groups are denoted by * ($p \leq 0.05$) and # ($p < 0.10$).

Chapter 4

A Regression Model-Based Analysis of Mouse Left Ventricular Action Potential Repolarization

4.1 Introduction

Since computational models of the cardiac action potential (AP) were first described (McAllister et al. 1975; Beeler and Reuter, 1977), they have often been used to understand the roles and contributions of specific ion channels/pumps/transporters (Greenstein, et al. 2000), mechanisms of electrical propagation (Wang and Rudy, 2000; Cherry and Evans, 2008), and consequences of altered electrophysiological properties in various disease states (Clancy and Rudy, 1999; Clancy and Rudy, 2001). Therefore, AP models have proven their usefulness within the scientific community in a variety of research applications. Since the appearance of the first cardiac models, numerous AP models have been developed (Luo and Rudy, 1991; Noble, et al. 1998; Hund and Rudy, 2004; Pandit, et al. 2003; Bondarenko, et al. 2004) commensurate with an increasing availability of whole-cell patch clamp data from various different species. For this reason, recent models are much more complex—often comprising more than 40 differential equations—in comparison to their older predecessors.

Recently, numerous electrophysiological studies have been conducted on the hearts of mice due to their rapid development and the ability to manipulate their genetic expression. Hence, computational models of a mouse ventricular cell are currently in demand and have been used to simulate AP changes in response to altered ionic concentrations and/or protein expression levels (Pott, et al. 2007; Sabir, et al. 2007), changes in Ca^{2+} handling (Koivumaki, et al. 2009; Mork, et al. 2007) and electrical conduction in both two- (Noujaim, et al. 2007) and three-dimensional tissue (Mori, et al. 2008).

Due to the increasing complexity of electrophysiological models, understanding the relationships between the input parameters and the output variables can be a daunting task, especially if multiple conditions, such as changes in rate, are simulated. To facilitate this

analysis, researchers may benefit from the use of statistical methods that can analyze data in bulk. For instance, Sobie, E.A. (2009) demonstrated the application of multivariable regression for parameter sensitivity analysis, which quantifies the relative contributions of ion channels and pumps/transporters to changes in the AP.

The present study consisted of two main objectives. The first goal was to modify a widely used computational model of the mouse left ventricular AP (Bondarenko, et al. 2004) and to evaluate the modified physiological model against experimental data. The second goal was to analyze the relationships between the physiological model inputs and outputs using multivariable linear regression (MLR), which allowed the determination of which input parameters in the physiological model significantly influence the calculation of the AP. Specifically, we examined the significance of $I_{to,fast}$ and $I_{K,slow}$ conductances and gating properties in setting the repolarization rate at early, mid and late phases of the AP (APD_{50}, APD_{75} and APD_{90}, respectively).

4.2 Materials and Methods

4.2.1 Isolation and Preparation of Left Ventricular Myocytes

A detailed procedure for the isolation of left ventricular cells from wild type mice (7 to 16 weeks old) has been described previously (chapter 3). The isolated myocytes were stored in KB solution at 22°C for up to 12 hours while electrophysiological recordings were being obtained. For each set of experiments, cells were divided into control and experimental groups for comparison. Cells in the experimental groups were treated for 2 to 12 hours with 200 nM or 1 µM of A2 (Sigma-Aldrich Inc.).

4.2.2 Electrophysiological Recordings

Whole-cell patch clamp experiments were conducted at room temperature (22°C) within 12 hours of cell isolation. For both K^+-current and AP measurements, the internal pipette solution contained (in mM) 115 K-Aspartic Acid, 25 KOH, 10 KCl, 3 $MgCl_2$, 11 EGTA, 10 HEPES and 5 Na_2-ATP (pH adjusted to 7.2 with KOH). Pipette series resistances were between 4-7 MΩ in whole-cell mode. For all measurements, myocytes were perfused with an external solution containing (in mM) 137.7 NaCl, 2.3 NaOH, 5.4 KCl, 1 $MgCl_2$, 1.8 $CaCl_2$, 2 $CoCl_2$, 10 Glucose and 5 HEPES (pH adjusted to 7.4 with NaOH).

Both voltage-clamp and current-clamp experiments were conducted using an Axopatch 1D amplifier (Axon Instruments Inc.) interfaced to a computer with a Digidata 1200 digitizer and pClamp 8.2 software (Axon Instruments Inc.). In current-clamp mode, APs were elicited with short depolarizing current injections (~2 ms) at a frequency of 2.5 Hz. In voltage-clamp mode, K^+ currents were measured in response to a short prepulse (10 ms) to -30mV to inactivate Na^+ channels followed by 6000 ms voltage steps (V_{test}) between +10 mV and +50 mV from a holding potential of -65 mV. For all voltage-clamp recordings, series resistances were routinely compensated electronically by ~85%.

4.2.3 Experimental Data Analysis

Voltage- and current-clamp data were analyzed using Clampfit 8.2 (Axon Instruments Inc.), Microsoft Excel (Microsoft Inc.), SigmaPlot (Systat Software Inc.) and MATLAB (Mathworks Inc.). AP durations to 50%, 75% and 90% repolarization (APD_{50}, APD_{75} and APD_{90}, respectively) were accurately determined using a script written in MATLAB. Distinct K^+ current components ($I_{to,fast}$, $I_{K,slow}$ and I_{sus}) were extracted from the obtained K^+ current

recordings using the Curve Fitting Toolbox in MATLAB to fit a two-exponential decay function in the form of $A_1\exp(-t_1/\tau_1)+A_2\exp(-t_2/\ \tau_2)+A_3$ (Xu, H. et al. 1999) as described previously[2]. Peak current amplitudes were normalized to the cell capacitance (C_m), which was measured in each cell using the Membrane Test function in the pClamp software, and presented as current densities (pA/pF).

4.2.4 Validation of a Physiological Model of the Mouse Left Ventricular AP

A mathematical model of a mouse left ventricular AP has been described (Bondarenko et al. 2004) and this formulation was used, with several modifications and simplifications, for the purposes of this study. A fundamental issue with the existing model was discovered upon exploring the effect of diminishing the maximal conductance of $I_{K,slow}$ by 30%, which is a conservative measure of $I_{K,slow}$ downregulation compared with values that have been reported in literature (Brouillette, et al. 2004; Rivard, et al. 2008; Guo, et al. 2000). Incorporating reduced $I_{K,slow}$ conductance into the model yielded APs that failed to repolarize (Fig 4.1) to a physiological range of resting potentials, which is usually more negative than -60 mV in accordance with our experimental data. This presented a problem in applying the model to predict AP characteristics in diseased hearts, which often display significant reductions in $I_{K,slow}$ in addition to $I_{to,fast}$ even though the APs repolarize fully (Rivard, et al. 2008; Guo, et al. 2000). Moreover, the existing model outputs values of the resting potential (more negative than -80 mV) were significantly lower than values (-65 to -70 mV) typically observed in live experiments. To resolve these issues, the existing model was thoroughly examined and the necessary revisions were implemented (Appendix). For the purpose of validation, the revised model was dramatically simplified to simulate whole-cell patch clamp conditions where $[Ca^{2+}]_i$ is buffered

and ion concentrations are held fixed. In addition, Ca^{2+} conductances were virtually eliminated to simulate experimental conditions in which $I_{to,fast}$ and $I_{K,slow}$ are recorded.

To validate the modified computational AP model, which will be referred to as the physiological model, maximal conductances of $I_{to,fast}$ and $I_{K,slow}$ were scaled to match experimental results (Fig 4.2) and simulated APs (generated at 2.5 Hz) were compared with experimental recordings. A2-induced reductions on $I_{to,fast}$ and $I_{K,slow}$ were simulated by attenuating the maximal conductances of $I_{to,fast}$ and $I_{K,slow}$ by 12% and 15%, respectively, for 200 nM A2 and 30% and 35% for 1 μM A2 (percentages obtained from Fig 3.4). Simulated APs with attenuated $I_{to,fast}$ and $I_{K,slow}$ were compared with experimental APs recorded from A2 treated cells (Fig 4.2C & D).

4.2.5 Generation of Training Sets for MLR

To quantify the relative contribution of each input variable to the calculation of the AP, we used a method involving MLR to calculate parameter sensitivities, similar to what has been done using partial least-square (PLS) regression (Sobie, 2009). In the present study, we used conventional multivariable regression since the number of simulation trials far exceeded the number of input variables (explained further in the Discussion). In this instance, PLS regression and MLR produce identical regression coefficients, although PLS regression is more effective in dealing with non-ideal data sets, i.e. when the number of input variables exceeds the number of simulation trials (Sobie, 2009). Since the implementation of MLR is less convoluted than that of PLS regression, MLR was chosen for our analysis.

A summary of the procedure used to obtain parameter sensitivities is outlined in Figure 4.3. Here we will discuss further details underlying the overall scheme. Using the physiological

model, multiple training sets were generated with multiple simulations using randomly generated sets of input values. A training set is defined as the input values and the resulting output values of one simulation trial. Training sets were stored in the input matrix **X** and the output matrix **Y**, where each row of **X** and **Y** represented a particular training set. Therefore, the number of rows, which is always equal in **X** and **Y**, represented the number of training sets obtained for a particular set of simulations. For this study, input variables in matrix **X** were chosen to represent maximal plasma membrane ion channel and pump/transporter densities and shifts in the voltage dependence of relevant ion channels. Each column of **X** represented an input variable and each row represented the set of input values used for one simulation. Each row of **X** was generated by randomly scaling the maximal ionic conductances, pump/transporter fluxes and voltage shifts using a random number generator. Scaling factors for ionic conductances and pump/transporter fluxes were randomly drawn from a log-normal distribution (Fig 4.4), which is a probabilistic assumption that prevents assignment of negative maximal conductance and/or flux values. Voltage shift values were randomly varied with a normal distribution since their range spans both positive and negative values (Fig 4.4). Random numbers were distributed with normalized standard deviations (σ^2) of 0.1. In total, **X** contained 6 ionic conductances, 2 maximal pump/transporter flux parameters and 4 voltage shift parameters for a total of 12 input variables. For the analysis of $I_{to,fast}$ and $I_{K,slow}$ properties, 6 input variables representing $I_{to,fast}$ and $I_{K,slow}$ conductances, activation time constants and inactivation time constants comprised **X**. In most instances, we chose five output variables **Y** to represent AP characteristics comprising APD_{50}, APD_{75}, APD_{90}, V_{rest} and V_{peak}. For the analysis of $I_{to,fast}$ and $I_{K,slow}$ properties, only three output variables, APD_{50}, APD_{75} and APD_{90}, were considered. Each column of **Y** represented an output

variable and each row represented the outputs of one simulation that were calculated using the input values contained in the corresponding row of **X**.

In most cases, 650 training sets were generated corresponding to 650 simulations using randomly generated input variables. Of these, 500 training sets, which was a conservatively large sample size, were used to fit MLR regression coefficients and the remaining 150 training sets were saved for later use in validating the MLR model. As a result, **X** was an *m* by *n* matrix, where *m* is the number of training sets (*m* = 500 in most cases) and *n* is the number of input variables (*n* = 12 or 6) and **Y** was an *m* by *k* matrix, where *k* is the number of output variables (*k* = 5 or 3). Random variables **Y** and some in **X** were log-transformed to resemble normal distributions for the regression analysis.

The physiological model was compiled in C++ and the executable program was incorporated into a MATLAB script to run multiple simulations. APs were simulated at a frequency of 2.5 Hz unless otherwise indicated. Simulated APs were continuously elicited for 50 cycles to attain steady state and only the 50th AP was considered for the values in **Y**.

4.2.6 Calculation of MLR Coefficients for Parameter Sensitivity Analysis

The basic assumption of MLR is that the output variables in **Y** are approximately a linear function of the input variables in **X**, such that for the *i*th training set,

$$y^{(i)} = b_0 + b_1 x_1^{(i)} + b_2 x_2^{(i)} + \cdots + b_n x_n^{(i)} + \varepsilon^{(i)}$$

where b_0 is the intercept term, $\{b_1,\ldots, b_n\}$ are *n* MLR coefficients, $\{x_1, x_2,\ldots, x_n\}$ are *n* input variables, *y* is one of the output variables and ε represents the error, which is the difference between *y* and the MLR prediction of *y*. Given this assumption, the goal of MLR is to produce a set of linear regression coefficients **B** that most closely reproduce **Y** from **X**. In other words, the

MLR model is defined by a matrix of linear regression coefficients **B** that minimizes the sum of squared error between MLR predictions of the outputs $\mathbf{Y}_{\mathbf{predicted}}$ and the physiological model outputs **Y**. **B** can be calculated with the normal equation, which is given by $\mathbf{B} = (\mathbf{X}^T\mathbf{X})^{-1}\mathbf{X}^T\mathbf{Y}$.

However, before **B** was calculated, **X** and **Y** were pre-processed so that **B** may contain informative regression coefficients (parameter sensitivities) that 1) represent the relative contribution of each input variable in the calculation of a particular output variable and 2) indicate the direction (positive or negative) of change in the output variable for a given change in the input variable. For pre-processing, each column of **X** and **Y** was mean-centralized and normalized by its standard deviation for conversion to z-scores, which were stored in $\mathbf{X_Z}$ and $\mathbf{Y_Z}$. Since all of the means are centered, by definition, in z-scores, the intercept term b_0 is automatically assigned a value of zero when MLR coefficients are computed. Hence, the MLR model is described fully (without intercept terms) by the linear summation of weighted input variables in $\mathbf{X_Z}$, where the "weights" are the MLR coefficients. MLR coefficients were computed using the normal equation given by $\mathbf{B} = (\mathbf{X_Z}^T\mathbf{X_Z})^{-1}\mathbf{X_Z}^T\mathbf{Y_Z}$, where **B** is an *n* by *k* matrix of coefficients.

4.2.7 Evaluation of MLR Coefficients

The predictive accuracy of the MLR model has to be good in order to obtain meaningful coefficients that reflect the parameter sensitivities. Therefore, MLR coefficients were assessed on their ability to yield accurate estimates of the output values. As mentioned earlier, of the 650 total training sets obtained from simulations using the physiological model, 150 training sets were set apart to be used in evaluating the predictive accuracy of the MLR coefficients. In effect, these 150 training sets were "held-out" from being used in the determination of MLR

model coefficients for the sole purpose of being used to validate the MLR model. For the purpose of explanation, we will reuse the notations **X** and **Y** to refer to the inputs and outputs, respectively, of the hold-out training set. A summary of the following procedure is outlined in Figure 4.5. Log-transformations were applied to the same input **X** and output **Y** variables that were transformed for computing the MLR coefficients, as described previously. Following this, **X** and **Y** were converted to z-scores to yield $\mathbf{X_Z}$ and $\mathbf{Y_Z}$. The MLR coefficients in **B** were then used to calculate the MLR model predictions $\mathbf{Y_{Z,predicted}}$ with the equation $\mathbf{Y_{Z,predicted}} = \mathbf{X_Z B}$. The predictive accuracy of the MLR model coefficients **B** were evaluated based on the proximity of the linear regression between each output variable in $\mathbf{Y_Z}$ and $\mathbf{Y_{Z,predicted}}$ to the 1:1 line and the proportion of the total variance explained by the regression line (given by R^2). It was imperative for the regression analysis to be carried out with the MLR outputs $\mathbf{Y_{Z,predicted}}$ treated as the independent variable (abscissa) and the physiological model outputs $\mathbf{Y_Z}$ as the dependent variable (ordinate) and not vice versa (Pineiro, et al. 2008).

4.3 Results

4.3.1 Validation of the Mouse Ventricular AP Model

As a precursor to modeling the mouse ventricular AP, whole-cell patch clamp experiments were conducted to measure $I_{to,fast}$, $I_{K,slow}$ and APs from wild type left ventricular myocytes. The voltage dependences of peak $I_{to,fast}$ and $I_{K,slow}$ obtained from experiments are presented in Fig 4.2A. Using the model equations of $I_{to,fast}$ and $I_{K,slow}$, voltage clamp experiments were simulated with the same protocol used in the experiments. Simulated peak $I_{to,fast}$ and $I_{K,slow}$ conductances ($G_{to,fast}$ and $G_{K,slow}$, respectively) were scaled to match the peak currents from the experiments and the resulting voltage dependences from this simulation are given in Fig 4.2B.

From this analysis, mean $G_{to,fast}$ and $G_{K,slow}$ were determined to be 0.32 and 0.10 (mS/µF), respectively. Having confirmed that the simulated peak $I_{to,fast}$ and $I_{K,slow}$ are concordant with experimental data, the scaled conductances $G_{to,fast}$ and $G_{K,slow}$ were implemented in the AP model. In a separate set of simulations, $G_{to,fast}$ and $G_{K,slow}$ were reduced by a percentage amount (Table in Fig 4.2) in accordance with A2 dose-inhibition curves reported in chapter 3 to model $I_{to,fast}$ and $I_{K,slow}$ from cells incubated with 200 nM and 1 µM A2. The simulated traces of APs incorporating $G_{to,fast}$ and $G_{K,slow}$ of control and A2 stimulated cells are displayed in Fig 4.2C. AP characteristics of simulation and experimental traces are tabulated in Table 4.1, in which simulated values of APD (at 50%, 75% and 90% repolarization), V_{rest} and V_{peak} of control cells appear to agree well with experimental values. Additionally, simulated traces of APs with reduced $G_{to,fast}$ and $G_{K,slow}$ to mimic attenuated $I_{to,fast}$ and $I_{K,slow}$ magnitudes in A2 treated cells were similar to APs recorded from cells treated with the same concentrations of A2 (Table 4.1). This suggests that A2-induced reductions in $I_{to,fast}$ and $I_{K,slow}$ explain most of the change observed in the AP morphology of A2 treated cells.

4.3.2 Evaluation of the MLR Coefficients

Scatter plots of the MLR model outputs ($\mathbf{Y_{Z,predicted}}$) versus the corresponding outputs of the physiological model ($\mathbf{Y_Z}$) were constructed and linear regression lines were fit to the data to determine the accuracy of the MLR model coefficients (Fig 4.6). Regression lines fitted for each output variable virtually overlapped the 1:1 line with high R^2 (> 0.90) indicating that MLR model predictions are accurate.

4.3.3 Parameter Sensitivity Analysis

Parameter sensitivities produced from MLR on 12 input and 5 output variables were plotted on bar charts (example in Fig 4.7) to visualize the significance of each input variable on influencing a particular outcome. From this analysis, we were able to hypothesize that the list of input variables having significant contributions to the AP can be reduced to six inputs, which were G_{Na}, G_{Nab}, $G_{to,fast}$, $G_{K,slow,}$ G_{K1} and V_{K1}. Notably, APD_{50} is most influenced by $G_{to,fast}$ and moderately influenced by $G_{K,slow}$ and G_{Na} whereas APD_{90} is most influenced by $G_{K,slow}$ with I_{K1} having a more prominent role than $G_{to,fast}$. Having determined that $I_{to,fast}$ and/or $I_{K,slow}$ are significant contributors to APD_{50}, APD_{75} and APD_{90} based on the parameter sensitivities, we sought to understand whether, in addition to the conductances, time-dependent properties of $I_{to,fast}$ and $I_{K,slow}$ are also significant contributors. Parameter sensitivity analysis (Fig 4.8) with six input variables ($G_{to,fast}$, $G_{K,slow}$, $\tau_{act,fast}$, $\tau_{inact,fast}$, $\tau_{act,slow}$, $\tau_{inact,slow}$) revealed that the inactivation time constants of both $I_{to,fast}$ and $I_{K,slow}$ were of minimal significance in contributing to the AP. To ascertain whether inactivation takes on more significance with increasing stimulation rate, parameter sensitivities were computed with the stimulation frequency increased from 2.5 Hz to 10 Hz. Despite this increase, inactivation time constants remained insignificant in influencing the AP (Fig 4.9A to 4.9C). To demonstrate that inactivation properties are indeed not significant in affecting the AP at a stimulation frequency of 10 Hz, inactivation time constants were either increased by 50% or decreased by 50% in the physiological model and the resulting APs were visualized (Fig 4.9G and 4.9I). These were compared with APs obtained by modulating the activation time constants and the conductances in the same manner (Fig 4.9D to 4.9F and 4.9H). APs obtained by modulating the inactivation time constants were virtually identical to each other whereas modulating the activation time constants or the conductances yielded significant

changes in the morphology of the AP. Therefore, we were able to verify that the parameter sensitivities, with respect to $I_{to,fast}$ and $I_{K,slow}$ properties, were valid.

4.4 Discussion

4.4.1 Evaluation of the Physiological AP Model

A previously published computer model of the mouse left ventricular (Bondarenko, et al. 2004) was modified and simplified to simulate ideal patch-clamp conditions in which it is assumed that ionic concentrations are held fixed. To validate the model with respect to the activity of $I_{to,fast}$ and $I_{K,slow}$, which are known to be the primary repolarizing currents that heavily influence the AP, $I_{Ca,L}$ was set to zero to simulate conditions in which I_{to} currents were experimentally obtained. Additionally, APs, which would later serve to validate the model, were measured in the same external solution in which I_{to} currents were recorded to eliminate the effects of switching to a solution that does not contain $CoCl_2$ (Agus, Z.S. et al. 1991). Though this may seem to be counter-productive, since physiological solutions generally do not contain high concentrations of $CoCl_2$, we decided to take the approach of accurately modeling the AP in the same environment in which I_{to} is measured where we are more certain of I_{to} properties and hence are capable of making a more confident prediction of the AP than if we were to try and model the AP in a solution in which I_{to} is inadequately described. In addition, the exclusion of $I_{Ca,L}$ prevents the need to address the complex interplay of this current with I_{to} currents in shaping the AP (Sah, et al. 2003) and makes validation of the model feasible. A reductionist approach to model evaluation minimizes errors in the model stemming from the uncertainty of how $I_{Ca,L}$ contributes to the repolarization rate in cooperation with $I_{K,slow}$ and $I_{to,fast}$. One goal of this study was to accurately model the mouse ventricular AP, in its simplicity, using direct measurements

from experiments as the standard for model evaluation, as a first step towards complex characterizations that include $I_{Ca,L}$, dynamic ion concentrations and Ca^{2+} dynamics. We verified that our model adequately replicates experimentally obtained AP waveforms based on quantitative comparisons of five output variables that sufficiently describe the AP (Table 4.1). In summary, all of the simulated output variables were within at most one standard deviation of the experimental means.

4.4.2 Simulations of A2-Induced Reductions in $I_{to,fast}$ and $I_{K,slow}$

The validated model was then used to simulate the AP with $G_{to,fast}$ and $G_{K,slow}$ reduced in accordance with peak reductions in $I_{to,fast}$ and $I_{K,slow}$ in response to prolonged (+2 hours) A2 stimulation. For this particular exercise, APs were also directly measured from cells stimulated with 200 nM and 1 µM A2 for comparison with model outputs. All but one simulated parameter (V_{peak}, 1 µM A2) out of ten were within one standard deviation of the experimental means, suggesting that the reductions in $G_{to,fast}$ and $G_{K,slow}$ can explain most of the changes in AP morphology in response to A2 stimulation, given our experimental conditions. However, from this analysis, it was not possible to deduce whether or not A2 significantly regulates other components that have relatively little influence on the AP (i.e. Na/K pump current).

4.4.3 Prediction Accuracy of the MLR Model

The dominant influence of $I_{to,fast}$ and $I_{K,slow}$ on the AP morphology is a well-known murine trait (Brunner, et al. 2001) however, the relative contribution of each component to the AP has not been quantitatively defined. Therefore, the second goal of this study was to quantify the impact of $I_{to,fast}$ and $I_{K,slow}$ properties on the morphology of the AP using parameter

sensitivities obtained from MLR. Before this analysis was carried out, we assessed the predictive accuracy of the MLR model to ensure that the regression coefficients accurately represented parameter sensitivities. Our evaluation indicated that the MLR model reproduced physiological model outputs, with the range of input values that were considered in our analysis. Given that all of the conditions (i.e. normality of input variable frequency distributions, linearly independent input variables, large number of training sets) were ideal for least-squares linear regression, a calculation of informative parameter sensitivities was to be expected. In situations where all of these conditions cannot be met (i.e. smaller number of training sets than the number of input variables), other methods such as PLS regression are more useful (Sobie, 2009).

For this particular study, the effectiveness of the MLR model in accurately predicting outputs of a non-linear system (physiological model) undoubtedly benefited from the log-transformations of both input and output variables, which allowed MLR to be performed on transformed variables with (approximately) normal distributions. Therefore, in situations where log-transformations will not suffice, MLR models may benefit from using other transformation functions (i.e. square root) that result in the closest resemblance to a normal distribution.

4.4.4 Significance of $I_{to,fast}$ and $I_{K,slow}$ Properties

Based on the parameter sensitivities (Table 4.2), it appears that $I_{to,fast}$ heavily influences the early repolarization rate, reflected in the APD_{50}, without much influence on late phase repolarization (APD_{90}) while $I_{K,slow}$ influences both early and late phases consistently. This result is not surprising based on experimental observations (Brouillette, et al. 2004) that $I_{K,slow}$ possesses slow inactivation kinetics (τ_{inact} > 1000 ms) that are dramatically different from those of $I_{to,fast}$ (τ_{inact} < 100 ms). From a theoretical standpoint, this means that inactivation of $I_{K,slow}$

plays an insignificant part within physiological durations of the AP, which is on the order of tens of milliseconds. Therefore, the contribution of $I_{K,slow}$ in shaping the AP mostly depends on its activation properties and maximal conductance. This was verified using MLR parameter sensitivity analysis on six input variables representing the inactivation and activation time constants of $I_{to,fast}$ and $I_{K,slow}$ (Fig 4.8). Surprisingly, based on this analysis, changes in $I_{to,fast}$ inactivation were also insignificant in influencing the AP morphology despite its shorter time constants. To test whether $I_{to,fast}$ and $I_{K,slow}$ inactivation properties were significant with faster AP rate, parameter sensitivities were calculated with the stimulation frequency increased to 10 Hz (Fig 4.9). Even under these conditions, inactivation appeared to be a negligible component in shaping AP morphology. The insignificance of $I_{to,fast}$ inactivation properties to the APD in murine left ventricular myocytes suggests an important difference between the underlying electrophysiological properties of mice and larger species, in which the longer APD nearly guarantees that I_{to} inactivation properties are an integral part of shaping the AP. Furthermore, the observation that $I_{to,fast}$ is not significantly involved in APD_{90} suggests that the primary function of $I_{to,fast}$ is in the determination of the early repolarization rate and hence, exists to regulate $I_{Ca,L}$. In contrast, $I_{K,slow}$ appears to be a more crucial component of AP repolarization since it regulates the AP considerably in virtually all phases of repolarization.

Another interesting observation in our study was that increasing the activation time constants of $I_{to,fast}$ and $I_{K,slow}$ prolong APD_{50} but does the opposite with APD_{90}. The difference here is possibly because APD_{50} is influenced mainly by the upstrokes of $I_{to,fast}$ and $I_{K,slow}$ whereas APD_{90} depends upon how slowly $I_{to,fast}$ and $I_{K,slow}$ decay during the AP. Since inactivation is not involved, the decay depends solely on the rate of activation "gates" closing in response to membrane repolarization. Moreover, our results suggest that activation and inactivation

properties have minimal influence on APD_{75}, which probably reflects the time point at which the two currents are mostly affected by the membrane potential (and therefore, the conductance) rather than time-dependent gating properties.

4.4.5 Interpretation of Parameter Sensitivities

Parameter sensitivities quantify the relative change in the output that is the result of a one standard deviation increase in the relevant input. Based on this definition, if a particular input variable were to be more widely distributed with higher standard deviation, the corresponding parameter sensitivity would be greater. For the purpose of our study, the mean-normalized standard deviations of ionic conductances and maximal transporter fluxes (k_{NaCa} and I_{NaKmax}) were equal since the random number scaling factors were drawn consistently from a log-normal distribution with a median of 1 and a standard deviation of 0.1. If parameter sensitivities were to be calculated using experimental data, in which normalized variances among various input parameters are likely to vary, interpretation of parameter sensitivities should account for the variances of individual input parameters.

4.4.6 Conclusions

In this study, we demonstrated the use of a linear regression model to quantify the relative importance of individual electrophysiological parameters on determining the morphology of the mouse left ventricular AP. Specifically, we analyzed MLR parameter sensitivities to distinguish the roles of different $I_{to,fast}$ and $I_{K,slow}$ properties in influencing the AP. Future work should involve the precise incorporation of $I_{Ca,L}$, dynamic ion concentrations and

Ca^{2+} handling machinery to the physiological model and work towards understanding the complexity of the cardiac cell using regression model-based analysis.

	APD_{50} (ms)	APD_{75} (ms)	APD_{90} (ms)	V_{rest} (mV)	V_{max} (mV)
CON					
Experiment (n=6)	4.1 ± 0.6	10.3 ± 1.6	24.4 ± 4.3	-66.0 ± 1.3	51.8 ± 4.6
Simulation	4.1	9.0	25.6	-67.3	50.8
200 nM A2					
Experiment (n=6)	4.4 ± 0.9	12.1 ± 3.3	27.9 ± 9.4	-67.2 ± 1.3	54.1 ± 7.1
Simulation	4.4	10.3	29.3	-67.3	51.1
1 mM A2					
Experiment (n=5)	5.2 ± 1.2	13.8 ± 3.2	33.4 ± 12.3	-66.2 ± 2.0	54.2 ± 2.5
Simulation	4.9	12.5	36.4	-67.3	51.5

Table 4.1: AP properties measured from patch clamp experiments and model simulations. The control (CON) values of APD, V_{rest} and V_{max} from experiments and simulation demonstrated that a simulated AP using the computer model is well in agreement with experimentally obtained traces of the AP from control myocytes. Simulating A2-induced changes in $I_{to,fast}$ and $I_{K,slow}$ produced APs that minimally deviated from experimental measurements.

B	APD_{50}	APD_{75}	APD_{90}	V_{rest}	V_{peak}
G_{Na}	**-0.3741**	**-0.3593**	-0.1427	0.0057	**0.5989**
k_{NaCa}	0.0038	-0.0014	-0.0084	0.0011	-0.0067
I_{NaKmax}	-0.0409	0.0282	-0.1090	-0.1868	0.1313
G_{Nab}	0.0899	-0.1439	0.2150	**0.6335**	**-0.4769**
$G_{to,fast}$	**-0.7646**	**-0.6147**	-0.1931	0.0013	-0.0154
$G_{K,slow}$	**-0.4500**	**-0.5891**	**-0.5683**	0.0015	-0.0799
$G_{K,ss}$	-0.0409	-0.1126	-0.2768	-0.0008	-0.0108
G_{K1}	-0.0817	0.1446	**-0.5324**	**-0.6474**	**0.4914**
$V_{to,fast}$	-0.0906	-0.1180	-0.0621	0.0048	-0.0179
$V_{K,slow}$	-0.0211	-0.0523	-0.1463	-0.0046	0.0029
V_{K1}	-0.0141	0.1667	**0.3548**	**-0.3156**	0.2164
$V_{K,ss}$	-0.0193	-0.0206	-0.0468	0.0022	0.0080

Table 4.2: Multivariable regression parameter sensitivities contained in **B** indicate relative contributions of each input variable (leftmost column) on influencing the 5 output variables (APD_{50}, APD_{75}, APD_{90}, V_{rest} and V_{peak}) that were considered for this study. The top three input variables that significantly influence a particular outcome contain values in their respective rows that are highlighted in bold.

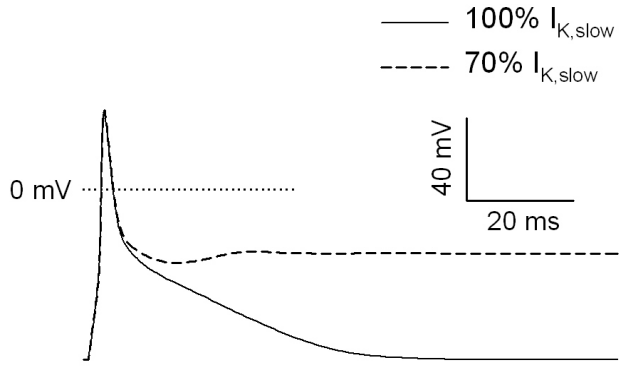

Figure 4.1: Simulated traces of the Bondarenko model AP in control (100% $I_{K,slow}$) and 30% $I_{K,slow}$ reduced (70% of control $I_{K,slow}$ conductance retained) myocytes. According to the Bondarenko model outputs, 30% reduction in $I_{K,slow}$ results in repolarization failure. This was a significantly different result compared with AP traces obtained from cells incubated with 5 µM A2 (pink trace in Fig 3.1), which possess $I_{to,fast}$ and $I_{K,slow}$ that are approximately 40% and 45% reduced, respectively, relative to CON (based on Fig 3.4). Based on these comparisons, the Bondarenko model inadequately describes the electrophysiological activity underlying the AP. Therefore, we modified the model equations in accordance with experimental observations to improve the model output (Appendix).

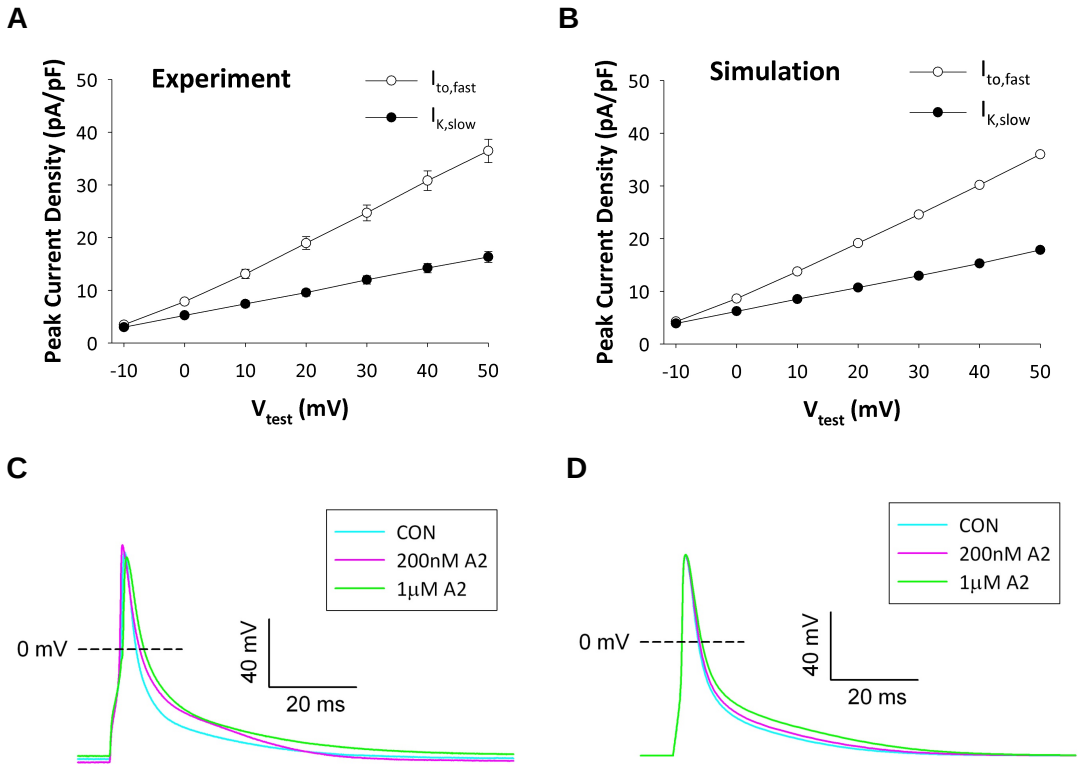

Simulation Parameters		
	$\Delta gmax_{to,f}$	$\Delta gmax_{K,slow}$
200nM A2	-12%	-15%
1mM A2	-30%	-35%

Figure 4.2: Evaluation of the physiological mouse AP model. Peak conductances of $I_{to,fast}$ and $I_{K,slow}$ used for the computation of the AP were scaled to match our experimental observations. In doing so, the peak I-V relationships obtained from experiments (A) were in agreement with the simulations (B). (C) Representative traces of APs that were obtained experimentally from control (CON), 200 nM A2 and 1 μM A2 groups. (D) Simulations of the AP using the modified model with varying $I_{to,fast}$ and $I_{K,slow}$ conductance parameters based on experimentally observed cellular changes in peak $I_{to,fast}$ and peak $I_{K,slow}$ in the presence of different concentrations of A2 (shown in the table). Based on the AP measurements (Table 4.1), the simulated APs agreed well with experimental APs.

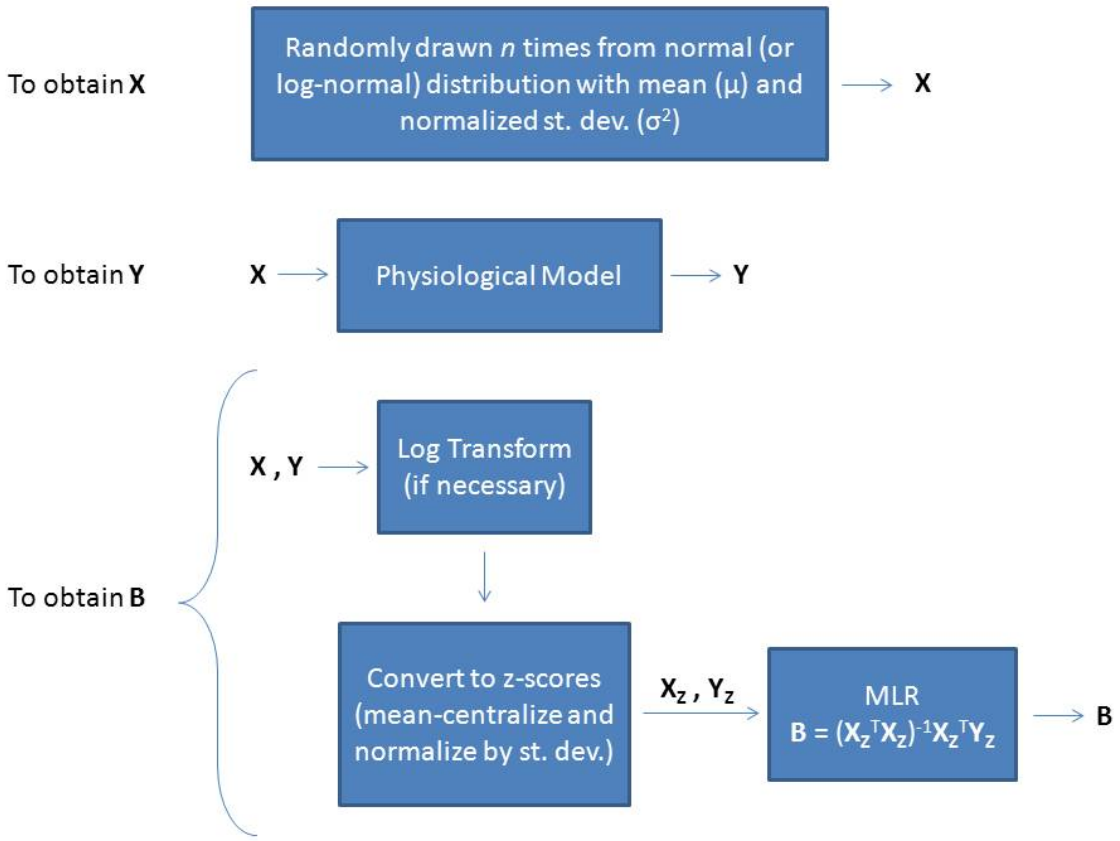

Figure 4.3: Overview of the procedure taken to calculate parameter sensitivities **B** from matrices **X** and **Y**. Each column of matrix **X** represents an input parameter (i.e. $G_{to,fast}$) and each column of **Y** represents an output variable (i.e. APD_{50}), which were calculated from the physiological model. The rows of **X** and **Y** represent the number of randomly drawn samples *n*. The mean (μ) of each input parameter is the value of the parameter in control conditions. To obtain parameter sensitivities **B**, some input parameters in **X** and some output variables in **Y** were log-transformed so that the frequency distributions of all variables in both **X** and **Y** resembled normal distributions, which is one of the conditions that need to be fulfilled for least-square regression. Although the regression may proceed without conversion to z-scores for MLR-based prediction of **Y**, meaningful values of **B** that represent relative contributions of each input variable to the calculation of the outputs can only be obtained when all of the input and output variables have been mean-centralized and normalized by their respective standard deviations.

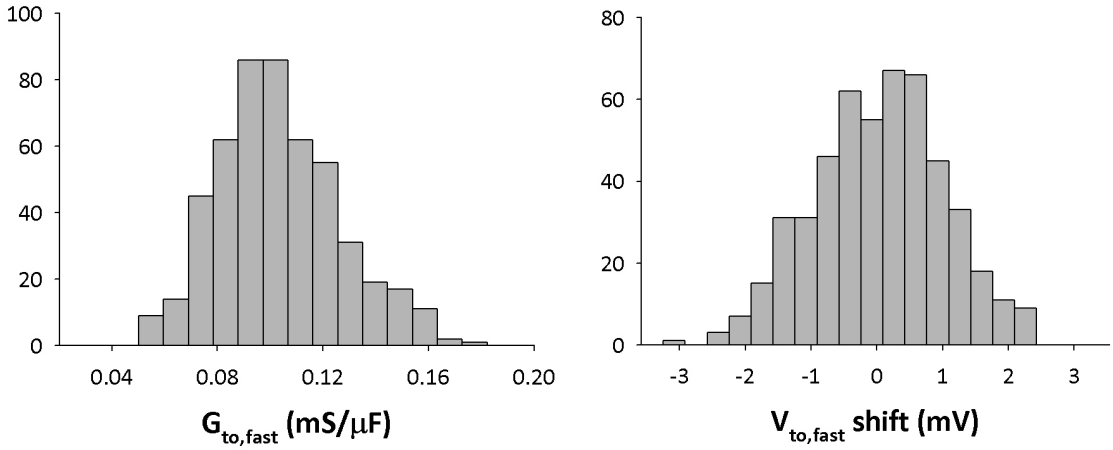

Figure 4.4: Representative examples depicting the frequency distributions (n = 500 samples) of two input variables, for which the distribution of $G_{to,fast}$ is log-normal (left) and that of $V_{to,fast}$ is normal (right). Log-normal distributions were used for certain variables (i.e. conductances) which physically cannot have negative values.

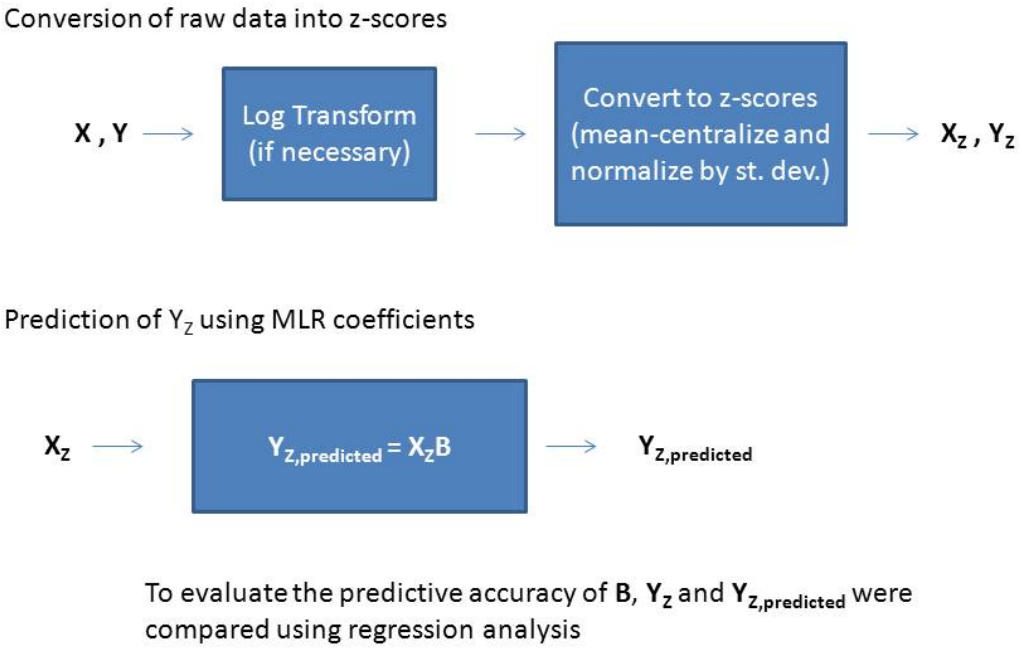

Figure 4.5: Overview of the procedure to evaluate the predictive accuracy of the MLR coefficients contained in **B**. Hold-out training sets (training sets not used for the determination of MLR coefficients) in **X** and **Y** were converted to z-scores $\mathbf{X_Z}$ and $\mathbf{Y_Z}$ and MLR model predictions $\mathbf{Y_{Z,predicted}}$ were calculated with the equation $\mathbf{Y_{Z,predicted}} = \mathbf{X_Z B}$. To evaluate the predictive accuracy of **B**, the relationship between $\mathbf{Y_Z}$ and $\mathbf{Y_{Z,predicted}}$ was assessed using regression analysis.

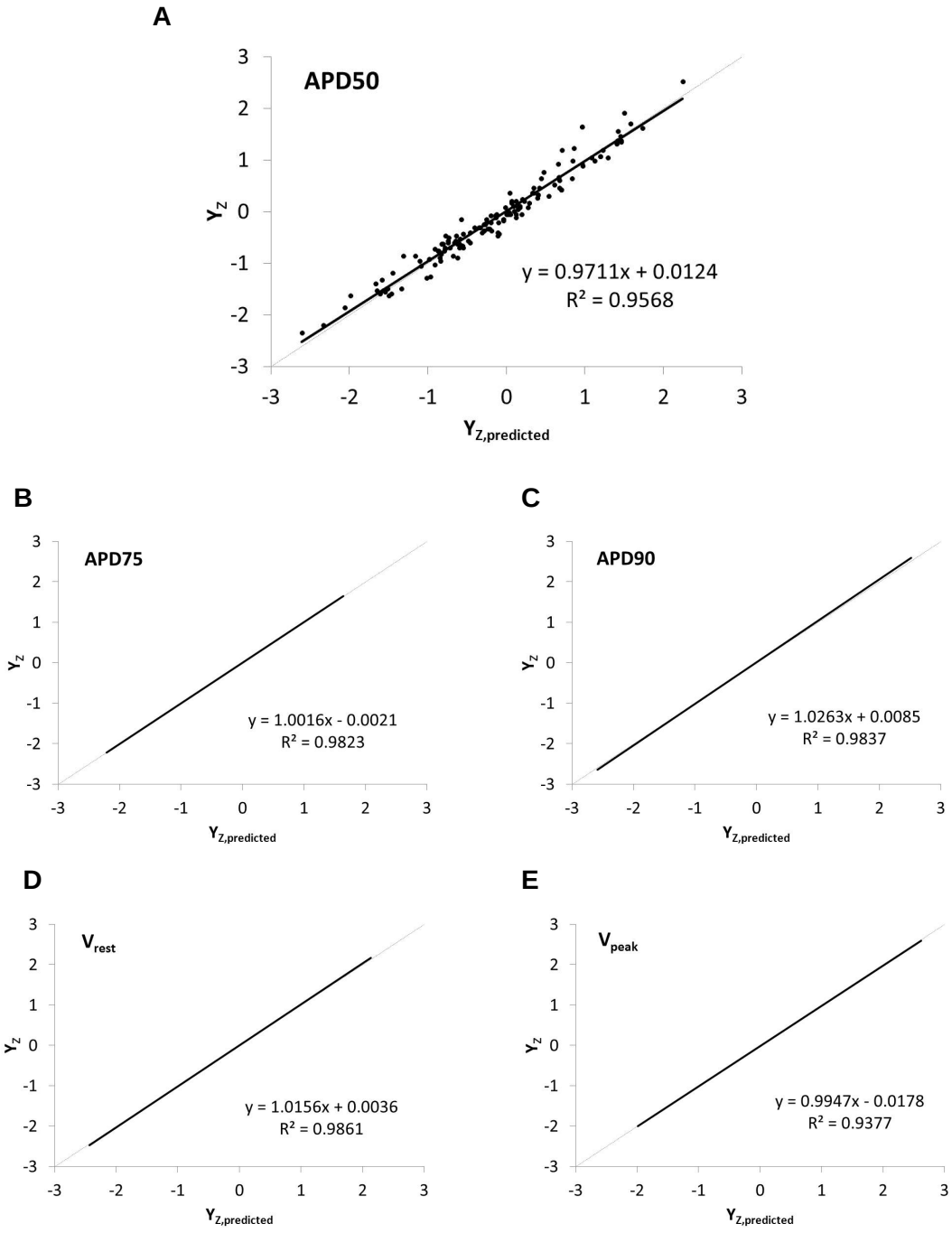

Figure 4.6: Evaluating the predictive accuracy of the MLR model coefficients. (A) Representative scatter plot of APD_{50} z-scores obtained with the MLR model ($\mathbf{Y_{Z,predicted}}$) vs. z-scores obtained with the physiological model ($\mathbf{Y_Z}$). The gray line represents the 1:1 line which has slope = 1 and zero intercept. The solid line is the regression line, which virtually overlaps the 1:1 line with high R^2 indicating good predictability of the MLR model. Regression analysis of (B) APD_{75}, (C) APD_{90}, (D) V_{rest} and (E) V_{peak} are shown without the actual data points for clarity.

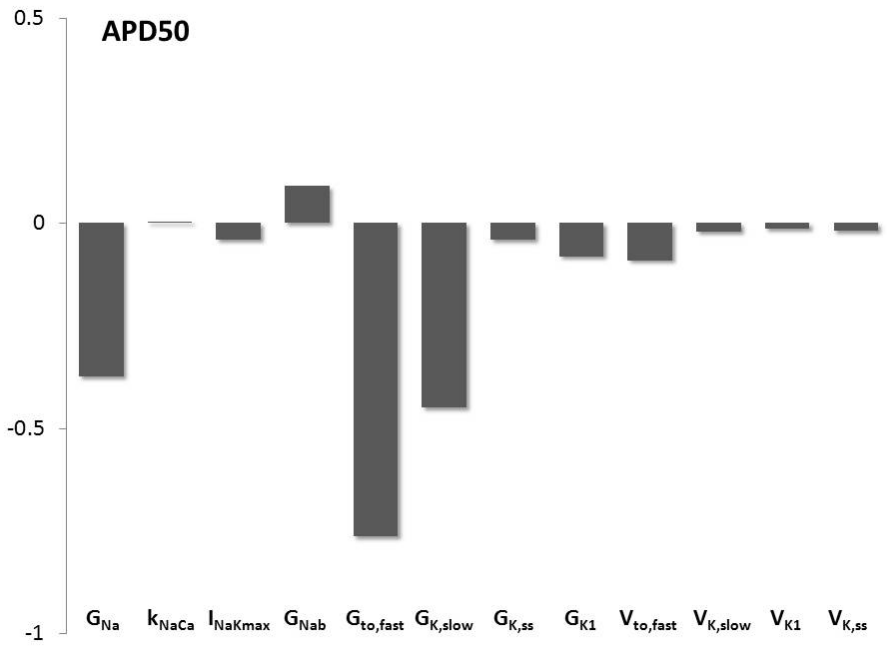

Figure 4.7: Parameter sensitivity analysis of input variables on affecting APD_{50}. This is a representative bar chart of normalized MLR coefficients, which are indicative of the relative contributions of each input variable to each output variable. From this chart, it can be easily determined that out of the 12 input variables examined, $G_{to,fast}$ most heavily contributes to APD_{50}.

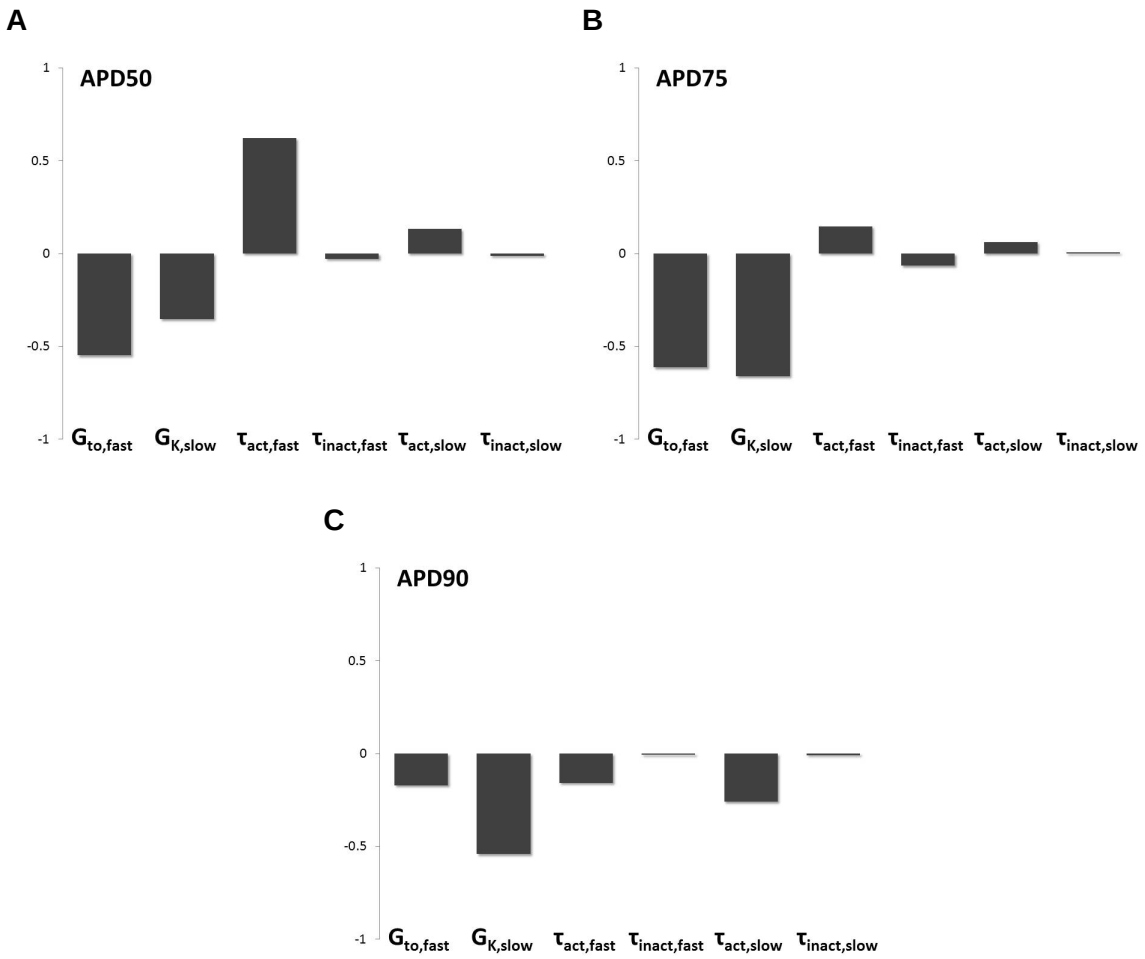

Figure 4.8: Parameter sensitivities of $I_{to,fast}$ and $I_{K,slow}$ properties consisting of conductances ($G_{to,fast}$ and $G_{K,slow}$), activation time constants of $I_{to,fast}$ and $I_{K,slow}$ ($\tau_{act,fast}$ and $\tau_{act,slow}$, respectively) and inactivation time constants ($\tau_{inact,fast}$ and $\tau_{inact,slow}$). Inactivation time constants of both currents are not significant in shaping the AP. For these results, AP stimulation frequency was set at 2.5 Hz.

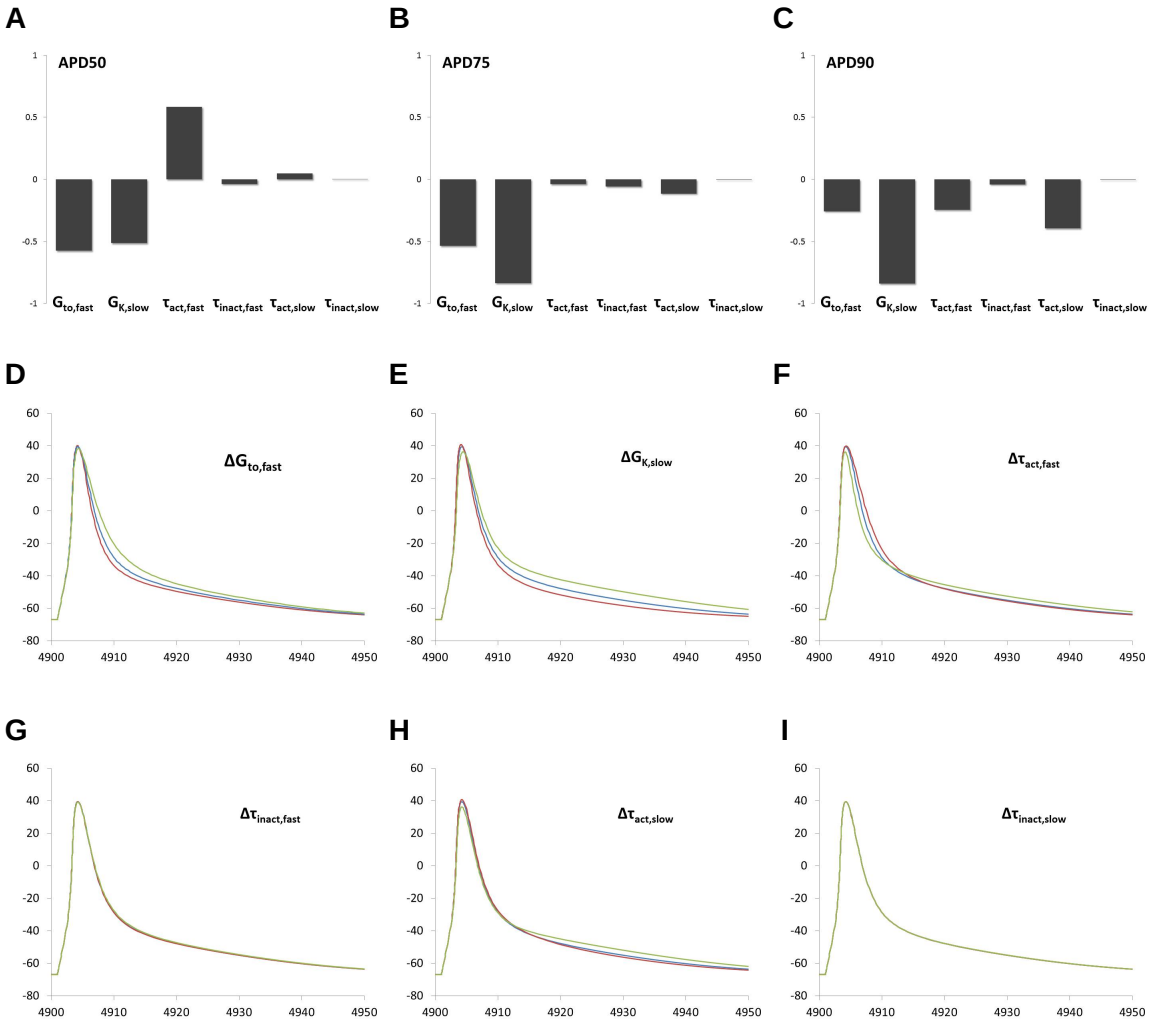

Figure 4.9: (A to C) Parameter sensitivities of $I_{to,fast}$ and $I_{K,slow}$ properties obtained at high AP stimulation rate (10 Hz). To verify these parameter sensitivities, input variables were individually modulated (by increasing or decreasing by 50%) and the resulting APs were examined to determine whether or not a significant change had occurred (D to I). In accordance with the parameter sensitivities, inactivation of either $I_{to,fast}$ or $I_{K,slow}$ (G and I) was not significant in contributing to the AP morphology. AP traces resulting from no change, 50% increase and 50% decrease of the relevant input variable are represented by blue, red and green lines, respectively. The vertical axes represent membrane potential (mV) and the horizontal axes represent time (ms).

Chapter 5

General Discussion

This chapter summarizes and discusses the major findings of this thesis. The overall goal of this research was to investigate AT_1 receptor involvement in the transduction of mechanical stress into molecular signals, which induce significant changes to the electrophysiology of cardiac myocytes. Our secondary objective was to use a computational model-based approach to understand the role and significance of individual ion channel properties in affecting the AP profile. In fulfilling these objectives, we introduced several new aspects of cardiac cell regulation and function that, we believe, will greatly impact future studies on this particular subject.

5.1 AT_1 Receptor-Mediated Electrical Remodeling in Left Ventricular Myocytes

The first aim of this research was to determine the role of AT_1 receptors in mediating pressure overload-induced electrical remodeling in mouse left ventricular myocytes. A preliminary observation was the immediate (within 48 hours) downregulation of $I_{to,fast}$ and $I_{K,slow}$ in response to sustained increases in mechanical stress brought upon by aortic constriction. These changes were observed prior to any structural remodeling suggesting that electrical remodeling, involving reductions in $I_{to,fast}$ and $I_{K,slow}$, precedes the development of cardiac hypertrophy in response to increased mechanical load. In isolated myocytes, reductions in $I_{to,fast}$ and $I_{K,slow}$, resulting from short-term TAC surgery, were reversible using an AT_1 receptor blocker, indicating that pressure overload-induced reductions in $I_{to,fast}$ and $I_{K,slow}$ may be attributable to AT_1 receptor activation. From the observation that these reductions were retained in isolated myocytes, which are no longer subjected to mechanical strain, we hypothesized that AT_1 receptor stimulation is sustained in these myocytes possibly via an autocrine mechanism of A2 release (Sadoshima, et al. 1993) contained within the t-tubules. In long-term TAC myocytes,

$I_{to,fast}$ was reduced and AT_1 receptor blockade restored $I_{to,fast}$, but unlike short-term TAC myocytes, $I_{K,slow}$ was only moderately reduced and minimally changed in response to AT_1 receptor blockade. The reasons for this is yet unclear, but it may involve increased surface expression levels of Kv1.5 and Kv2.1 (Marionneau, et al. 2008), both of which encode $I_{K,slow}$, in long-term TAC myocytes.

5.2 G Protein-Independence in AT_1 Receptor-Mediated Electrical Remodeling

To further explore the mechanisms of AT_1 receptor-mediated electrical remodeling in cardiac myocytes, we incubated isolated control left ventricular myocytes with various concentrations of external A2. Preliminary observations of APs, which reflect the global activity of all membrane ionic currents, recorded from these cells displayed A2 dose-dependence in both APD_{50} and APD_{90}, suggesting a strong relationship between A2 and either or both of the predominant repolarizing currents $I_{to,fast}$ and $I_{K,slow}$. Therefore, the effects of various A2 concentrations on these individual currents were examined, from which it was observed that A2 inhibits both $I_{to,fast}$ and $I_{K,slow}$ in a dose-dependent manner without shifting their voltage-dependence. This suggests that A2 regulation of $I_{to,fast}$ and $I_{K,slow}$ primarily involves modulations in the number of functional $I_{to,fast}$ and $I_{K,slow}$ channels expressed in the membrane. Moreover, based on their dose-inhibition curves, $I_{to,fast}$ and $I_{K,slow}$ half-max concentrations were virtually the same, suggesting that A2 may regulate $I_{to,fast}$ and $I_{K,slow}$ in a coherent manner. Based on a previous study, which suggests AT_1 receptors co-internalize with Kv4.3 (Doronin, et al. 2004), we hypothesized that $I_{to,fast}$ and $I_{K,slow}$ are not dependent on G protein stimulation, which is independent of β-arrestin dependent AT_1 receptor internalization. The first set of experiments involved application of colchicine to the isolated myocytes to disrupt intracellular trafficking. In

these cells, APDs were unchanged in response to application of A2, suggesting that either inhibition of AT_1 receptor internalization or the inhibition of $I_{to,fast}/I_{K,slow}$ trafficking (or perhaps both, if AT_1 receptor and channels are co-internalized) resulted in the desensitization of $I_{to,fast}$ and $I_{K,slow}$ to A2 stimulation. Hence, this experiment alone could not rule out G protein-dependence of AT_1 receptor-mediated $I_{to,fast}$ and $I_{K,slow}$ reductions. Therefore, we utilized a recently developed pharmacological approach to selectively activate the AT_1 receptor without stimulating G proteins to test for the involvement of G proteins in AT_1 receptor-induced reductions of $I_{to,fast}$ and $I_{K,slow}$. Even without G protein involvement, $I_{to,fast}$ and $I_{K,slow}$ were significantly reduced in response to AT_1 receptor stimulation, suggesting that $I_{to,fast}$ and $I_{K,slow}$ reductions mediated by AT_1 receptors are G protein independent and may depend on co-internalization with the receptors.

5.3 Regression Model-Based Analysis of Electrophysiological Parameters

The third and final aim of this research was to use a combined approach involving a physiological model of the mouse AP and multivariable linear regression (MLR) to quantify the significance of various electrophysiological parameters in contributing to the AP morphology. Based on our analysis of the MLR parameter sensitivities, APDs were highly sensitive to changes in $I_{to,fast}$ and/or $I_{K,slow}$ conductances relative to other electrophysiological parameters. However, we determined that APDs were insensitive to changes in $I_{to,fast}$ and $I_{K,slow}$ time constants of inactivation at both slow (2.5 Hz) and fast (10 Hz) AP rates. Therefore, we hypothesized that in mouse left ventricular myocytes, inactivation properties of $I_{to,fast}$ and $I_{K,slow}$ have minimal influence on the AP morphology unlike their respective conductances and activation properties, which appear to be significantly involved in some aspect of the AP.

5.4 Conclusions

Mechanisms underlying the regulation and function of cardiac myocytes involve a diverse array of processes, of which, we have studied only a small subset. First, our findings suggest the importance of revealing the time dependence, especially at early time points, of changes that occur in cardiac myocytes in response to pressure overload. Second, as a continuation of our study, future work should investigate the electrophysiological consequences of biased AT_1 receptor signaling, which may potentially lead to the development of well-targeted pharmacological therapy. Lastly, we stress the importance of developing and finding new ways of utilizing mathematical cardiac cell models, which will find more use in the future as our knowledge base continues to grow.

REFERENCES

1. Adams JW, Sakata Y, Davis MG, Sah VP, Wang Y, Liggett SB, Chien KR, Brown JH, Dorn GW, 2nd. Enhanced galphaq signaling: A common pathway mediates cardiac hypertrophy and apoptotic heart failure. *Proc Natl Acad Sci U S A*. 1998;95:10140-10145

2. Agus ZS, Dukes ID, Morad M. Divalent cations modulate the transient outward current in rat ventricular myocytes. *Am J Physiol*. 1991;261:C310-318

3. Aiello EA, Cingolani HE. Angiotensin ii stimulates cardiac l-type ca(2+) current by a ca(2+)- and protein kinase c-dependent mechanism. *Am J Physiol Heart Circ Physiol*. 2001;280:H1528-1536

4. Aplin M, Bonde MM, Hansen JL. Molecular determinants of angiotensin ii type 1 receptor functional selectivity. *J Mol Cell Cardiol*. 2009;46:15-24

5. Aplin M, Christensen GL, Schneider M, Heydorn A, Gammeltoft S, Kjolbye AL, Sheikh SP, Hansen JL. Differential extracellular signal-regulated kinases 1 and 2 activation by the angiotensin type 1 receptor supports distinct phenotypes of cardiac myocytes. *Basic Clin Pharmacol Toxicol*. 2007;100:296-301

6. Armoundas AA, Hobai IA, Tomaselli GF, Winslow RL, O'Rourke B. Role of sodium-calcium exchanger in modulating the action potential of ventricular myocytes from normal and failing hearts. *Circ Res*. 2003;93:46-53

7. Baker KM, Aceto JF. Angiotensin ii stimulation of protein synthesis and cell growth in chick heart cells. *Am J Physiol*. 1990;259:H610-618

8. Barry SP, Davidson SM, Townsend PA. Molecular regulation of cardiac hypertrophy. *Int J Biochem Cell Biol*. 2008;40:2023-2039

9. Beeler GW, Reuter H. Reconstruction of the action potential of ventricular myocardial fibres. *J Physiol*. 1977;268:177-210

10. Benitah JP, Gomez AM, Bailly P, Da Ponte JP, Berson G, Delgado C, Lorente P. Heterogeneity of the early outward current in ventricular cells isolated from normal and hypertrophied rat hearts. *J Physiol*. 1993;469:111-138

11. Bers DM. Cardiac excitation-contraction coupling. *Nature*. 2002;415:198-205

12. Beuckelmann DJ, Nabauer M, Erdmann E. Alterations of k+ currents in isolated human ventricular myocytes from patients with terminal heart failure. *Circ Res*. 1993;73:379-385

13. Bondarenko VE, Szigeti GP, Bett GC, Kim SJ, Rasmusson RL. Computer model of action potential of mouse ventricular myocytes. *Am J Physiol Heart Circ Physiol*. 2004;287:H1378-1403

14. Bouchard RA, Clark RB, Giles WR. Effects of action potential duration on excitation-contraction coupling in rat ventricular myocytes. Action potential voltage-clamp measurements. *Circ Res*. 1995;76:790-801

15. Brouillette J, Clark RB, Giles WR, Fiset C. Functional properties of k+ currents in adult mouse ventricular myocytes. *J Physiol*. 2004;559:777-798

16. Brown VI, Greene MI. Molecular and cellular mechanisms of receptor-mediated endocytosis. *DNA Cell Biol*. 1991;10:399-409

17. Brunet S, Aimond F, Li H, Guo W, Eldstrom J, Fedida D, Yamada KA, Nerbonne JM. Heterogeneous expression of repolarizing, voltage-gated k+ currents in adult mouse ventricles. *J Physiol*. 2004;559:103-120

18. Brunner M, Guo W, Mitchell GF, Buckett PD, Nerbonne JM, Koren G. Characterization of mice with a combined suppression of i(to) and i(k,slow). *Am J Physiol Heart Circ Physiol*. 2001;281:H1201-1209

19. Campbell DL, Rasmusson RL, Qu Y, Strauss HC. The calcium-independent transient outward potassium current in isolated ferret right ventricular myocytes. I. Basic characterization and kinetic analysis. *J Gen Physiol*. 1993;101:571-601

20. Cherry EM, Evans SJ. Properties of two human atrial cell models in tissue: Restitution, memory, propagation, and reentry. *J Theor Biol*. 2008;254:674-690

21. Clancy CE, Rudy Y. Linking a genetic defect to its cellular phenotype in a cardiac arrhythmia. *Nature*. 1999;400:566-569

22. Clancy CE, Rudy Y. Cellular consequences of herg mutations in the long qt syndrome: Precursors to sudden cardiac death. *Cardiovasc Res*. 2001;50:301-313

23. Cutler MJ, Jeyaraj D, Rosenbaum DS. Cardiac electrical remodeling in health and disease. *Trends Pharmacol Sci*. 2011;32:174-180

24. D'Angelo DD, Sakata Y, Lorenz JN, Boivin GP, Walsh RA, Liggett SB, Dorn GW, 2nd. Transgenic galphaq overexpression induces cardiac contractile failure in mice. *Proc Natl Acad Sci U S A*. 1997;94:8121-8126

25. Deckmann AC, Theizen TH, Medrano FJ, Franchini KG, Pereira GA. Immediate response of myocardium to pressure overload includes transient regulation of genes associated with mitochondrial bioenergetics and calcium availability. *Genet Mol Biol*. 2010;33:12-16

26. Dixon JE, Shi W, Wang HS, McDonald C, Yu H, Wymore RS, Cohen IS, McKinnon D. Role of the kv4.3 k+ channel in ventricular muscle. A molecular correlate for the transient outward current. *Circ Res*. 1996;79:659-668
27. Doronin SV, Potapova IA, Lu Z, Cohen IS. Angiotensin receptor type 1 forms a complex with the transient outward potassium channel kv4.3 and regulates its gating properties and intracellular localization. *J Biol Chem*. 2004;279:48231-48237
28. Dostal DE, Rothblum KN, Conrad KM, Cooper GR, Baker KM. Detection of angiotensin i and ii in cultured rat cardiac myocytes and fibroblasts. *Am J Physiol*. 1992;263:C851-863
29. England SK, Uebele VN, Shear H, Kodali J, Bennett PB, Tamkun MM. Characterization of a voltage-gated k+ channel beta subunit expressed in human heart. *Proc Natl Acad Sci U S A*. 1995;92:6309-6313
30. Fedida D, Eldstrom J, Hesketh JC, Lamorgese M, Castel L, Steele DF, Van Wagoner DR. Kv1.5 is an important component of repolarizing k+ current in canine atrial myocytes. *Circ Res*. 2003;93:744-751
31. Fedida D, Giles WR. Regional variations in action potentials and transient outward current in myocytes isolated from rabbit left ventricle. *J Physiol*. 1991;442:191-209
32. Feng YH, Ding Y, Ren S, Zhou L, Xu C, Karnik SS. Unconventional homologous internalization of the angiotensin ii type-1 receptor induced by g-protein-independent signals. *Hypertension*. 2005;46:419-425
33. Fiset C, Clark RB, Larsen TS, Giles WR. A rapidly activating sustained k+ current modulates repolarization and excitation-contraction coupling in adult mouse ventricle. *J Physiol*. 1997;504 (Pt 3):557-563
34. Forbes MS, van Neil EE. Membrane systems of guinea pig myocardium: Ultrastructure and morphometric studies. *Anat Rec*. 1988;222:362-379
35. Freer RJ, Pappano AJ, Peach MJ, Bing KT, McLean MJ, Vogel S, Sperelakis N. Mechanism for the postive inotropic effect of angiotensin ii on isolated cardiac muscle. *Circ Res*. 1976;39:178-183
36. Gao J, Wang W, Cohen IS, Mathias RT. Transmural gradients in na/k pump activity and [na+]i in canine ventricle. *Biophys J*. 2005;89:1700-1709
37. Gassanov N, Brandt MC, Michels G, Lindner M, Er F, Hoppe UC. Angiotensin ii-induced changes of calcium sparks and ionic currents in human atrial myocytes: Potential role for early remodeling in atrial fibrillation. *Cell Calcium*. 2006;39:175-186

38. Glitsch HG. Electrophysiology of the sodium-potassium-atpase in cardiac cells. *Physiol Rev*. 2001;81:1791-1826

39. Greenstein JL, Wu R, Po S, Tomaselli GF, Winslow RL. Role of the calcium-independent transient outward current i(to1) in shaping action potential morphology and duration. *Circ Res*. 2000;87:1026-1033

40. Guo W, Jung WE, Marionneau C, Aimond F, Xu H, Yamada KA, Schwarz TL, Demolombe S, Nerbonne JM. Targeted deletion of kv4.2 eliminates i(to,f) and results in electrical and molecular remodeling, with no evidence of ventricular hypertrophy or myocardial dysfunction. *Circ Res*. 2005;97:1342-1350

41. Guo W, Li H, Aimond F, Johns DC, Rhodes KJ, Trimmer JS, Nerbonne JM. Role of heteromultimers in the generation of myocardial transient outward k+ currents. *Circ Res*. 2002;90:586-593

42. Guo W, Li H, London B, Nerbonne JM. Functional consequences of elimination of i(to,f) and i(to,s): Early afterdepolarizations, atrioventricular block, and ventricular arrhythmias in mice lacking kv1.4 and expressing a dominant-negative kv4 alpha subunit. *Circ Res*. 2000;87:73-79

43. Heineke J, Molkentin JD. Regulation of cardiac hypertrophy by intracellular signalling pathways. *Nat Rev Mol Cell Biol*. 2006;7:589-600

44. Holloway AC, Qian H, Pipolo L, Ziogas J, Miura S, Karnik S, Southwell BR, Lew MJ, Thomas WG. Side-chain substitutions within angiotensin ii reveal different requirements for signaling, internalization, and phosphorylation of type 1a angiotensin receptors. *Mol Pharmacol*. 2002;61:768-777

45. Hu P, Zhang D, Swenson L, Chakrabarti G, Abel ED, Litwin SE. Minimally invasive aortic banding in mice: Effects of altered cardiomyocyte insulin signaling during pressure overload. *Am J Physiol Heart Circ Physiol*. 2003;285:H1261-1269

46. Hund TJ, Rudy Y. Rate dependence and regulation of action potential and calcium transient in a canine cardiac ventricular cell model. *Circulation*. 2004;110:3168-3174

47. Hunyady L, Baukal AJ, Balla T, Catt KJ. Independence of type i angiotensin ii receptor endocytosis from g protein coupling and signal transduction. *J Biol Chem*. 1994;269:24798-24804

48. Ichiyanagi O, Ishii K, Endoh M. Angiotensin ii increases l-type ca2+ current in gramicidin d-perforated adult rabbit ventricular myocytes: Comparison with conventional patch-clamp method. *Pflugers Arch*. 2002;444:107-116

49. Jeyaraj D, Wilson LD, Zhong J, Flask C, Saffitz JE, Deschenes I, Yu X, Rosenbaum DS. Mechanoelectrical feedback as novel mechanism of cardiac electrical remodeling. *Circulation*. 2007;115:3145-3155

50. Ju YK, Saint DA, Gage PW. Hypoxia increases persistent sodium current in rat ventricular myocytes. *J Physiol*. 1996;497 (Pt 2):337-347

51. Kaab S, Dixon J, Duc J, Ashen D, Nabauer M, Beuckelmann DJ, Steinbeck G, McKinnon D, Tomaselli GF. Molecular basis of transient outward potassium current downregulation in human heart failure: A decrease in kv4.3 mrna correlates with a reduction in current density. *Circulation*. 1998;98:1383-1393

52. Kaab S, Nuss HB, Chiamvimonvat N, O'Rourke B, Pak PH, Kass DA, Marban E, Tomaselli GF. Ionic mechanism of action potential prolongation in ventricular myocytes from dogs with pacing-induced heart failure. *Circ Res*. 1996;78:262-273

53. Kawai M, Hussain M, Orchard CH. Excitation-contraction coupling in rat ventricular myocytes after formamide-induced detubulation. *Am J Physiol*. 1999;277:H603-609

54. Koivumaki JT, Takalo J, Korhonen T, Tavi P, Weckstrom M. Modelling sarcoplasmic reticulum calcium atpase and its regulation in cardiac myocytes. *Philos Transact A Math Phys Eng Sci*. 2009;367:2181-2202

55. Kuo HC, Cheng CF, Clark RB, Lin JJ, Lin JL, Hoshijima M, Nguyen-Tran VT, Gu Y, Ikeda Y, Chu PH, Ross J, Giles WR, Chien KR. A defect in the kv channel-interacting protein 2 (kchip2) gene leads to a complete loss of i(to) and confers susceptibility to ventricular tachycardia. *Cell*. 2001;107:801-813

56. Kuryshev YA, Gudz TI, Brown AM, Wible BA. Kchap as a chaperone for specific k(+) channels. *Am J Physiol Cell Physiol*. 2000;278:C931-941

57. Lammerding J, Kamm RD, Lee RT. Mechanotransduction in cardiac myocytes. *Ann N Y Acad Sci*. 2004;1015:53-70

58. Lefkowitz RJ, Shenoy SK. Transduction of receptor signals by beta-arrestins. *Science*. 2005;308:512-517

59. Levin HR, Oz MC, Chen JM, Packer M, Rose EA, Burkhoff D. Reversal of chronic ventricular dilation in patients with end-stage cardiomyopathy by prolonged mechanical unloading. *Circulation*. 1995;91:2717-2720

60. Levy D, Garrison RJ, Savage DD, Kannel WB, Castelli WP. Prognostic implications of echocardiographically determined left ventricular mass in the framingham heart study. *N Engl J Med*. 1990;322:1561-1566

61. Li GR, Lau CP, Ducharme A, Tardif JC, Nattel S. Transmural action potential and ionic current remodeling in ventricles of failing canine hearts. *Am J Physiol Heart Circ Physiol*. 2002;283:H1031-1041

62. Lips DJ, deWindt LJ, van Kraaij DJ, Doevendans PA. Molecular determinants of myocardial hypertrophy and failure: Alternative pathways for beneficial and maladaptive hypertrophy. *Eur Heart J*. 2003;24:883-896

63. Litovsky SH, Antzelevitch C. Transient outward current prominent in canine ventricular epicardium but not endocardium. *Circ Res*. 1988;62:116-126

64. London B, Guo W, Pan X, Lee JS, Shusterman V, Rocco CJ, Logothetis DA, Nerbonne JM, Hill JA. Targeted replacement of kv1.5 in the mouse leads to loss of the 4-aminopyridine-sensitive component of i(k,slow) and resistance to drug-induced qt prolongation. *Circ Res*. 2001;88:940-946

65. Lu T, Ting AY, Mainland J, Jan LY, Schultz PG, Yang J. Probing ion permeation and gating in a k+ channel with backbone mutations in the selectivity filter. *Nat Neurosci*. 2001;4:239-246

66. Lue WM, Boyden PA. Abnormal electrical properties of myocytes from chronically infarcted canine heart. Alterations in vmax and the transient outward current. *Circulation*. 1992;85:1175-1188

67. Luo CH, Rudy Y. A model of the ventricular cardiac action potential. Depolarization, repolarization, and their interaction. *Circ Res*. 1991;68:1501-1526

68. Main MJ, Grantham CJ, Cannell MB. Changes in subsarcolemmal sodium concentration measured by na-ca exchanger activity during na-pump inhibition and beta-adrenergic stimulation in guinea-pig ventricular myocytes. *Pflugers Arch*. 1997;435:112-118

69. Marionneau C, Brunet S, Flagg TP, Pilgram TK, Demolombe S, Nerbonne JM. Distinct cellular and molecular mechanisms underlie functional remodeling of repolarizing k+ currents with left ventricular hypertrophy. *Circ Res*. 2008;102:1406-1415

70. Matsuda H, Kurata Y, Imanishi S, Sato R, Shibamoto T. Effects of angiotensin ii on sustained outward currents in rat ventricular myocytes. *Pflugers Arch*. 2004;448:54-62

71. McAllister RE, Noble D, Tsien RW. Reconstruction of the electrical activity of cardiac purkinje fibres. *J Physiol*. 1975;251:1-59

72. Mehta PK, Griendling KK. Angiotensin ii cell signaling: Physiological and pathological effects in the cardiovascular system. *Am J Physiol Cell Physiol*. 2007;292:C82-97

73. Mori Y, Fishman GI, Peskin CS. Ephaptic conduction in a cardiac strand model with 3d electrodiffusion. *Proc Natl Acad Sci U S A*. 2008;105:6463-6468

74. Mork HK, Sjaastad I, Sande JB, Periasamy M, Sejersted OM, Louch WE. Increased cardiomyocyte function and ca2+ transients in mice during early congestive heart failure. *J Mol Cell Cardiol*. 2007;43:177-186

75. Mudd JO, Kass DA. Tackling heart failure in the twenty-first century. *Nature*. 2008;451:919-928

76. Nabauer M, Beuckelmann DJ, Uberfuhr P, Steinbeck G. Regional differences in current density and rate-dependent properties of the transient outward current in subepicardial and subendocardial myocytes of human left ventricle. *Circulation*. 1996;93:168-177

77. Nerbonne JM, Kass RS. Molecular physiology of cardiac repolarization. *Physiol Rev*. 2005;85:1205-1253

78. Niwa N, Nerbonne JM. Molecular determinants of cardiac transient outward potassium current (i(to)) expression and regulation. *J Mol Cell Cardiol*. 2010;48:12-25

79. Noble D, Varghese A, Kohl P, Noble P. Improved guinea-pig ventricular cell model incorporating a diadic space, ikr and iks, and length- and tension-dependent processes. *Can J Cardiol*. 1998;14:123-134

80. Noble D, Varghese A, Kohl P, Noble P. Improved guinea-pig ventricular cell model incorporating a diadic space, ikr and iks, and length- and tension-dependent processes. *Can J Cardiol*. 1998;14:123-134

81. Noujaim SF, Pandit SV, Berenfeld O, Vikstrom K, Cerrone M, Mironov S, Zugermayr M, Lopatin AN, Jalife J. Up-regulation of the inward rectifier k+ current (i k1) in the mouse heart accelerates and stabilizes rotors. *J Physiol*. 2007;578:315-326

82. Oudit GY, Kassiri Z, Sah R, Ramirez RJ, Zobel C, Backx PH. The molecular physiology of the cardiac transient outward potassium current (i(to)) in normal and diseased myocardium. *J Mol Cell Cardiol*. 2001;33:851-872

83. Page E. Quantitative ultrastructural analysis in cardiac membrane physiology. *Am J Physiol*. 1978;235:C147-158

84. Pandit SV, Clark RB, Giles WR, Demir SS. A mathematical model of action potential heterogeneity in adult rat left ventricular myocytes. *Biophys J*. 2001;81:3029-3051

85. Pandit SV, Giles WR, Demir SS. A mathematical model of the electrophysiological alterations in rat ventricular myocytes in type-i diabetes. *Biophys J*. 2003;84:832-841

86. Paradis P, Dali-Youcef N, Paradis FW, Thibault G, Nemer M. Overexpression of angiotensin ii type i receptor in cardiomyocytes induces cardiac hypertrophy and remodeling. *Proc Natl Acad Sci U S A*. 2000;97:931-936

87. Patel SP, Parai R, Campbell DL. Regulation of kv4.3 voltage-dependent gating kinetics by kchip2 isoforms. *J Physiol*. 2004;557:19-41

88. Piñeiro G, Perelman S, Guerschman JP, Paruelo JM. How to evaluate models: Observed vs. Predicted or predicted vs. Observed? *Ecological Modelling*. 2008;216:316-322

89. Pott C, Ren X, Tran DX, Yang MJ, Henderson S, Jordan MC, Roos KP, Garfinkel A, Philipson KD, Goldhaber JI. Mechanism of shortened action potential duration in na+-ca2+ exchanger knockout mice. *Am J Physiol Cell Physiol*. 2007;292:C968-973

90. Qin D, Zhang ZH, Caref EB, Boutjdir M, Jain P, el-Sherif N. Cellular and ionic basis of arrhythmias in postinfarction remodeled ventricular myocardium. *Circ Res*. 1996;79:461-473

91. Rajagopal K, Whalen EJ, Violin JD, Stiber JA, Rosenberg PB, Premont RT, Coffman TM, Rockman HA, Lefkowitz RJ. Beta-arrestin2-mediated inotropic effects of the angiotensin ii type 1a receptor in isolated cardiac myocytes. *Proc Natl Acad Sci U S A*. 2006;103:16284-16289

92. Rivard K, Paradis P, Nemer M, Fiset C. Cardiac-specific overexpression of the human type 1 angiotensin ii receptor causes delayed repolarization. *Cardiovasc Res*. 2008;78:53-62

93. Rockman HA, Ross RS, Harris AN, Knowlton KU, Steinhelper ME, Field LJ, Ross J, Jr., Chien KR. Segregation of atrial-specific and inducible expression of an atrial natriuretic factor transgene in an in vivo murine model of cardiac hypertrophy. *Proc Natl Acad Sci U S A*. 1991;88:8277-8281

94. Roger VL, Go AS, Lloyd-Jones DM, Adams RJ, Berry JD, Brown TM, Carnethon MR, Dai S, de Simone G, Ford ES, Fox CS, Fullerton HJ, Gillespie C, Greenlund KJ, Hailpern SM, Heit JA, Ho PM, Howard VJ, Kissela BM, Kittner SJ, Lackland DT, Lichtman JH, Lisabeth LD, Makuc DM, Marcus GM, Marelli A, Matchar DB, McDermott MM, Meigs JB, Moy CS, Mozaffarian D, Mussolino ME, Nichol G, Paynter NP, Rosamond WD, Sorlie PD, Stafford RS, Turan TN, Turner MB, Wong ND, Wylie-Rosett J. Heart disease and stroke statistics--2011 update: A report from the american heart association. *Circulation*. 2011;123:e18-e209

95. Rosati B, Pan Z, Lypen S, Wang HS, Cohen I, Dixon JE, McKinnon D. Regulation of kchip2 potassium channel beta subunit gene expression underlies the gradient of transient outward current in canine and human ventricle. *J Physiol*. 2001;533:119-125

96. Rozanski GJ, Xu Z, Whitney RT, Murakami H, Zucker IH. Electrophysiology of rabbit ventricular myocytes following sustained rapid ventricular pacing. *J Mol Cell Cardiol*. 1997;29:721-732

97. Sabir IN, Fraser JA, Killeen MJ, Grace AA, Huang CL. The contribution of refractoriness to arrhythmic substrate in hypokalemic langendorff-perfused murine hearts. *Pflugers Arch*. 2007;454:209-222

98. Sadoshima J, Izumo S. Molecular characterization of angiotensin ii--induced hypertrophy of cardiac myocytes and hyperplasia of cardiac fibroblasts. Critical role of the at1 receptor subtype. *Circ Res*. 1993;73:413-423

99. Sadoshima J, Izumo S. The cellular and molecular response of cardiac myocytes to mechanical stress. *Annu Rev Physiol*. 1997;59:551-571

100. Sadoshima J, Xu Y, Slayter HS, Izumo S. Autocrine release of angiotensin ii mediates stretch-induced hypertrophy of cardiac myocytes in vitro. *Cell*. 1993;75:977-984

101. Sah R, Oudit GY, Nguyen TT, Lim HW, Wickenden AD, Wilson GJ, Molkentin JD, Backx PH. Inhibition of calcineurin and sarcolemmal ca2+ influx protects cardiac morphology and ventricular function in k(v)4.2n transgenic mice. *Circulation*. 2002;105:1850-1856

102. Sah R, Ramirez RJ, Backx PH. Modulation of ca(2+) release in cardiac myocytes by changes in repolarization rate: Role of phase-1 action potential repolarization in excitation-contraction coupling. *Circ Res*. 2002;90:165-173

103. Sah R, Ramirez RJ, Oudit GY, Gidrewicz D, Trivieri MG, Zobel C, Backx PH. Regulation of cardiac excitation-contraction coupling by action potential repolarization: Role of the transient outward potassium current (i(to)). *J Physiol*. 2003;546:5-18

104. Saint DA, Ju YK, Gage PW. A persistent sodium current in rat ventricular myocytes. *J Physiol*. 1992;453:219-231

105. Sakmann BF, Spindler AJ, Bryant SM, Linz KW, Noble D. Distribution of a persistent sodium current across the ventricular wall in guinea pigs. *Circ Res*. 2000;87:910-914

106. Scow DT, Smith EG, Shaughnessy AF. Combination therapy with ace inhibitors and angiotensin-receptor blockers in heart failure. *Am Fam Physician*. 2003;68:1795-1798

107. Shimoni Y. Inhibition of the formation or action of angiotensin ii reverses attenuated k+ currents in type 1 and type 2 diabetes. *J Physiol*. 2001;537:83-92

108. Snyders DJ, Tamkun MM, Bennett PB. A rapidly activating and slowly inactivating potassium channel cloned from human heart. Functional analysis after stable mammalian cell culture expression. *J Gen Physiol*. 1993;101:513-543

109. Sobie EA. Parameter sensitivity analysis in electrophysiological models using multivariable regression. *Biophys J*. 2009;96:1264-1274

110. Spruill LS, Baicu CF, Zile MR, McDermott PJ. Selective translation of mrnas in the left ventricular myocardium of the mouse in response to acute pressure overload. *J Mol Cell Cardiol*. 2008;44:69-75

111. Streeter DD, Jr., Vaishnav RN, Patel DJ, Spotnitz HM, Ross J, Jr., Sonnenblick EH. Stress distribution in the canine left ventricle during diastole and systole. *Biophys J*. 1970;10:345-363

112. Takeuchi S, Takagishi Y, Yasui K, Murata Y, Toyama J, Kodama I. Voltage-gated k(+)channel, kv4.2, localizes predominantly to the transverse-axial tubular system of the rat myocyte. *J Mol Cell Cardiol*. 2000;32:1361-1369

113. Tomaselli GF, Marban E. Electrophysiological remodeling in hypertrophy and heart failure. *Cardiovasc Res*. 1999;42:270-283

114. Tomita F, Bassett AL, Myerburg RJ, Kimura S. Diminished transient outward currents in rat hypertrophied ventricular myocytes. *Circ Res*. 1994;75:296-303

115. van Kats JP, Danser AH, van Meegen JR, Sassen LM, Verdouw PD, Schalekamp MA. Angiotensin production by the heart: A quantitative study in pigs with the use of radiolabeled angiotensin infusions. *Circulation*. 1998;98:73-81

116. van Kats JP, de Lannoy LM, Jan Danser AH, van Meegen JR, Verdouw PD, Schalekamp MA. Angiotensin ii type 1 (at1) receptor-mediated accumulation of angiotensin ii in tissues and its intracellular half-life in vivo. *Hypertension*. 1997;30:42-49

117. Varro A, Lathrop DA, Hester SB, Nanasi PP, Papp JG. Ionic currents and action potentials in rabbit, rat, and guinea pig ventricular myocytes. *Basic Res Cardiol*. 1993;88:93-102

118. Wang HS, Cohen IS. Calcium channel heterogeneity in canine left ventricular myocytes. *J Physiol*. 2003;547:825-833

119. Wang Y, Cheng J, Chen G, Rob F, Naseem RH, Nguyen L, Johnstone JL, Hill JA. Remodeling of outward k+ currents in pressure-overload heart failure. *J Cardiovasc Electrophysiol*. 2007;18:869-875

120. Wang Y, Rudy Y. Action potential propagation in inhomogeneous cardiac tissue: Safety factor considerations and ionic mechanism. *Am J Physiol Heart Circ Physiol*. 2000;278:H1019-1029

121. Wang YH, Shi CX, Dong F, Sheng JW, Xu YF. Inhibition of the rapid component of the delayed rectifier potassium current in ventricular myocytes by angiotensin ii via the at1 receptor. *Br J Pharmacol*. 2008;154:429-439

122. Watanabe T, Delbridge LM, Bustamante JO, McDonald TF. Heterogeneity of the action potential in isolated rat ventricular myocytes and tissue. *Circ Res*. 1983;52:280-290

123. Wei H, Ahn S, Shenoy SK, Karnik SS, Hunyady L, Luttrell LM, Lefkowitz RJ. Independent beta-arrestin 2 and g protein-mediated pathways for angiotensin ii activation of extracellular signal-regulated kinases 1 and 2. *Proc Natl Acad Sci U S A*. 2003;100:10782-10787

124. Wible BA, Yang Q, Kuryshev YA, Accili EA, Brown AM. Cloning and expression of a novel k+ channel regulatory protein, kchap. *J Biol Chem*. 1998;273:11745-11751

125. Wickenden AD, Lee P, Sah R, Huang Q, Fishman GI, Backx PH. Targeted expression of a dominant-negative k(v)4.2 k(+) channel subunit in the mouse heart. *Circ Res*. 1999;85:1067-1076

126. Xu H, Guo W, Nerbonne JM. Four kinetically distinct depolarization-activated k+ currents in adult mouse ventricular myocytes. *J Gen Physiol*. 1999;113:661-678

127. Yang EK, Alvira MR, Levitan ES, Takimoto K. Kvbeta subunits increase expression of kv4.3 channels by interacting with their c termini. *J Biol Chem*. 2001;276:4839-4844

128. Yasuda N, Akazawa H, Qin Y, Zou Y, Komuro I. A novel mechanism of mechanical stress-induced angiotensin ii type 1-receptor activation without the involvement of angiotensin ii. *Naunyn Schmiedebergs Arch Pharmacol*. 2008;377:393-399

129. Yasuda N, Miura S, Akazawa H, Tanaka T, Qin Y, Kiya Y, Imaizumi S, Fujino M, Ito K, Zou Y, Fukuhara S, Kunimoto S, Fukuzaki K, Sato T, Ge J, Mochizuki N, Nakaya H, Saku K, Komuro I. Conformational switch of angiotensin ii type 1 receptor underlying mechanical stress-induced activation. *EMBO Rep*. 2008;9:179-186

130. Yu H, Gao J, Wang H, Wymore R, Steinberg S, McKinnon D, Rosen MR, Cohen IS. Effects of the renin-angiotensin system on the current i(to) in epicardial and endocardial ventricular myocytes from the canine heart. *Circ Res*. 2000;86:1062-1068

131. Zou Y, Akazawa H, Qin Y, Sano M, Takano H, Minamino T, Makita N, Iwanaga K, Zhu W, Kudoh S, Toko H, Tamura K, Kihara M, Nagai T, Fukamizu A, Umemura S, Iiri T, Fujita T, Komuro I. Mechanical stress activates angiotensin ii type 1 receptor without the involvement of angiotensin ii. *Nat Cell Biol*. 2004;6:499-506

APPENDIX - Modifications to Existing AP Model (Bondarenko, et al. 2004)

1. I_{Na} α_3 and α_4 were changed in accordance with Clancy and Rudy (1999).

2. $I_{pCa,max}$ lowered to 0.05, similar to adult rat left ventricular model (Pandit, et al. 2001).

3. Published values of K^+ selectivity (permeability ratios: P_{Na}/P_K) were incorporated into the calculation of Nernst potentials for $I_{to,fast}$ (Campbell, et al. 1993), $I_{K,slow}$ (Snyders, et al. 1993) and I_{K1} (Lu, et al. 2001) channels.

4. $I_{to,fast}$ was reformulated so that the steady state activation time constants do not approach infinity at hyperpolarizing potentials and to shift the half-max steady state activation from -22.5 mV to -35 mV, which is uncompensated for the presence of divalent cations in the external solution (2 mM $CoCl_2$ shifts activation curve approximately -12.5 mV). This yielded the following equations:

$$\alpha_a = \frac{1.5e^{(V-30)/25}}{1+e^{(V-30)/25}} \qquad \beta_a = \frac{1.5e^{-(V+100)/25}}{1+e^{-(V+100)/25}}$$

$$\alpha_i = \frac{0.000152e^{-(V+23.5)/7}}{0.067083e^{-(V+43.5)/7}+1} \qquad \beta_i = \frac{0.00095e^{(V+43.5)/7}}{0.051335e^{(V+43.5)/7}+1}$$

$$\frac{da_{to,f}}{dt} = \alpha_a\left(1-a_{to,f}\right) - \beta_a a_{to,f} \qquad \frac{di_{to,f}}{dt} = \alpha_i\left(1-i_{to,f}\right) - \beta_i i_{to,f}$$

$$E_{to,f} = \frac{RT}{F} ln\left(\frac{0.92[K^+]_o + 0.08[Na^+]_o}{0.92[K^+]_i + 0.08[Na^+]_i}\right) \qquad R_{to,f} = e^{V/200}$$

$$I_{to,f} = G_{to,f} R_{to,f} a_{to,f}^6 i_{to,f}\left(V - E_{to,f}\right)$$

5. $I_{K,slow}$ was similarly reformulated to yield the following equations:

$$\alpha_a = \frac{0.91e^{(V-30.21)/18}}{1+e^{(V-30.21)/18}} \qquad \beta_a = 0.008e^{-(V-35)/23.5}$$

$$\tau_a = (\alpha_a + \beta_a)^{-1} \qquad \tau_i = 1200 - \frac{170}{1+e^{(V+35.2)/5.7}}$$

$$a_\infty = (1+e^{-(V+15)/10.7})^{-1} \qquad i_\infty = \left(1+e^{(V+35.2)/5.7}\right)^{-1}$$

$$\frac{da_{K,slow}}{dt} = \frac{a_\infty - a_{K,slow}}{\tau_a} \qquad \frac{di_{K,slow}}{dt} = \frac{i_\infty - i_{K,slow}}{\tau_i}$$

$$R_{K,slow} = e^{V/150}$$

$$E_{K,slow} = \frac{RT}{F} ln\left(\frac{0.993[K^+]_o + 0.007[Na^+]_o}{0.993[K^+]_i + 0.007[Na^+]_i}\right)$$

$$I_{K,slow} = G_{K,slow} R_{K,slow} a_{K,slow} i_{K,slow} (V - E_{K,slow})$$

6. Ionic concentrations were held constant to simulate patch clamp conditions.

7. $G_{Ca,L}$ was set to zero in order to simulate block of $I_{Ca,L}$ by $CoCl_2$.

8. A small leak current was added to simulate non-ideal whole-cell seal resistances.

$$I_{leak} = 0.002V$$